박 사 학 위 논 문

Ph.D. Dissertation

동적 해석을 위한 자유단 경계 기반의 부구조를 갖는 모델 축소 기법

On the model reduction methods with free-interface substructuring for dynamic analysis

2018

김 정 호(金 政 湖 Kim, Jeong-Ho)

한 국 과 학 기 술 원

Korea Advanced Institute of Science and Technology

박 사 학 위 논 문

동적 해석을 위한 자유단 경계 기반의 부구조를 갖는 모델 축소 기법

2018

김 정 호

한 국 과 학 기 술 원

기계항공공학부/기계공학과

동적 해석을 위한 자유단 경계 기반의 부구조를 갖는 모델 축소 기법

김 정 호

위 논문은 한국과학기술원 박사학위논문으로
학위논문 심사위원회의 심사를 통과하였음

2017년 11월 23일

심사위원장 이 필 승 (인)

심 사 위 원 박 용 화 (인)

심 사 위 원 오 일 권 (인)

심 사 위 원 윤 정 환 (인)

심 사 위 원 정 형 조 (인)

On the model reduction methods with free-interface substructuring for dynamic analysis

Jeong-Ho Kim

Advisor: Phill-Seung Lee

A dissertation submitted to the faculty of
Korea Advanced Institute of Science and Technology in
partial fulfillment of the requirements for the degree of
Doctor of Philosophy in Mechanical Engineering

Daejeon, Korea
November 23, 2017

Approved by

Phill-Seung Lee
Professor of Mechanical Engineering

The study was conducted in accordance with Code of Research Ethics[1].

1) Declaration of Ethical Conduct in Research: I, as a graduate student of Korea Advanced Institute of Science and Technology, hereby declare that I have not committed any act that may damage the credibility of my research. This includes, but is not limited to, falsification, thesis written by someone else, distortion of research findings, and plagiarism. I confirm that my dissertation contains honest conclusions based on my own careful research under the guidance of my advisor.

DME 20145065

김정호. 동적 해석을 위한 자유단 경계 기반의 부구조를 갖는 모델 축소 기법. 기계공학과. 2018년. 148+vii 쪽. 지도교수: 이필승. (영문 논문)

Kim, Jeong-Ho. On the model reduction methods with free-interface substructuring for dynamic analysis. Department of Mechanical Engineering. 2018. 148+vii pages. Advisor: Lee, Phill-Seung. (Text in English)

초 록

현대에 이르러 구조물에 대한 동적 응답 해석은 대형화, 복잡한 구조 설계 및 시공 조건 등으로 인해 어려움을 갖게 되었다. 유한요소 모델 구축 시 자유도가 매우 증가하기 때문에 구조해석을 위해서는 상당한 전산 시간이 소요된다. 이러한 이유로 모델 축소기법(model reduction method)에 대한 연구 필요성이 증가하고 있다. 모델 축소기법은 1960년대에 연구가 시작된 이후로 축소 절차의 전산 효율성, 축소모델의 정확도 개선, 주요 모드 또는 주 자유도의 선정, 부구조 간 경계조건의 처리 등 다양한 문제에 대하여 연구가 활발히 진행되고 있다. 본 연구에서는 이와 같은 주요 이슈를 해결하기 위하여 자유단 경계 기반의 부구조법을 적용한 새로운 축소기법을 개발하였다. 먼저, dual Craig-Bampton (DCB) 기법의 정확도를 향상시킨 새로운 부분구조합성법을 제안하였다. 또한 DCB 기법으로 얻은 축소 모델이 갖는 고유치의 신뢰도를 파악할 수 있는 정확한 오차 추정 기법을 제안하였다. 마지막으로 부구조 독립성을 갖는 자유도 기반 축소기법을 개발하였다. 특히 개발된 기법은 실제의 설계 및 제작 절차에 맞게 조립을 통해 전체 구조물의 유한요소 모델을 얻는 시스템에서 효과적으로 활용될 수 있을 것으로 기대한다. 다양한 수치예제들을 통하여 개발된 기법의 성능을 검증하였다.

Abstract

In response to the large and complex finite element models in practical engineering, the needs for studies on model reduction methods have been highlighted. Since 1960s, the model reduction methods have been actively studied for various problems such as computational efficiency of the reduction process, improvement of the accuracy of the reduction model. In this dissertation, the effective model reduction methods are proposed. The developed methods divide the entire finite element model into several substructures and consider the free-interface between neighboring substructures. In particular, the new component mode synthesis (CMS) method is provided by improving the accuracy of dual Craig-Bampton (DCB) method. The error estimation method for the DCB method is also proposed. For the degree of freedom based reduction method, the new dynamic condensation method with fully decoupled substructuring is proposed. Through the various numerical problems, the solution accuracy and computational efficiency of the present methods are demonstrated.

Keywords Finite element method, structural dynamics, model reduction method, component mode synthesis (CMS), Craig-Bampton (CB) method, dual Craig-Bampton (DCB) method, Guyan method, improved reduced system (IRS) method, system equivalent reduction expansion process (SEREP) method, interface reduction, eigenvalue problem

(Table of) Contents

List of Tables

List of Figures

Chapter 1. Introduction

1.1 Research Background

Model reduction methods have been widely used to reduce the degrees of freedom (DOFs) of a large finite element (FE) model. For a long time, significant efforts have been made to develop more effective reduction method to obtain accurate reduced models with computational efficiency. When a complicated structure consisting with various substructures is designed through the cooperation of different engineers, it is very expensive to deal with its FE models. This is because the whole and substructural models require frequent design modifications and repeated analysis. In response to the large and complex structure, the model reduction methods are used for various research fields such as eigenvalue analysis, multi-body dynamics, multi-physics, structural health monitoring, experimental-FE model correlation, and FE model updating.

Model reduction methods can be classified as the model based and DOF based reduction. The mode based reduction methods are called component mode syntheses (CMS) [1-11, 26-44, 61] in the field of structural dynamics. The substructuring algorithm is applied to construct a reduced model considering only the dominant modes for each substructure. As a representative method, the Craig-Bampton (CB) method [3] was developed in the 1960s, which used the fixed-interface condition between neighboring substructures. In the early 2000s, Rixen [9] and Park et al. [10] developed the free-interface based CMS method: the dual Craig-Bampton (DCB) method and flexibility-based CMS (FCMS), respectively. Through the free-interface based formulation, each substructure can be reduced independently before assemblage and has a better accuracy than the CB method.

In the DOF based reduction methods [16-20, 42, 49-58], the global FE model is divided into master DOFs and slave DOFs, and then condense the stiffness and inertial effects of slave DOFs to the master DOFs. As a representative methods, the Guyan reduction method [16] using the static condensation and the improved reduced system (IRS) method [17] considering the inertial effects additionally. Unlike the CMS methods, the DOF based reduction methods have been developed without applying the substructuring algorithm. Recently, it has been attempted to improve the efficiency of the DOF based reduction methods [49-58].

Since the beginning of the studies in the 1960s, the model reduction methods have been studied for various issues, such as the computation efficiency of reduction procedures, improvement of accuracy, selection of dominant modes or master DOFs, and treatment of interface between neighboring substructures [26-44, 49-58]. In this dissertation, there are focused on developing a new type of CMS method and a DOF based reduction method, both considering free-interface based substructuring algorithm. Especially, the effective model reduction methods are proposed which suitable for the structure obtained from the assemblage of independently constructed substructures.

1.2 Research purpose

The first objective of this dissertation is to improve the well-known dual Craig-Bampton (DCB) method [9]. The original transformation matrix of the DCB method is improved by considering the higher-order effect of residual substructural modes through residual flexibility. Using the new transformation matrix, original finite element models can be more accurately approximated in the reduced models. Herein, additional generalized coordinates are newly defined for considering the second order residual flexibility. Additional coordinates related to the interface boundary can be eliminated by applying the concept of SEREP (the system equivalent reduction expansion process) [18]. The formulation of the improved DCB method [44] is presented in detail, and its accuracy is investigated through numerical examples.

The second objective of this dissertation is to provide an error estimation method to accurately estimate the relative eigenvalue errors of reduced model by the DCB method [9]. By using the improved transformation matrix in the improved DCB method [44], the accurate error estimator for the DCB method is successfully developed. In the formulation, the computation of error estimator is simplified by using the component matrices of each substructure, instead of using the transformation matrix. Accurate error estimation is expected to be able to satisfy the solution accuracy effectively in application studies using the reduced model with the DCB method. The detailed formulation of the present error estimation method is presented, and its performance is demonstrated through numerical examples.

The third objective of this dissertation is to propose a novel DOFs based reduction method with fully decoupled substructures by employing the dual assembly technique. The IRS method [17] is adopted to reduce substructures, which are independently defined. The reduced mass and stiffness matrices of substructures are assembled by using a Lagrange multiplier vector, leading to the final reduced system. Using the proposed method, each substructural finite element (FE) model can be efficiently reduced without coupling of neighboring substructures and thus the method can be simply applied to substructures connected through non-matching meshes. The formulation of the proposed method is presented in detail, and its accuracy and computational efficiency are investigated through solving several practical engineering problems.

Hence, the research for this dissertation has been divided into three major parts:

I. Improving the accuracy of the dual Craig-Bampton method

II. Error estimation for dual Craig-Bampton method

III. A dynamic condensation method with free-interface based substructuring

The present model reduction studies are applicable to develop an effective parallel computation algorithm to deal with FE models with a large number of DOFs. We expect that the new method is an attractive solution for constructing accurate reduced models for experimental-FE model correlation, FE model updating, and optimizations.

1.3 Dissertation Organization

This dissertation is organized as follows:

In Chapter 2, the well-known model reduction methods discussed in this dissertation are introduced. In the following sections, the formulations of Craig-Bampton (CB), dual Craig-Bampton (DCB), and improved reduced system (IRS) methods are presented in detail [3, 9, 17].

In Chapter 3, the formulation of the improved DCB method [44] is presented. In the following sections, we derive a new transformation matrix for the DCB method, improved by considering the second order effect of residual substructural modes. The issue of the interface reduction for additional coordinates is discussed. The performance of the improved DCB method is described through various numerical examples. We considered six structural problems: a rectangular plate with matching and non-matching meshes, a plate with a hole, a hyperboloid shell, a bended pipe, a NACA 2415 wing with ailerons, and a cable-stayed bridge. The negative eigenvalues in lower modes for the original and improved DCB methods are also investigated.

In Chapter 4, the error estimation method of the DCB method is proposed. The formulation of improved transformation matrix is presented, and then error estimation method is derived by using new transformation matrix. The global matrix multiplications are simplified by the calculations in substructural component matrix level. The performance of the present error estimation method is investigated through numerical examples, and the correction of approximated eigenvalues are attempted. Here, four structural problems are considered: a rectangular plate with matching and non-matching meshes, a hyperboloid shell, a pipe intersection, and a cable-stayed bridge.

In Chapter 5, the new dynamic condensation method with free-interface based substructuring is proposed. The formulation of the free-interface based substructuring is presented, and then the new transformation matrix for the independently defined substructures is presented. The performance of the present method compared to the original IRS method is tested through the eigensolutions of various numerical examples: a rectangular plate with matching and non-matching meshes, a plate with a hole, a hyperboloid shell, a bended pipe with matching and non-matching meshes, a wind turbine rotor, a NACA 2415 wing with ailerons, and a cable-stayed bridge.

In Chapter 6, the conclusions and discussions for future works are presented.

Chapter 2. Model reduction methods

In this chapter, the well-known model reduction methods discussed in this dissertation are briefly introduced. The formulations of Craig-Bampton (CB), dual Craig-Bampton (DCB), and improved reduced system (IRS) methods are presented below. See references [3, 9, 17] for detailed derivations.

2.1 Craig-Bampton (CB) method

In the CB method [3], a global structural FE model is partitioned into N_s substructures as in Fig. 2.1a. The substructures are connected through a fixed interface boundary Γ (Fig. 2.1b).

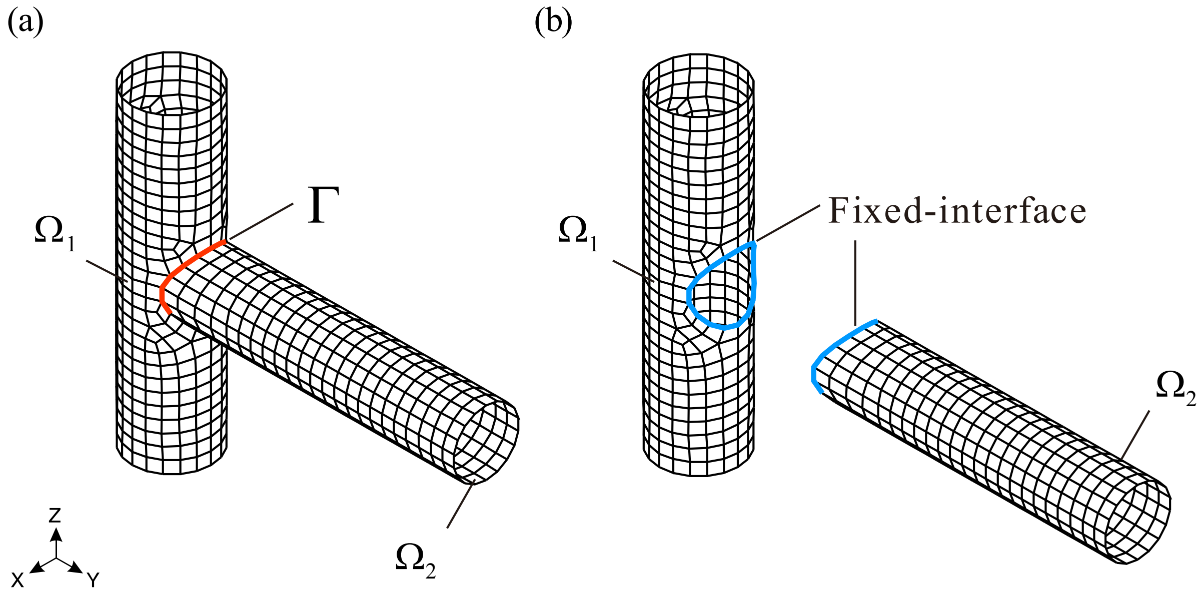

Figure 2.1 Partitioning of global FE model and interface handling in the CB method ($N_s = 2$).

The equations of motion can be expressed by

$$\mathbf{M}_g \ddot{\mathbf{u}}_g + \mathbf{K}_g \mathbf{u}_g = \mathbf{f}_g \tag{2.1}$$

with $\mathbf{M}_g = \begin{bmatrix} \mathbf{M}_s & \mathbf{M}_c \\ \mathbf{M}_c^T & \mathbf{M}_b \end{bmatrix}$, $\mathbf{K}_g = \begin{bmatrix} \mathbf{K}_s & \mathbf{K}_c \\ \mathbf{K}_c^T & \mathbf{K}_b \end{bmatrix}$, $\mathbf{u}_g = \begin{bmatrix} \mathbf{u}_s \\ \mathbf{u}_b \end{bmatrix}$, $\mathbf{f} = \begin{bmatrix} \mathbf{f}_s \\ \mathbf{f}_b \end{bmatrix}$,

where $\mathbf{M}$ and $\mathbf{K}$ are the mass and stiffness matrices, respectively, $\mathbf{u}$ is the corresponding displacement vector, $\mathbf{f}$ is the external load vector applied to the FE model. Note that $(\ddot{\ }) = d^2(\ )/dt^2$ with time variable t. The subscript g indicates the global structural quantities, and s, c and b indicate the substructural, coupled and interface boundary quantities, respectively. Here, $\mathbf{M}_s$ and $\mathbf{K}_s$ are block-diagonal mass and stiffness matrices that consist of substructural mass and stiffness matrices ($\mathbf{M}^{(i)}$ and $\mathbf{K}^{(i)}$).

The global eigenvalue problem is defined as

$$\mathbf{K}_g (\boldsymbol{\varphi}_g)_i = (\lambda_g)_i \mathbf{M}_g (\boldsymbol{\varphi}_g)_i \quad \text{for} \quad i = 1, \cdots, N_g \, , \tag{2.2}$$

in which $(\lambda_g)_i$ and $(\boldsymbol{\varphi}_g)_i$ are the global eigenvalue and eigenvector corresponding to the i^{th} global mode, respectively, and N_g is the number of DOFs in the original FE model. This number consists of interface and substructural DOFs ($N_g = N_b + \sum_{k=1}^{N_s} N_u^{(k)}$, where N_b is the number of interface DOFs and $N_u^{(k)}$ is the number of substructural DOFs of the k^{th} substructure).

Because the interface DOFs of each substructure can be seen as totally constrained, the substructural displacement vector $\mathbf{u}_s$ is assumed in the CB method, as

$$\mathbf{u}_s \approx \boldsymbol{\Theta}_s \mathbf{q}_s + \boldsymbol{\Phi}_c \mathbf{u}_b , \quad \boldsymbol{\Phi}_c = -\mathbf{K}_s^{-1} \mathbf{K}_c \, , \tag{2.3}$$

in which $\boldsymbol{\Theta}_s$ and $\mathbf{q}_s$ are the block-diagonal matrix that consists of substructural eigenvectors and the corresponding generalized coordinate vector, $\boldsymbol{\Phi}_c$ is the constraint mode matrix. The constraint mode matrix is defined as the mode shapes of the substructure due to unit displacement of interface DOF, and all other interface DOFs are constrained. The constraint mode matrix $\boldsymbol{\Phi}_c$ in Eq. (2.3) is calculated by

$$\mathbf{\Phi}_c = \begin{bmatrix} \mathbf{\Phi}_c^{(1)} \\ \mathbf{\Phi}_c^{(1)} \\ \vdots \\ \mathbf{\Phi}_c^{(N_s)} \end{bmatrix} \text{ with } \mathbf{\Phi}_c^{(k)} = -\mathbf{K}_s^{(k)^{-1}}\mathbf{K}_c^{(k)} \text{ for } k = 1, 2, \cdots, N_s . \tag{2.4}$$

The substructural normal modes are calculated by solving the following eigenvalue problems

$$\mathbf{K}^{(k)}\mathbf{\Theta}^{(k)} = \mathbf{\Lambda}^{(k)}\mathbf{M}^{(k)}\mathbf{\Theta}^{(k)}, \ k = 1, \cdots, N_s , \tag{2.5}$$

in which $\mathbf{\Theta}^{(k)}$ and $\mathbf{\Lambda}^{(k)}$ are the substructural eigenvector and eigenvalue matrices of the k^{th} substructure, respectively. Note that the eigenvectors are scaled to satisfy the mass-orthonormality condition.

The substructural eigenvector matrix $\mathbf{\Theta}^{(k)}$ in Eq. (2.5) consists of dominant and residual term

$$\mathbf{\Theta}^{(k)} = [\mathbf{\Theta}_d^{(k)} \quad \mathbf{\Theta}_r^{(k)}], \tag{2.6}$$

where $\mathbf{\Theta}_d^{(k)}$ and $\mathbf{\Theta}_r^{(k)}$ includes $N_d^{(k)}$ dominant substructural modes, and the remaining modes, respectively.

The substructural displacement vector can be approximated using only the dominant modes

$$\mathbf{u}_s \approx \mathbf{\Theta}_s^d \mathbf{q}_s^d + \mathbf{\Phi}_c \mathbf{u}_b , \tag{2.7}$$

in which $\mathbf{\Theta}_s^d$ and $\mathbf{q}_s^d$ are the block-diagonal eigenvector matrix that consists of dominant substructural modes and corresponding generalized coordinate vector.

Then, the global displacement vector $\mathbf{u}_g$ can be approximated using the transformation

$$\mathbf{u}_g \approx \mathbf{T}_0 \begin{bmatrix} \mathbf{q}_s^d \\ \mathbf{u}_b \end{bmatrix} \text{ with } \mathbf{T}_0 = \left[\begin{array}{c:c} \mathbf{\Theta}_s^d & \mathbf{\Phi}_c \\ \mathbf{0} & \mathbf{I}_b \end{array}\right], \tag{2.8}$$

where $\mathbf{T}_0$ is the transformation matrix ($N_g \times N_0$) of the CB method [3]. Note that, in the substructural eigenvalue problem, only the eigenpairs of the dominant modes are calculated, not for all eigenpairs.

The reduced mass and stiffness matrices ($N_0 \times N_0$) and the force vector ($N_0 \times 1$) of the CB method can be obtained as

$$\overline{\mathbf{M}}_0 = \mathbf{T}_0^T \mathbf{M}_g \mathbf{T}_0 , \ \overline{\mathbf{K}}_0 = \mathbf{T}_0^T \mathbf{K}_g \mathbf{T}_0 , \ \overline{\mathbf{f}}_0 = \mathbf{T}_0^T \mathbf{f}_g . \tag{2.9}$$

Note that N_0 is the number of DOFs in the reduced FE model: $N_0 = N_b + \sum_{k=1}^{N_s} N_d^{(k)}$, in which $N_d^{(i)}$ is the number of dominant modes of the k^{th} substructure.

2.2 Dual Craig-Bampton (DCB) method

In the DCB method [9], a structural FE model is assembled by N_s substructures as in Fig. 2.2a. The substructures are connected through a free-interface boundary Γ (Fig. 2.2b). The compatibility between substructures is explicitly enforced using the following constraint equation

$$\sum_{k=1}^{N_s} \mathbf{b}^{(k)^T} \mathbf{u}_b^{(k)} = \mathbf{0}, \tag{2.10}$$

in which $\mathbf{u}_b^{(k)}$ is the interface displacement vector of the k^{th} substructure, and $\mathbf{b}^{(k)}$ is a signed Boolean matrix.

The linear dynamic equations for each substructure Ω_k can be individually expressed by

$$\mathbf{M}^{(k)}\ddot{\mathbf{u}}^{(k)} + \mathbf{K}^{(k)}\mathbf{u}^{(k)} + \mathbf{B}^{(k)}\boldsymbol{\mu} = \mathbf{f}^{(k)},\ \ k = 1, \cdots, N_s, \tag{2.11}$$

where $\mathbf{M}^{(k)}$ and $\mathbf{K}^{(k)}$ are the mass and stiffness matrices of the k^{th} substructure, $\mathbf{u}^{(k)}$ is the corresponding displacement vector, $\mathbf{f}^{(k)}$ is the external load vector applied to the substructure, and $\mathbf{B}^{(k)}\boldsymbol{\mu}$ is the interconnecting force between substructures with $\mathbf{B}^{(k)} = \begin{bmatrix} \mathbf{0} \\ \mathbf{b}^{(k)} \end{bmatrix}$ and the Lagrange multiplier vector $\boldsymbol{\mu}$. Note that $(\ddot{\ }) = d^2(\ )/dt^2$ with time variable t.

Assembling the linear dynamic equations for each substructure in Eq. (2.11) using the compatibility constraint equation in Eq. (2.10), the dynamic equilibrium equation of the original assembled FE model (see Fig. 2.2c) is constructed as

$$\begin{bmatrix} \mathbf{M} & \mathbf{0} \\ \mathbf{0} & \mathbf{0} \end{bmatrix} \begin{bmatrix} \ddot{\mathbf{u}} \\ \boldsymbol{\mu} \end{bmatrix} + \begin{bmatrix} \mathbf{K} & \mathbf{B} \\ \mathbf{B}^T & \mathbf{0} \end{bmatrix} \begin{bmatrix} \mathbf{u} \\ \boldsymbol{\mu} \end{bmatrix} = \begin{bmatrix} \mathbf{f} \\ \mathbf{0} \end{bmatrix}, \tag{2.12}$$

$$\text{with}\ \ \mathbf{M}=\begin{bmatrix}\mathbf{M}^{(1)} & & \mathbf{0}\\ & \ddots & \\ \mathbf{0} & & \mathbf{M}^{(N_s)}\end{bmatrix},\ \mathbf{K}=\begin{bmatrix}\mathbf{K}^{(1)} & & \mathbf{0}\\ & \ddots & \\ \mathbf{0} & & \mathbf{K}^{(N_s)}\end{bmatrix},\ \mathbf{u}=\begin{bmatrix}\mathbf{u}^{(1)}\\ \vdots\\ \mathbf{u}^{(N_s)}\end{bmatrix},\ \mathbf{f}=\begin{bmatrix}\mathbf{f}^{(1)}\\ \vdots\\ \mathbf{f}^{(N_s)}\end{bmatrix},\ \mathbf{B}=\begin{bmatrix}\mathbf{B}^{(1)}\\ \vdots\\ \mathbf{B}^{(N_s)}\end{bmatrix},$$

where $\mathbf{M}$ and $\mathbf{K}$ are block-diagonal mass and stiffness matrices that consist of substructural mass and stiffness matrices ($\mathbf{M}^{(k)}$ and $\mathbf{K}^{(k)}$).

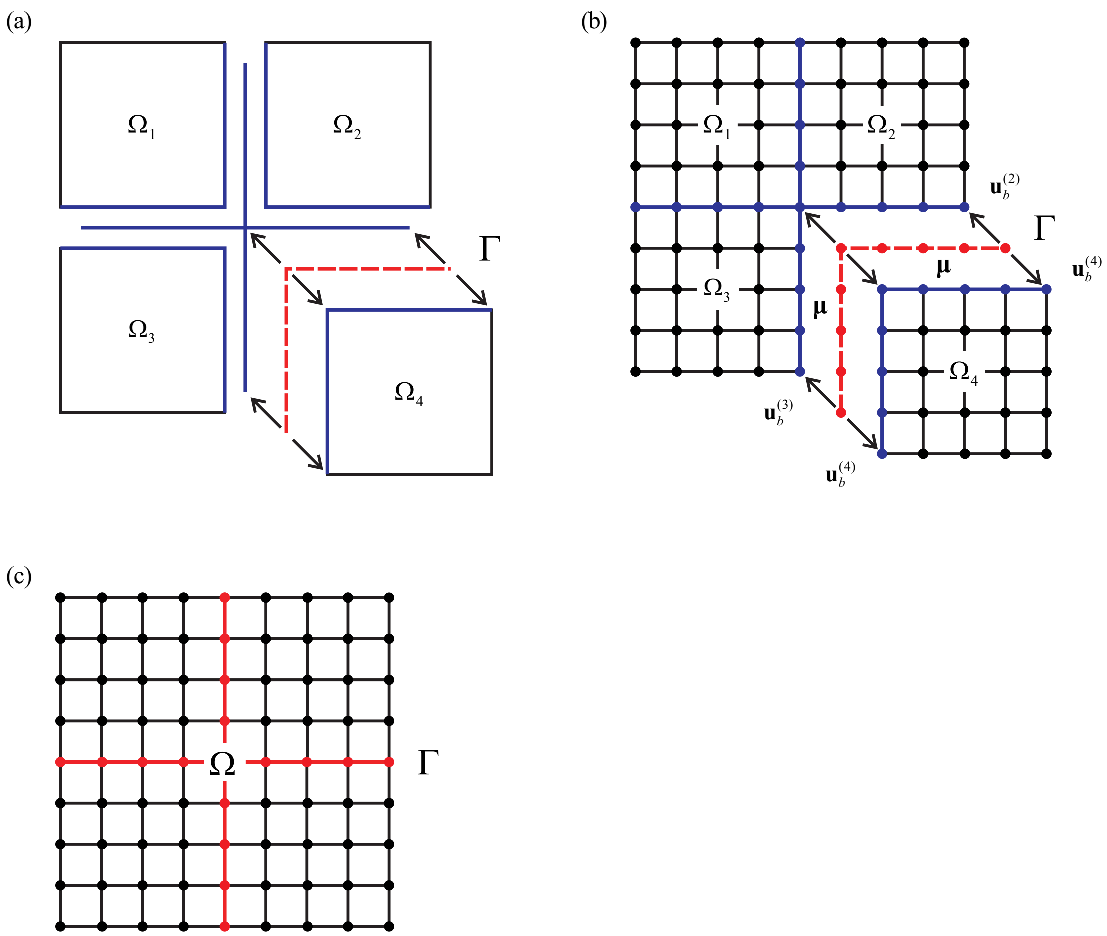

Figure 2.2 Assemblage of substructures and interface handling in the DCB method ($N_s = 4$). (a) Substructures, Ω_1, Ω_2, Ω_3 and Ω_4, (b) Interconnecting forces and interfacial DOFs of the substructure Ω_4, (c) Assembled FE model Ω with its interface boundary Γ.

The global eigenvalue problem is defined for the original assembled FE model

$$\mathbf{K}_g(\boldsymbol{\varphi}_g)_i = (\lambda_g)_i \mathbf{M}_g(\boldsymbol{\varphi}_g)_i \quad \text{for } i = 1, \cdots, N_g, \tag{2.13}$$

$$\text{with } \mathbf{K}_g = \begin{bmatrix} \mathbf{K} & \mathbf{B} \\ \mathbf{B}^T & \mathbf{0} \end{bmatrix}, \ \mathbf{M}_g = \begin{bmatrix} \mathbf{M} & \mathbf{0} \\ \mathbf{0} & \mathbf{0} \end{bmatrix},$$

in which $(\lambda_g)_i$ and $(\boldsymbol{\varphi}_g)_i$ are the global eigenvalue and eigenvector corresponding to the i^{th} global mode, respectively, and N_g is the number of DOFs in the original FE model. This number consists of interface and substructural DOFs ($N_g = N_\mu + \sum_{k=1}^{N_s} N_u^{(k)}$, where N_μ is the number of Lagrange multipliers and $N_u^{(k)}$ is the number of DOFs of the k^{th} substructure).

Because each substructure can be seen as being excited through interconnecting forces, the displacement of each substructure is assumed in the original DCB formulation, as

$$\mathbf{u}^{(k)} \approx -\mathbf{K}^{(k)^+}\mathbf{B}^{(k)}\boldsymbol{\mu} + \mathbf{R}^{(k)}\boldsymbol{\alpha}^{(k)} + \boldsymbol{\Theta}^{(k)}\mathbf{q}^{(k)}, \ k = 1, \cdots, N_s, \tag{2.14}$$

where $\mathbf{K}^{(k)^+}$ is the generalized inverse matrix of $\mathbf{K}^{(k)}$ (the flexibility matrix), $\mathbf{R}^{(k)}$ is the rigid body mode matrix, $\boldsymbol{\Theta}^{(k)}$ is the matrix that consists of free-interface normal modes, and $\boldsymbol{\alpha}^{(k)}$ and $\mathbf{q}^{(k)}$ are the corresponding generalized coordinate vectors.

The rigid body and free-interface normal modes of the k^{th} substructure are calculated by solving the following eigenvalue problems

$$\mathbf{K}^{(k)}(\boldsymbol{\varphi}^{(k)})_j = \lambda_j^{(k)}\mathbf{M}^{(k)}(\boldsymbol{\varphi}^{(k)})_j, \ \ j = 1, \cdots, N_u^{(k)}, \tag{2.15}$$

in which $\lambda_j^{(k)}$ and $(\boldsymbol{\varphi}^{(k)})_j$ are the j^{th} eigenvalue and the corresponding mode, respectively. Note that the mode vectors are scaled to satisfy the mass-orthonormality condition.

The free-interface normal mode matrix $\boldsymbol{\Theta}^{(k)}$ in Eq. (2.14) consists of dominant and residual normal modes

$$\boldsymbol{\Theta}^{(k)} = \left[\boldsymbol{\Theta}_d^{(k)} \quad \boldsymbol{\Theta}_r^{(k)}\right], \tag{2.16}$$

in which $\boldsymbol{\Theta}_d^{(k)}$ and $\boldsymbol{\Theta}_r^{(k)}$ includes $N_d^{(k)}$ dominant free-interface normal modes, and the remaining modes, respectively.

The displacement of the substructure can be approximated using only the dominant modes

$$\mathbf{u}^{(k)} \approx -\mathbf{K}^{(k)^+}\mathbf{B}^{(k)}\boldsymbol{\mu} + \mathbf{R}^{(k)}\boldsymbol{\alpha}^{(k)} + \boldsymbol{\Theta}_d^{(k)}\mathbf{q}_d^{(k)}, \tag{2.17}$$

where the term $-\mathbf{K}^{(k)^+}\mathbf{B}^{(k)}\boldsymbol{\mu}$ is the static displacement by interconnecting forces, and this term can be expressed using modal parameters

$$-\mathbf{K}^{(k)^+}\mathbf{B}^{(k)}\boldsymbol{\mu} = -\boldsymbol{\Theta}^{(k)}\boldsymbol{\Lambda}^{(k)^{-1}}\boldsymbol{\Theta}^{(k)^T}\mathbf{B}^{(k)}\boldsymbol{\mu} \quad \text{with} \quad \boldsymbol{\Lambda}^{(k)} = \mathrm{diag}(\lambda_1^{(k)}, \lambda_2^{(k)}, \ldots \lambda_{N_u^{(k)}}^{(k)}), \tag{2.18}$$

where $\boldsymbol{\Lambda}^{(k)}$ is the substructural eigenvalue matrix.

Substituting Eq. (2.16) into Eq. (2.18), the static displacement can be divided into dominant and residual parts

$$-\mathbf{K}^{(k)^+}\mathbf{B}^{(k)}\boldsymbol{\mu} = -\boldsymbol{\Theta}_d^{(k)}\boldsymbol{\Lambda}_d^{(k)^{-1}}\boldsymbol{\Theta}_d^{(k)^T}\mathbf{B}^{(k)}\boldsymbol{\mu} - \boldsymbol{\Theta}_r^{(k)}\boldsymbol{\Lambda}_r^{(k)^{-1}}\boldsymbol{\Theta}_r^{(k)^T}\mathbf{B}^{(k)}\boldsymbol{\mu}, \tag{2.19}$$

with the corresponding substructural eigenvalue matrices $\boldsymbol{\Lambda}_d^{(k)}$ and $\boldsymbol{\Lambda}_r^{(k)}$ defined by

$$\boldsymbol{\Lambda}_d^{(k)} = \boldsymbol{\Theta}_d^{(k)^T}\mathbf{K}^{(k)}\boldsymbol{\Theta}_d^{(k)}, \;\; \boldsymbol{\Lambda}_r^{(k)} = \boldsymbol{\Theta}_r^{(k)^T}\mathbf{K}^{(k)}\boldsymbol{\Theta}_r^{(k)}. \tag{2.20}$$

Using Eq. (2.19) in Eq. (2.17), the following equation is obtained:

$$\mathbf{u}^{(k)} \approx -\boldsymbol{\Theta}_d^{(k)}\boldsymbol{\Lambda}_d^{(k)^{-1}}\boldsymbol{\Theta}_d^{(k)^T}\mathbf{B}^{(k)}\boldsymbol{\mu} - \boldsymbol{\Theta}_r^{(k)}\boldsymbol{\Lambda}_r^{(k)^{-1}}\boldsymbol{\Theta}_r^{(k)^T}\mathbf{B}^{(k)}\boldsymbol{\mu} + \mathbf{R}^{(k)}\boldsymbol{\alpha}^{(k)} + \boldsymbol{\Theta}_d^{(k)}\mathbf{q}_d^{(k)}. \tag{2.21}$$

It is easily observed that the first and last terms on the right side of Eq. (2.21) are identical and thus neglecting the first term, we obtain

$$\mathbf{u}^{(k)} \approx -\mathbf{F}_1^{(k)}\mathbf{B}^{(k)}\boldsymbol{\mu} + \mathbf{R}^{(k)}\boldsymbol{\alpha}^{(k)} + \boldsymbol{\Theta}_d^{(k)}\mathbf{q}_d^{(k)} \quad \text{with} \quad \mathbf{F}_1^{(k)} = \boldsymbol{\Theta}_r^{(k)}\boldsymbol{\Lambda}_r^{(k)^{-1}}\boldsymbol{\Theta}_r^{(k)^T}. \tag{2.22}$$

in which $\mathbf{F}_1^{(k)}$ is called the residual flexibility matrix. The residual flexibility matrix can be calculated by subtracting the dominant flexibility matrix from the full flexibility matrix $\mathbf{K}^{(k)^+}$

$$\mathbf{F}_1^{(k)} = \mathbf{K}^{(k)^+} - \boldsymbol{\Theta}_d^{(k)}\boldsymbol{\Lambda}_d^{(k)^{-1}}\boldsymbol{\Theta}_d^{(k)^T}. \tag{2.23}$$

The displacement and the Lagrange multipliers of the k^{th} substructure can be approximated using the transformation

$$\begin{bmatrix} \mathbf{u}^{(k)} \\ \boldsymbol{\mu} \end{bmatrix} \approx \mathbf{T}_1^{(k)} \begin{bmatrix} \boldsymbol{\alpha}^{(k)} \\ \mathbf{q}_d^{(k)} \\ \hline \boldsymbol{\mu} \end{bmatrix} \quad \text{with} \quad \mathbf{T}_1^{(k)} = \left[\begin{array}{cc|c} \mathbf{R}^{(k)} & \boldsymbol{\Theta}_d^{(k)} & -\mathbf{F}_1^{(k)}\mathbf{B}^{(k)} \\ \mathbf{0} & \mathbf{0} & \mathbf{I} \end{array}\right], \tag{2.24}$$

in which $\mathbf{T}_1^{(k)}$ is the substructural transformation matrix of the original DCB method for the k^{th} substructure [9]. Note that, in the substructural eigenvalue problem, only the eigenpairs of the dominant and rigid body modes are calculated, not for all eigenpairs.

The transformation matrix $\mathbf{T}_1$ ($N_g \times N_1$) for the original assembled FE model is then given by

$$\begin{bmatrix} \mathbf{u} \\ \boldsymbol{\mu} \end{bmatrix} \approx \mathbf{T}_1 \begin{bmatrix} \boldsymbol{\alpha}^{(1)} \\ \vdots \\ \boldsymbol{\alpha}^{(N_s)} \\ \mathbf{q}_d^{(1)} \\ \vdots \\ \mathbf{q}_d^{(N_s)} \\ \hline \boldsymbol{\mu} \end{bmatrix} \quad \text{with} \quad \mathbf{T}_1 = \left[\begin{array}{cccccc|c} \mathbf{R}^{(1)} & & \mathbf{0} & \boldsymbol{\Theta}_d^{(1)} & & \mathbf{0} & -\mathbf{F}_1^{(1)}\mathbf{B}^{(1)} \\ & \ddots & & & \ddots & & \vdots \\ \mathbf{0} & & \mathbf{R}^{(N_s)} & \mathbf{0} & & \boldsymbol{\Theta}_d^{(N_s)} & -\mathbf{F}_1^{(N_s)}\mathbf{B}^{(N_s)} \\ \mathbf{0} & \cdots & \mathbf{0} & \mathbf{0} & \cdots & \mathbf{0} & \mathbf{I} \end{array}\right]. \tag{2.25}$$

and the reduced mass and stiffness matrices ($N_1 \times N_1$) and the force vector ($N_1 \times 1$) are obtained using the transformation matrix

$$\overline{\mathbf{M}}_1 = \mathbf{T}_1^T \begin{bmatrix} \mathbf{M} & \mathbf{0} \\ \mathbf{0} & \mathbf{0} \end{bmatrix} \mathbf{T}_1, \ \overline{\mathbf{K}}_1 = \mathbf{T}_1^T \begin{bmatrix} \mathbf{K} & \mathbf{B} \\ \mathbf{B}^T & \mathbf{0} \end{bmatrix} \mathbf{T}_1, \ \bar{\mathbf{f}}_1 = \mathbf{T}_1^T \begin{bmatrix} \mathbf{f} \\ \mathbf{0} \end{bmatrix} \tag{2.26}$$

Note that N_1 is the number of DOFs in the reduced FE model: $N_1 = N_0 + N_\mu$ with $N_0 = \sum_{k=1}^{N_s} \left(N_r^{(k)} + N_d^{(k)} \right)$, in which $N_r^{(k)}$ and $N_d^{(k)}$ are the numbers of rigid body modes and dominant modes of the k^{th} substructure, respectively.

The eigenvalue problem with the reduced mass and stiffness matrices in the DCB method is defined as

$$\overline{\mathbf{K}}\overline{\boldsymbol{\varphi}}_i = \bar{\lambda}_i \overline{\mathbf{M}}\overline{\boldsymbol{\varphi}}_i, \ i = 1, \cdots, \overline{N}, \tag{2.27}$$

where $\bar{\lambda}_i$ and $\overline{\boldsymbol{\varphi}}_i$ are the approximated eigenvalues and the corresponding eigenvectors, respectively. $\overline{N}$ is the number of DOFs in the reduced model : $\overline{N} = N_\mu + N_m$ with $N_m = \sum_{k=1}^{N_s} (N_r^{(k)} + N_d^{(k)})$, where $N_r^{(k)}$ is the number of rigid body modes of the k^{th} substructure.

2.3 Improved reduced system (IRS) method

In the IRS method [17], the equations of motion for undamped free vibration are given by

$$\mathbf{M}_g \ddot{\mathbf{U}}_g + \mathbf{K}_g \mathbf{U}_g = \mathbf{0}, \tag{2.28a}$$

$$\text{with } \mathbf{M}_g = \begin{bmatrix} \mathbf{M}_{ss} & \mathbf{M}_{sm} \\ \mathbf{M}_{ms} & \mathbf{M}_{mm} \end{bmatrix}, \ \mathbf{K}_g = \begin{bmatrix} \mathbf{K}_{ss} & \mathbf{K}_{sm} \\ \mathbf{K}_{ms} & \mathbf{K}_{mm} \end{bmatrix}, \ \mathbf{U}_g = \begin{bmatrix} \mathbf{U}_s \\ \mathbf{U}_m \end{bmatrix}, \tag{2.28b}$$

in which $\mathbf{M}_g$ and $\mathbf{K}_g$ are the mass and stiffness matrices of global structural FE model (see Fig. 2.3a), $\mathbf{U}_g$ is the corresponding displacement vector. The subscripts s and m denote the 'slave' and 'master' DOFs, respectively (see Fig. 2.3b). Note that $(\ddot{\ }) = \mathrm{d}^2(\ )/dt^2$ with time variable t.

The global eigenvalue problem can be written as

$$\begin{bmatrix} \mathbf{K}_{ss} & \mathbf{K}_{sm} \\ \mathbf{K}_{ms} & \mathbf{K}_{mm} \end{bmatrix} \begin{bmatrix} \mathbf{u}_s \\ \mathbf{u}_m \end{bmatrix} = \lambda \begin{bmatrix} \mathbf{M}_{ss} & \mathbf{M}_{sm} \\ \mathbf{M}_{ms} & \mathbf{M}_{mm} \end{bmatrix} \begin{bmatrix} \mathbf{u}_s \\ \mathbf{u}_m \end{bmatrix}, \text{ with } \mathbf{u}_g = \begin{bmatrix} \mathbf{u}_s \\ \mathbf{u}_m \end{bmatrix}, \tag{2.29}$$

where λ and $\mathbf{u}_g$ are the eigenvalue and eigenvector of global FE model, $\mathbf{u}_s$ and $\mathbf{u}_m$ are the eigenvectors corresponding to the slave and master DOFs, respectively. From the first row in Eq. (2.29), $\mathbf{u}_s$ is represented by

$$\mathbf{u}_s = -(\mathbf{K}_{ss} - \lambda \mathbf{M}_{ss})^{-1}(\mathbf{K}_{sm} - \lambda \mathbf{M}_{sm})\mathbf{u}_m. \tag{2.30}$$

Using the Neumann series expansion [40-48, 61-64], Eq. (2.30) can be expanded by

$$\mathbf{u}_s = -(\mathbf{K}_{ss}^{-1} + \lambda \mathbf{K}_{ss}^{-1}\mathbf{M}_{ss}\mathbf{K}_{ss}^{-1} + o(\lambda^2) + o(\lambda^3) + \cdots)(\mathbf{K}_{sm} - \lambda \mathbf{M}_{sm})\mathbf{u}_m. \tag{2.31}$$

and neglecting higher order terms of λ, $\mathbf{u}_s$ is approximated as follows

$$\mathbf{u}_s \approx \bar{\mathbf{u}}_s = (-\mathbf{K}_{ss}^{-1}\mathbf{K}_{sm} + \lambda \mathbf{K}_{ss}^{-1}(\mathbf{M}_{sm} - \mathbf{M}_{ss}\mathbf{K}_{ss}^{-1}\mathbf{K}_{sm}))\mathbf{u}_m. \tag{2.32}$$

Then, the approximated global eigenvector $\bar{\mathbf{u}}_g$ is obtained by

$$\mathbf{u}_g \approx \bar{\mathbf{u}}_g = \begin{bmatrix} \bar{\mathbf{u}}_s \\ \mathbf{u}_m \end{bmatrix} = (\mathbf{T}_0 + \lambda \mathbf{T}_a)\mathbf{u}_m, \tag{2.33a}$$

$$\text{with } \mathbf{T}_0 = \begin{bmatrix} -\mathbf{K}_{ss}^{-1}\mathbf{K}_{sm} \\ \mathbf{I}_m \end{bmatrix}, \ \mathbf{T}_a = \begin{bmatrix} \mathbf{K}_{ss}^{-1}(\mathbf{M}_{sm} - \mathbf{M}_{ss}\mathbf{K}_{ss}^{-1}\mathbf{K}_{sm}) \\ \mathbf{0} \end{bmatrix}, \tag{2.33b}$$

where $\mathbf{T}_0$ is called the Guyan transformation matrix [16], $\mathbf{T}_a$ is the additional transformation matrix containing the inertial effects of the slave DOFs, and $\mathbf{I}_m$ is the identity matrix corresponding to the master DOFs.

In the Guyan method [16], the approximated global eigenvector $\bar{\mathbf{u}}_g$ is defined by

$$\bar{\mathbf{u}}_g = \mathbf{T}_0 \mathbf{u}_m, \tag{2.34}$$

and then, the reduced eigenvalue problem is obtained by

$$\bar{\mathbf{K}}_0 \mathbf{u}_m = \bar{\lambda} \bar{\mathbf{M}}_0 \mathbf{u}_m \ \text{ with } \ \bar{\mathbf{M}}_0 = \mathbf{T}_0^T \mathbf{M}_g \mathbf{T}_0, \ \bar{\mathbf{K}}_0 = \mathbf{T}_0^T \mathbf{K}_g \mathbf{T}_0, \tag{2.35}$$

in which $\bar{\mathbf{M}}_0$ and $\bar{\mathbf{K}}_0$ are the reduced mass and stiffness matrices, and $\bar{\lambda}$ is the approximated eigenvalue in the Guyan method [16].

Multiplying $\bar{\mathbf{M}}_0^{-1}$ on the both sides of Eq. (2.35), the following relation is obtained

$$\bar{\lambda} \mathbf{u}_m = \mathbf{H}_0 \mathbf{u}_m \ \text{ with } \ \mathbf{H}_0 = \bar{\mathbf{M}}_0^{-1} \bar{\mathbf{K}}_0, \tag{2.36}$$

note that, from this relation, the eigenvalue $\bar{\lambda}$ can be replaced with the matrix $\mathbf{H}_0$.

In Eq. (2.33a), using $\bar{\lambda}$ instead of λ, and applying the relation $\bar{\lambda}\mathbf{u}_m = \mathbf{H}_0\mathbf{u}_m$ in Eq. (2.36), the approximated global eigenvector $\bar{\mathbf{u}}_g$ can be more accurately defined as follows

$$\bar{\mathbf{u}}_g = \mathbf{T}_1 \mathbf{u}_m \quad \text{with} \quad \mathbf{T}_1 = \mathbf{T}_0 + \mathbf{T}_a \mathbf{H}_0, \tag{2.37}$$

where $\mathbf{T}_1$ is the transformation matrix of the IRS method [17].

Using Eq. (2.37), the reduced mass and stiffness matrices in the IRS method (see Fig. 2.3c) are calculated as

$$\overline{\mathbf{M}}_1 = \mathbf{T}_1^T \mathbf{M}_g \mathbf{T}_1 = \overline{\mathbf{M}}_0 + \mathbf{T}_0^T \mathbf{M}_g \mathbf{T}_a \mathbf{H}_0 + \mathbf{H}_0^T \mathbf{T}_a^T \mathbf{M}_g \mathbf{T}_0 + \mathbf{H}_0^T \mathbf{T}_a^T \mathbf{M}_g \mathbf{T}_a \mathbf{H}_0, \tag{2.38a}$$

$$\overline{\mathbf{K}}_1 = \mathbf{T}_1^T \mathbf{K}_g \mathbf{T}_1 = \overline{\mathbf{K}}_0 + \mathbf{T}_0^T \mathbf{K}_g \mathbf{T}_a \mathbf{H}_0 + \mathbf{H}_0^T \mathbf{T}_a^T \mathbf{K}_g \mathbf{T}_0 + \mathbf{H}_0^T \mathbf{T}_a^T \mathbf{K}_g \mathbf{T}_a \mathbf{H}_0. \tag{2.38b}$$

Finally, the reduced eigenvalue problem in the IRS method [17] is given by

$$\overline{\mathbf{K}}_1 (\overline{\boldsymbol{\varphi}})_i = \bar{\lambda}_i \overline{\mathbf{M}}_1 (\overline{\boldsymbol{\varphi}})_i, \quad i = 1, 2, \cdots, N_m, \tag{2.39}$$

where $(\bar{\lambda}_1)_i$ and $(\overline{\boldsymbol{\varphi}}_1)_i$ are the approximated i^{th} eigenvalues and corresponding eigenvectors in the IRS method, and N_m is the number of master DOFs, which is same with the size of the reduced model.

The transformation procedure of the IRS method [17] described in Eq. (2.38) seems simple matrix multiplications. However, in the IRS method, the global structural FE model is considered without substructuring. For a large FE model, the construction of $\mathbf{T}_1$ in Eq. (2.37) is very difficult or even impossible in a personal computer, because it contains computationally expensive procedures such as inversion of large submatrix, $\mathbf{K}_{ss}^{-1}$ in Eq. (2.33).

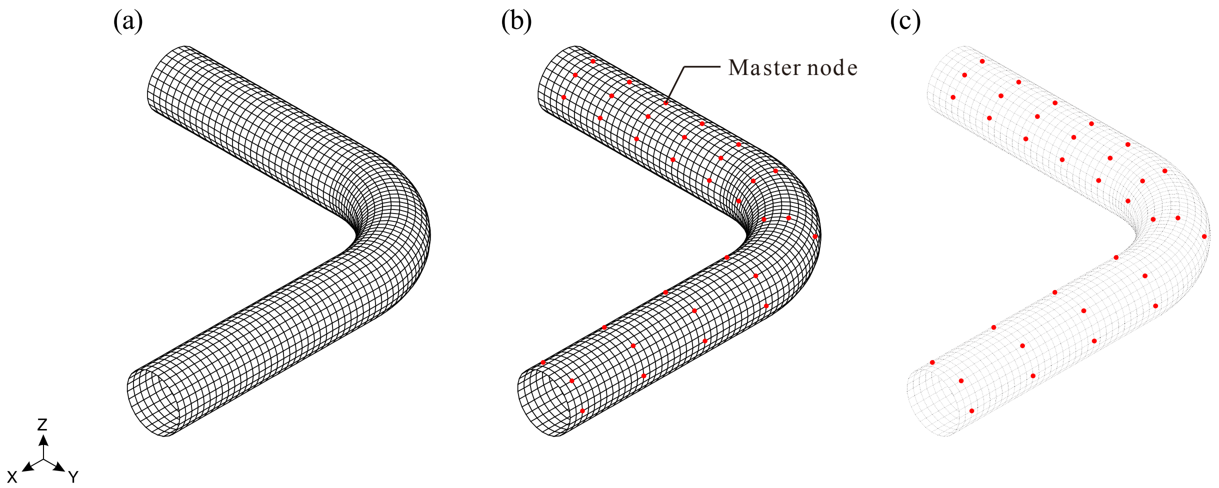

Figure 2.3 Reduction procedure of IRS method. (a) global structural FE model (b) selection of master nodes, (c) reduced model in the IRS method.

Chapter 3. Improved DCB method

In engineering practice, the degrees of freedom (DOFs) of numerical models have been continuously increased, along with the rapid increase in their complexity. When a complicated structure consisting with diverse components is designed through the cooperation of different engineers, it is very expensive to deal with its finite element models. This is because frequent design modifications affecting the whole and component models require repeated reanalysis. For these reasons, a number of model-reduction schemes have spotlighted its necessity, especially, in the structural dynamics community [1-11, 16-20, 26-58, 61-62]. Among the proposed solutions, component mode synthesis (CMS) methods are considered very powerful solutions. With CMS methods, the assemblage of small substructures represents a large structural model; then is approximated using a reduced model constructed using only the dominant substructural modes. In CMS methods, it is important to select the proper dominant modes [2, 21-23].

After pioneering work by Hurty [1] in the 1960s, numerous CMS methods have been introduced for various applications [1-11, 26-44, 61]. The CMS methods can be classified as fixed, free, and mixed-interface based methods, depending on how the interface is handled. The most successful fixed-interface based method is the Craig-Bampton method (CB method) [3] due to its simplicity, robustness, and accuracy. In contrast, the free-interface based methods [5-7, 9-10] proposed earlier were not successful because those methods were not adequate for either accuracy or efficiency in spite of their important advantages. These included such as substructural independence and easy treatment of various interface conditions [26-39].

In 2004, Rixen [9] introduced a new free-interface based method as a dual counterpart of the CB method, namely, the dual Craig-Bampton (DCB) method. In the DCB method, Lagrange multipliers are employed along the interface for assembling substructures and thus an original assembled finite element (FE) model can be effectively reduced as a form of quasi-diagonal matrices, leading to computational efficiency. The most advantageous feature of the DCB method is that, when a substructure is changed, entire reduced matrices do not need be updated again because in the formulation, substructures are handled independently. This feature also makes it possible to assemble substructures even if their FE meshes do not match along the interface [29]. For all these reasons, the DCB method is an attractive solution for experimental-FE model correlation [31-32, 36], as well as FE model updating and dynamic analysis considering various constraint conditions (contact, connection joint, damage, etc.) [37-39]. However, the DCB method still needs improvement in accuracy. In particular, the DCB method causes a weakening of the interface compatibility in reduced models, resulting in spurious modes with negative eigenvalues [9, 26]. If the reduction basis chosen is not sufficient, such spurious modes may occur in lower modes, which is an obstacle to approximating the original FE model correctly.

Recently, fixed-interface based CMS methods have been successfully improved considering the higher-order effect of the residual modes [8, 40-41, 43-44]. The motivation of this study is that the same principle can be adopted for improving free-interface based methods. In this study, we focus on improving the accuracy of the DCB method. We derive a new transformation matrix for the DCB method, improved by considering the second order effect of residual substructural modes. One difficulty comes from the fact that the improved approximation of substructural dynamic behavior contains unknown eigenvalues. In the formulation, unknown eigenvalues are considered additional generalized coordinates. These are subsequently eliminated using the concept of the system equivalent reduction expansion process (SEREP) to reduce computational cost. Finally, improved solution-accuracy is obtained in the final reduced systems. Furthermore, the use of the present method avoids creation of spurious modes with negative eigenvalues in the lower modes.

The formulation of the improved DCB method is presented in Section 3.1. Section 3.2 describes the performance of the improved DCB method through various numerical examples and in Section 3.3, we explore the negative eigenvalues in lower modes for the original and improved DCB methods.

3.1 Formulation

In the original DCB method [9], to construct the transformation matrix $\mathbf{T}_1$ in Eq. (2.25), the residual substructural modes are considered through the static flexibility matrix $\mathbf{K}^{(k)^+}$. However, in order to improve the DCB method, we here properly consider the effect of the residual substructural modes using dynamic flexibility, resulting in improved solution accuracy in the reduced models.

3.1.1 Second order dynamic residual flexibility

Let us consider Eq. (2.11) with $\mathbf{f}^{(k)} = \mathbf{0}$, and invoking harmonic response ($d^2/dt^2 = -\lambda$). The displacement of the k^{th} substructure can be written as

$$\mathbf{u}^{(k)} = -(\mathbf{K}^{(k)} - \lambda\mathbf{M}^{(k)})^{-1}\mathbf{B}^{(k)}\boldsymbol{\mu}, \ \ i = 1, \cdots, N_s, \tag{3.1}$$

in which $(\mathbf{K}^{(k)} - \lambda\mathbf{M}^{(k)})^{-1}$ is called the dynamic flexibility matrix. Using free-interface normal modes and rigid body modes obtained from Eq. (2.15), the dynamic flexibility matrix can be rewritten in terms of modal parameters

$$(\mathbf{K}^{(k)} - \lambda\mathbf{M}^{(k)})^{-1} = \boldsymbol{\Phi}^{(k)}(\boldsymbol{\Lambda}^{(k)} - \lambda\mathbf{I}^{(k)})^{-1}\boldsymbol{\Phi}^{(k)^T} \ \ \text{with} \ \ \boldsymbol{\Phi}^{(k)} = [\boldsymbol{\Theta}^{(k)} \quad \mathbf{R}^{(k)}]. \tag{3.2}$$

Substituting Eq. (3.2) into Eq. (3.1), the substructural displacement is represented by

$$\begin{gathered}\mathbf{u}^{(k)} = -\boldsymbol{\Theta}^{(k)}(\boldsymbol{\Lambda}_n^{(k)} - \lambda\mathbf{I}_n^{(k)})^{-1}\boldsymbol{\Theta}^{(k)^T}\mathbf{B}^{(k)}\boldsymbol{\mu} + \mathbf{R}^{(k)}\boldsymbol{\alpha}^{(k)} \\ \text{with} \ \ \boldsymbol{\Lambda}_n^{(k)} = \boldsymbol{\Theta}^{(k)^T}\mathbf{K}^{(k)}\boldsymbol{\Theta}^{(k)}, \ \ \mathbf{I}_n^{(k)} = \boldsymbol{\Theta}^{(k)^T}\mathbf{M}^{(k)}\boldsymbol{\Theta}^{(k)},\end{gathered} \tag{3.3}$$

in which $\boldsymbol{\Lambda}_n^{(k)}$ and $\mathbf{I}_n^{(k)}$ are the eigenvalue and identity matrices corresponding to the free-interface normal modes, and λ is the unknown eigenvalue.

We then substitute Eq. (2.16) into Eq. (3.3), to obtain

$$\mathbf{u}^{(k)} = \mathbf{\Theta}_d^{(k)}\mathbf{q}_d^{(k)} - \mathbf{\Theta}_r^{(k)}(\mathbf{\Lambda}_r^{(k)} - \lambda\mathbf{I}_r^{(k)})^{-1}\mathbf{\Theta}_r^{(k)^T}\mathbf{B}^{(k)}\boldsymbol{\mu} + \mathbf{R}^{(k)}\boldsymbol{\alpha}^{(k)} \tag{3.4}$$

$$\text{with } \mathbf{\Theta}_d^{(k)}\mathbf{q}_d^{(k)} = -\mathbf{\Theta}_d^{(k)}(\mathbf{\Lambda}_d^{(k)} - \lambda\mathbf{I}_d^{(k)})^{-1}\mathbf{\Theta}_d^{(k)^T}\mathbf{B}^{(k)}\boldsymbol{\mu}.$$

In Eq. (3.4), the residual part of the dynamic flexibility matrix $\mathbf{\Theta}_r^{(k)}(\mathbf{\Lambda}_r^{(k)} - \lambda\mathbf{I}_r^{(k)})^{-1}\mathbf{\Theta}_r^{(k)^T}$ can be expanded using a Taylor series [8, 10, 27, 40-48]

$$\mathbf{\Theta}_r^{(k)}(\mathbf{\Lambda}_r^{(k)} - \lambda\mathbf{I}_r^{(k)})^{-1}\mathbf{\Theta}_r^{(k)^T} = \mathbf{F}_1^{(k)} + \lambda\mathbf{F}_2^{(k)} + \cdots\lambda^{k-1}\mathbf{F}_j^{(k)} + \cdots \tag{3.5}$$

$$\text{with } \mathbf{F}_j^{(k)} = \mathbf{\Theta}_r^{(k)}\mathbf{\Lambda}_r^{(k)^{-j}}\mathbf{\Theta}_r^{(k)^T},$$

where $\mathbf{F}_j^{(k)}$ is the j^{th} order residual flexibility matrix of the k^{th} substructure.

Considering the residual flexibility up to the second order, the residual part of the dynamic flexibility matrix is approximated by

$$\mathbf{\Theta}_r^{(k)}(\mathbf{\Lambda}_r^{(k)} - \lambda\mathbf{I}_r^{(k)})^{-1}\mathbf{\Theta}_r^{(k)^T} \approx \mathbf{F}_1^{(k)} + \lambda\mathbf{F}_2^{(k)}, \tag{3.6}$$

and using Eq. (3.6) in Eq. (3.4), the substructural displacement is expressed as

$$\mathbf{u}^{(k)} \approx \mathbf{\Theta}_d^{(k)}\mathbf{q}_d^{(k)} - \mathbf{F}_1^{(k)}\mathbf{B}^{(k)}\boldsymbol{\mu} - \lambda\mathbf{F}_2^{(k)}\mathbf{B}^{(k)}\boldsymbol{\mu} + \mathbf{R}^{(k)}\boldsymbol{\alpha}^{(k)}. \tag{3.7}$$

Note that the substructural displacement of the original DCB formulation is obtained when the second order residual flexibility in Eq. (3.7) is ignored. The added second order residual flexibility contributes to strengthening the interface compatibility by more precisely calculating the displacement due to the interconnecting forces. As a result, it is expected that the emergence of spurious modes can be avoided in the lower modes. This feature will be briefly demonstrated using a numerical example. The second order residual flexibility matrix can be easily calculated by reusing $\mathbf{F}_1^{(k)}$ in Eq. (2.23)

$$\mathbf{F}_2^{(k)} = \mathbf{F}_1^{(k)}\mathbf{M}^{(k)}\mathbf{F}_1^{(k)}. \tag{3.8}$$

The substructural transformation matrix $\overline{\mathbf{T}}_2^{(k)}$ with the second order residual flexibility approximation is given by

$$\begin{bmatrix} \mathbf{u}^{(k)} \\ \boldsymbol{\mu} \end{bmatrix} \approx \overline{\mathbf{T}}_2^{(k)} \mathbf{u}_2^{(k)}, \tag{3.9}$$

with $\overline{\mathbf{T}}_2^{(k)} = \left[\begin{array}{cc:cc} \mathbf{R}^{(k)} & \boldsymbol{\Theta}_d^{(k)} & -\mathbf{F}_1^{(k)}\mathbf{B}^{(k)} & \overline{\boldsymbol{\Theta}}_2^{(k)} \\ \mathbf{0} & \mathbf{0} & \mathbf{I} & \mathbf{0} \end{array}\right]$, $\mathbf{u}_2^{(k)} = \begin{bmatrix} \boldsymbol{\alpha}^{(k)} \\ \mathbf{q}_d^{(k)} \\ \hdashline \boldsymbol{\mu} \\ \boldsymbol{\psi} \end{bmatrix}$, $\overline{\boldsymbol{\Theta}}_2^{(k)} = -\mathbf{F}_2^{(k)}\mathbf{B}^{(k)}$, $\boldsymbol{\psi} = \lambda\boldsymbol{\mu}$,

where $\mathbf{u}_2^{(k)}$ denotes the generalized coordinate vector and $\boldsymbol{\psi}$ is the additional coordinate vector containing the unknown eigenvalue λ .

It is important to note that the use of higher-order residual flexibility may produce badly scaled transformation matrices, resulting in ill-conditioned reduced system matrices. Thus, we normalize each column of $\overline{\boldsymbol{\Theta}}_2^{(k)}$ using its L2-norm [63-64].

$$\boldsymbol{\Theta}_2^{(k)} = \overline{\boldsymbol{\Theta}}_2^{(k)} \mathbf{G}^{(k)^{-1}} \quad \text{with} \quad \mathbf{G}^{(k)} = \begin{bmatrix} \left\| \{\overline{\boldsymbol{\theta}}_2^{(k)}\}_1 \right\|_2 & & & \mathbf{0} \\ & \left\| \{\overline{\boldsymbol{\theta}}_2^{(k)}\}_2 \right\|_2 & & \\ & & \ddots & \\ \mathbf{0} & & & \left\| \{\overline{\boldsymbol{\theta}}_2^{(k)}\}_{N_b} \right\|_2 \end{bmatrix}, \tag{3.10}$$

where $\boldsymbol{\Theta}_2^{(k)}$ is the normalized residual mode matrix containing the second order residual flexibility, and $\{\overline{\boldsymbol{\theta}}_2^{(k)}\}_j$ is the j^{th} column vector of $\overline{\boldsymbol{\Theta}}_2^{(i)}$.

Substituting Eq. (3.10) into Eq. (3.9), the substructural transformation matrix of the improved DCB method for the k^{th} substructure is

$$\begin{bmatrix} \mathbf{u}^{(k)} \\ \boldsymbol{\mu} \end{bmatrix} \approx \mathbf{T}_2^{(k)} \mathbf{u}_2^{(k)} \quad \text{with} \quad \mathbf{T}_2^{(k)} = \left[\begin{array}{cc|cc} \mathbf{R}^{(k)} & \boldsymbol{\Theta}_d^{(k)} & -\mathbf{F}_1^{(k)}\mathbf{B}^{(k)} & \boldsymbol{\Theta}_2^{(k)} \\ \mathbf{0} & \mathbf{0} & \mathbf{I} & \mathbf{0} \end{array}\right]. \tag{3.11}$$

Then, the displacement and Lagrange multipliers of the original assembled FE model with N_s substructures are approximated as

$$\begin{bmatrix} \mathbf{u} \\ \boldsymbol{\mu} \end{bmatrix} \approx \mathbf{T}_2 \left[\begin{array}{c} \boldsymbol{\alpha}^{(1)} \\ \vdots \\ \boldsymbol{\alpha}^{(N_s)} \\ \mathbf{q}_d^{(1)} \\ \vdots \\ \mathbf{q}_d^{(N_s)} \\ \hline \boldsymbol{\mu} \\ \boldsymbol{\psi} \end{array}\right] \tag{3.12}$$

$$\text{with} \quad \mathbf{T}_2 = \left[\begin{array}{cccccc|cc} \mathbf{R}^{(1)} & & \mathbf{0} & \boldsymbol{\Theta}_d^{(1)} & & \mathbf{0} & -\mathbf{F}_1^{(1)}\mathbf{B}^{(1)} & \boldsymbol{\Theta}_2^{(1)} \\ & \ddots & & & \ddots & & \vdots & \vdots \\ \mathbf{0} & & \mathbf{R}^{(N_s)} & \mathbf{0} & & \boldsymbol{\Theta}_d^{(N_s)} & -\mathbf{F}_1^{(N_s)}\mathbf{B}^{(N_s)} & \boldsymbol{\Theta}_2^{(N_s)} \\ \mathbf{0} & \cdots & \mathbf{0} & \mathbf{0} & \cdots & \mathbf{0} & \mathbf{I} & \mathbf{0} \end{array}\right]$$

Using the transformation matrix $\mathbf{T}_2$ ($N_g \times N_2$) in Eq. (3.12), the reduced system matrices ($N_2 \times N_2$) and force vector ($N_2 \times 1$) are calculated

$$\overline{\mathbf{M}}_2 = \mathbf{T}_2^T \begin{bmatrix} \mathbf{M} & \mathbf{0} \\ \mathbf{0} & \mathbf{0} \end{bmatrix} \mathbf{T}_2, \; \overline{\mathbf{K}}_2 = \mathbf{T}_2^T \begin{bmatrix} \mathbf{K} & \mathbf{B} \\ \mathbf{B}^T & \mathbf{0} \end{bmatrix} \mathbf{T}_2, \; \bar{\mathbf{f}}_2 = \mathbf{T}_2^T \begin{bmatrix} \mathbf{f} \\ \mathbf{0} \end{bmatrix}, \tag{3.13}$$

in which $\overline{\mathbf{M}}_2$, $\overline{\mathbf{K}}_2$, and $\bar{\mathbf{f}}_2$ are the reduced mass and stiffness matrices, and the reduced force vector, respectively. Note that N_2 is the number of DOFs in the reduced FE model, $N_2 = 2N_\mu + \sum_{k=1}^{N_s} \left(N_r^{(k)} + N_d^{(k)} \right)$.

3.1.2 Interface reduction

When the second order residual flexibility is considered, the size of reduced system is increased due to the additional coordinates $\boldsymbol{\psi}$ compared to the original DCB method [9]. The number of increased DOFs is equal to the number of Lagrange multipliers.

To resolve this problem, we eliminate the additional coordinates by employing the concept of the system equivalent reduction expansion process (SEREP) [18]. In the global eigenvalue problem given in Eq. (2.13), the eigenvalues related to the Lagrange multipliers $\boldsymbol{\mu}$ are non-physically infinite. When original FE models are reduced using the original and improved DCB methods in Eq. (2.26) and (3.13), respectively, such non-physical eigenvalues related to $\boldsymbol{\mu}$ and $\boldsymbol{\psi}$ ($\boldsymbol{\psi} = \lambda\boldsymbol{\mu}$) become finite, but appear in higher modes. The modes related to the additional coordinates can be eliminated through a further reduction using SEREP.

From the reduced system matrices in Eq. (3.13), the following eigenvalue problem is obtained:

$$\overline{\mathbf{K}}_2(\overline{\boldsymbol{\varphi}})_i = \overline{\lambda}_i\overline{\mathbf{M}}_2(\overline{\boldsymbol{\varphi}})_i, \quad i = 1, \cdots, N_2, \tag{3.14}$$

where $\overline{\lambda}_i$ and $(\overline{\boldsymbol{\varphi}})_i$ are the i^{th} eigenvalue and the corresponding mode vector, respectively. We then calculate the eigenvectors up to the N_1-th mode and construct the following eigenvector matrix

$$\overline{\boldsymbol{\Phi}} = \begin{bmatrix}(\overline{\boldsymbol{\varphi}})_1 & (\overline{\boldsymbol{\varphi}})_2 & \cdots & (\overline{\boldsymbol{\varphi}})_{N_1}\end{bmatrix}. \tag{3.15}$$

The transformation matrix of the improved DCB method [44] is further reduced using the eigenvector matrix in Eq. (3.15) as follows.

$$\hat{\mathbf{T}}_2 = \mathbf{T}_2\overline{\boldsymbol{\Phi}}, \tag{3.16}$$

and thus the new transformation matrix $\hat{\mathbf{T}}_2$ has the same size as $\mathbf{T}_1$ in the original DCB method ($N_g \times N_1$). That is, the additional coordinate vector $\boldsymbol{\psi}$ is eliminated.

Finally, the resulting reduced system matrices are calculated as follows:

$$\hat{\mathbf{M}}_2 = \hat{\mathbf{T}}_2^T \begin{bmatrix} \mathbf{M} & \mathbf{0} \\ \mathbf{0} & \mathbf{0} \end{bmatrix} \hat{\mathbf{T}}_2, \ \hat{\mathbf{K}}_2 = \hat{\mathbf{T}}_2^T \begin{bmatrix} \mathbf{K} & \mathbf{B} \\ \mathbf{B}^T & \mathbf{0} \end{bmatrix} \hat{\mathbf{T}}_2, \ \hat{\mathbf{f}}_2 = \hat{\mathbf{T}}_2^T \begin{bmatrix} \mathbf{f} \\ \mathbf{0} \end{bmatrix}, \tag{3.17}$$

in which $\hat{\mathbf{M}}_2$, $\hat{\mathbf{K}}_2$, and $\hat{\mathbf{f}}_2$ are the final reduced mass, stiffness matrices, and force vector, respectively. Then, the size of the reduced system matrices provided by the improved DCB method [44] becomes equal to that by the original DCB method [9].

The reduced eigenvalue problem of the present method is given by

$$\hat{\mathbf{K}}_2(\hat{\boldsymbol{\varphi}})_i = \hat{\lambda}_i \hat{\mathbf{M}}_2(\hat{\boldsymbol{\varphi}})_i, \ i = 1, 2, \cdots, N_1, \tag{3.18}$$

where $\hat{\lambda}_i$ and $(\hat{\boldsymbol{\varphi}})_i$ are the approximated i^{th} eigenvalues and corresponding eigenvectors in the present method.

The approximated global eigenvector $(\overline{\boldsymbol{\varphi}}_g)_i$ can be calculated by

$$(\overline{\boldsymbol{\varphi}}_g)_i = \hat{\mathbf{T}}_2(\hat{\boldsymbol{\varphi}})_i. \tag{3.19}$$

The reduced system becomes more accurate by improving the DCB formulation. The increase of computational cost is inevitable, but the computation of the second order residual flexibility is effectively performed using Eq. (3.8). In the present method, it is possible to independently perform the process for each substructure from construction to reduction. Since we do not have to deal with the global FE model, we can efficiently reduce the large structural FE model. The flow chart of the present reduction method is shown in the Fig. 3.1.

In the following sections, the accuracy and computational cost is investigated using various numerical examples. In the numerical examples, the computation cost for the interface reduction process also be examined.

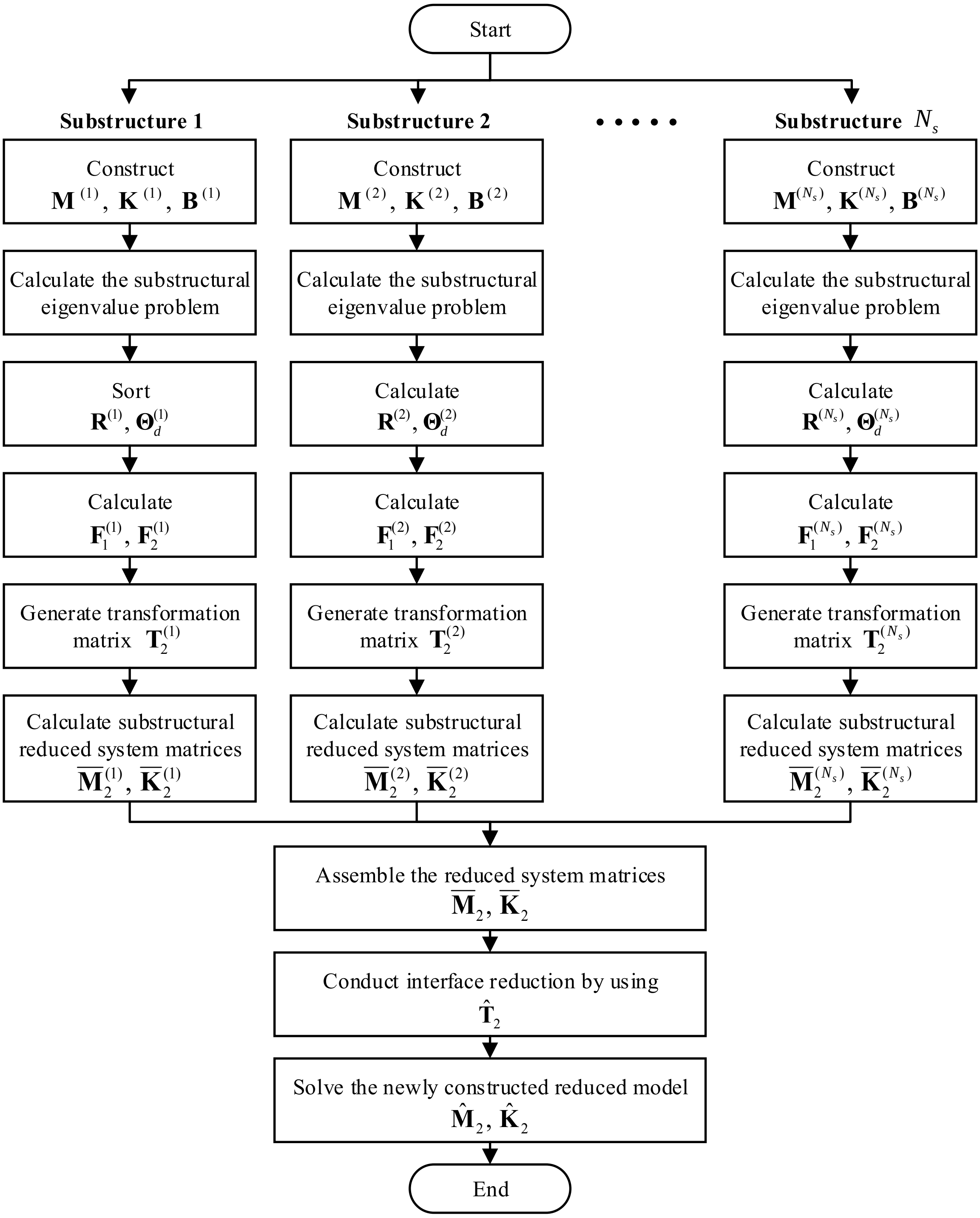

Figure 3.1 Flow chart for the FE model reduction in the improved DCB method

3.2 Numerical examples

In this section, we investigate the performance of the improved DCB method compared to the original DCB method. We considered six structural problems: a rectangular plate with matching and non-matching meshes, a plate with a hole, a hyperboloid shell, a bended pipe, a NACA 2415 wing with ailerons, and a cable-stayed bridge.

FE models are constructed using the 4-node MITC (Mixed Interpolation of Tensorial Components) shell elements [65-70], 3D solid elements and truss elements, and free or fixed boundary conditions are imposed differently according to the problem. The frequency cut-off method is employed to select dominant substructural modes [21-23]. All the computer codes are implemented in MATLAB and computation is performed in a personal computer (Inter core (TM) i7-4770, 3.40 GHz CPU, 32 GB RAM).

The relative eigenfrequency error is adopted to measure the accuracy of the reduced models

$$\xi_i = \frac{|\omega_i - \hat{\omega}_i|}{\omega_i} \quad \text{with} \quad \omega_i = \sqrt{\lambda_i}\,,\ \ \hat{\omega}_i = \sqrt{\hat{\lambda}_i} \tag{3.20}$$

in which ξ_i is the i^{th} relative eigenfrequency error, ω_i is the i^{th} exact eigenfrequency calculated from the global eigenvalue problem in Eq. (2.13); and $\hat{\omega}_i$ is the i^{th} approximated eigenfrequency from the reduced eigenvalue problem in Eq. (3.18). Note that the rigid body modes are not considered in measuring the accuracy.

The accuracy of approximated eigenvectors of the original and improved DCB method are measured by the modal assurance criterion (MAC) [59-60] as

$$\mathrm{MAC}(i,j) = \frac{|(\boldsymbol{\varphi}_g)_i^T(\overline{\boldsymbol{\varphi}}_g)_j|^2}{((\boldsymbol{\varphi}_g)_i^T(\boldsymbol{\varphi}_g)_i)((\overline{\boldsymbol{\varphi}}_g)_j^T(\overline{\boldsymbol{\varphi}}_g)_j)} \quad \text{for} \quad i,j = 1,2,\cdots,N_1, \tag{3.21}$$

in which $(\boldsymbol{\varphi}_g)$ and $(\overline{\boldsymbol{\varphi}}_g)$ are the global and approximated eigenvector, respectively. The resulting scalars are assembled into the MAC matrix. The MAC indicate the consistency between eigenvectors by its value from zero to unity. If the MAC has a value near unity, the eigenvectors are considered consistent. Note that the rigid body modes are not considered in measuring the consistency of eigenvectors.

3.2.1 Rectangular plate problem

Let us consider a rectangular plate with free boundary, see Fig. 3.2. Length L is 0.6096 m, width B is 0.3048 m, and thickness h is 3.18×10^{-3} m. Young's modulus E is 72 GPa, Poisson's ratio ν is 0.33, and density ρ is 2796 $\mathrm{kg/m^3}$. The whole structure is an assemblage of two substructures ($N_s = 2$) modeled by 4-node MITC shell elements. We consider two numerical cases, with matching and non-matching meshes between neighboring substructures.

For the matching mesh case, the first substructure is modeled using an 8×6 mesh and the second substructure is modeled using a 4×6 mesh, as shown in Fig. 3.2a. Fig. 3.3 presents the relative eigenfrequency errors obtained by the CB, the original and improved DCB methods. The numbers of dominant modes used and the numbers of DOFs in original and reduced systems are listed in Table 3.1. The improved DCB method shows significantly improved accuracy compared to the original CB method.

Let us consider the non-matching mesh case, see Fig. 3.2b. The first substructure is modeled by an 8×6 mesh and the second substructure is modeled by an 8×12 mesh. In this case, the interface compatibility is considered through nodal collocation and thus the matrices $\mathbf{B}^{(i)}$ are no longer Boolean, see Fig. 3.2c. Fig. 3.4 presents the relative eigenfrequency errors obtained by the original and improved DCB methods. Table 3.2 shows the numbers of dominant modes used and the numbers of DOFs in the original and reduced systems. The results also show that the improved method provides considerably more-accurate solutions for this non-matching mesh case.

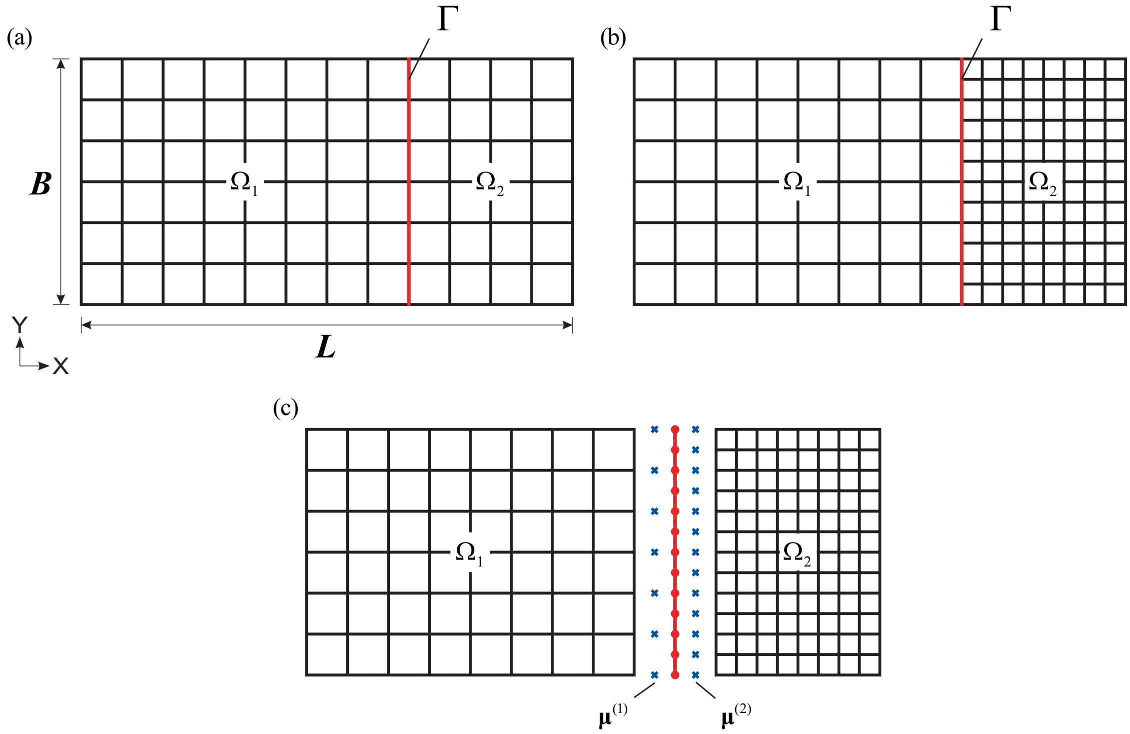

Figure 3.2 Rectangular plate problem: (a) Matching mesh on the interface (12×6 mesh), (b) Non-matching mesh between neighboring substructures, (c) Interface boundary treatment.

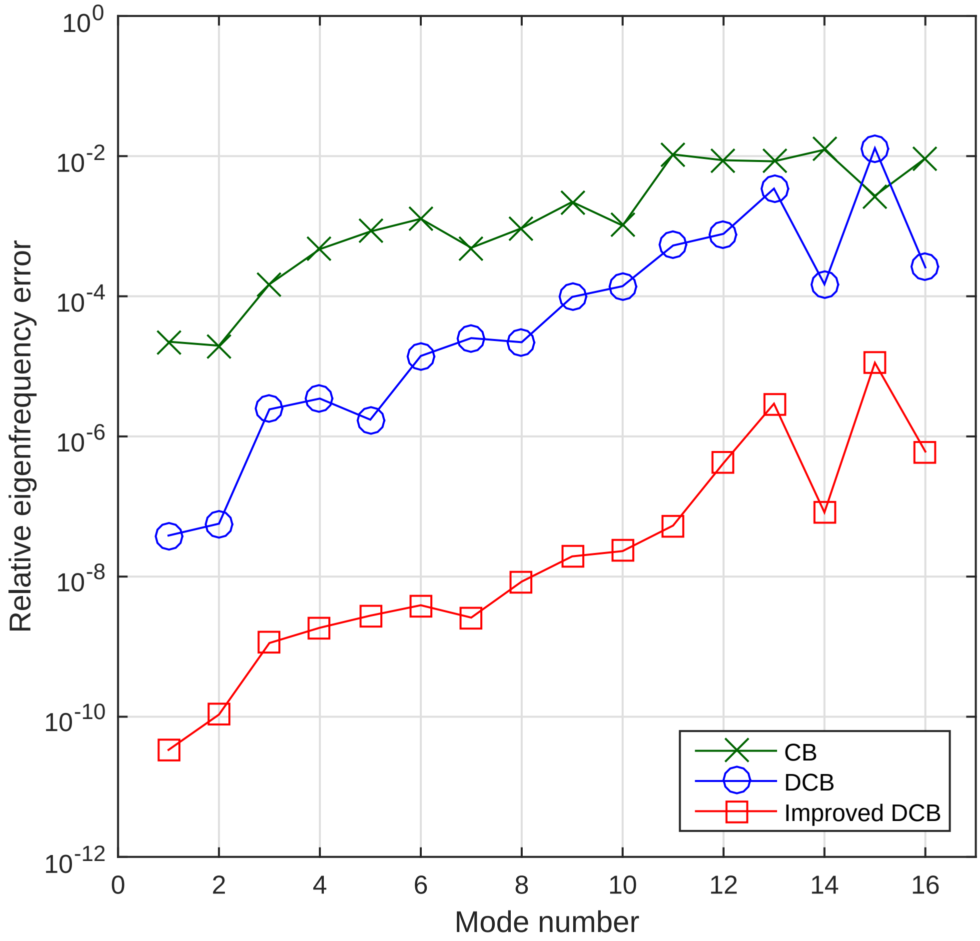

Figure 3.3 Relative eigenfrequency errors in the rectangular plate problem with matching mesh.

Table 3.1 Number of dominant modes used and number of DOFs in original and reduced systems for the rectangular plate problem (12×6 mesh).

Methods	$N_d^{(1)}$	$N_d^{(2)}$	N_d	N_g	N_1
CB	13	7	20	455	55
DCB	13	7	20	525	67
Improved DCB	13	7	20	525	67

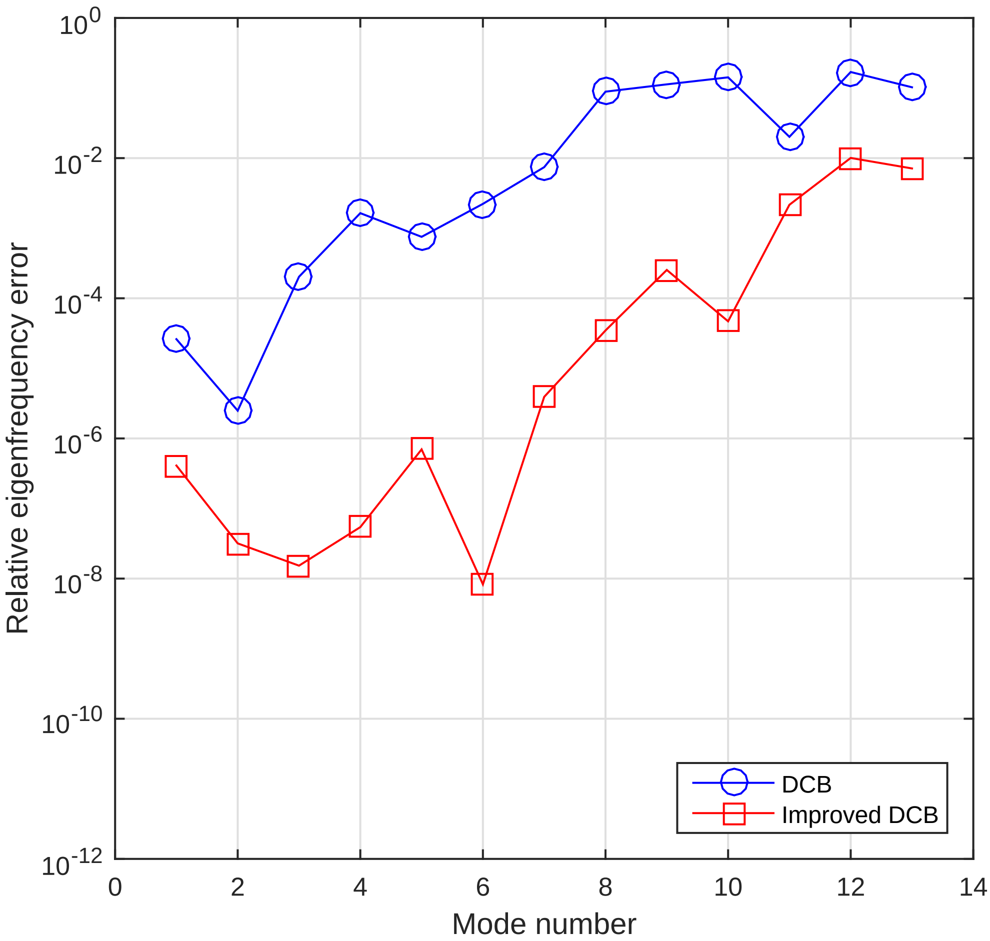

Figure 3.4. Relative eigenfrequency errors in the rectangular plate problem with non-matching mesh.

Table 3.2. Number of dominant modes used and number of DOFs in original and reduced systems for the rectangular plate problem with non-matching mesh.

Methods	$N_d^{(1)}$	$N_d^{(2)}$	N_d	N_g	N_1
DCB	5	3	8	965	85
Improved DCB	5	3	8	965	85

3.2.2 Plate structure with a hole

Let us consider a rectangular plate with a hole, see Fig. 3.5. No boundary condition is imposed. The length L is 20 m, width B is 10 m, and thickness h is 0.25 m. Young's modulus E is 210 GPa, Poisson's ratio ν is 0.3, and density ρ is 7850 $\mathrm{kg/m^3}$. The whole model is an assemblage of four substructural FE models ($N_s = 4$). The whole model is discretized by 208 shell elements (1360 DOFs). The substructures are symmetrically positioned about the hole in center.

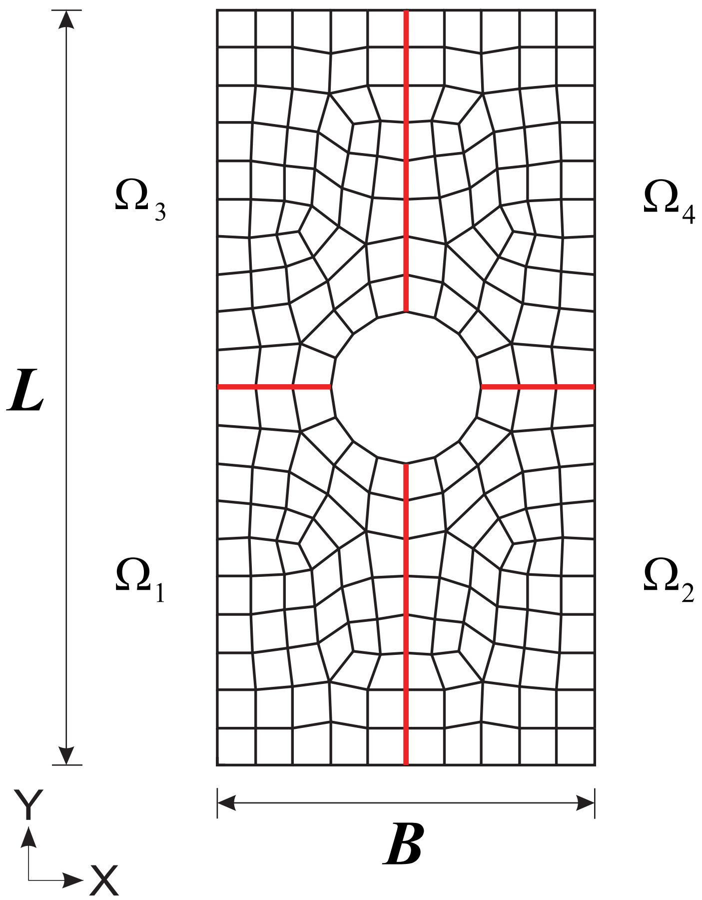

Figure 3.5. Plate structure with a hole.

The numbers of dominant modes used and the numbers of DOFs in the original and reduced systems are presented in Table 3.3. Fig. 3.6 presents the relative eigenfrequency errors obtained using the original and improved DCB methods. The results show that the improved DCB method largely outperforms the original DCB method, especially, in lower modes.

Fig. 3.7 presents the MAC for reduced system by the original and improved DCB method. The results from both methods show that the approximated eigenvectors in the improved DCB method have more accurate consistency than the original DCB method.

Table 3.3. Number of dominant modes used and number of DOFs in original and reduced systems for the plate structure with a hole.

Methods	$N_d^{(1)}$	$N_d^{(2)}$	$N_d^{(3)}$	$N_d^{(4)}$	N_d	N_g	N_1
DCB	5	5	5	5	20	1490	174
Improved DCB	5	5	5	5	20	1490	174

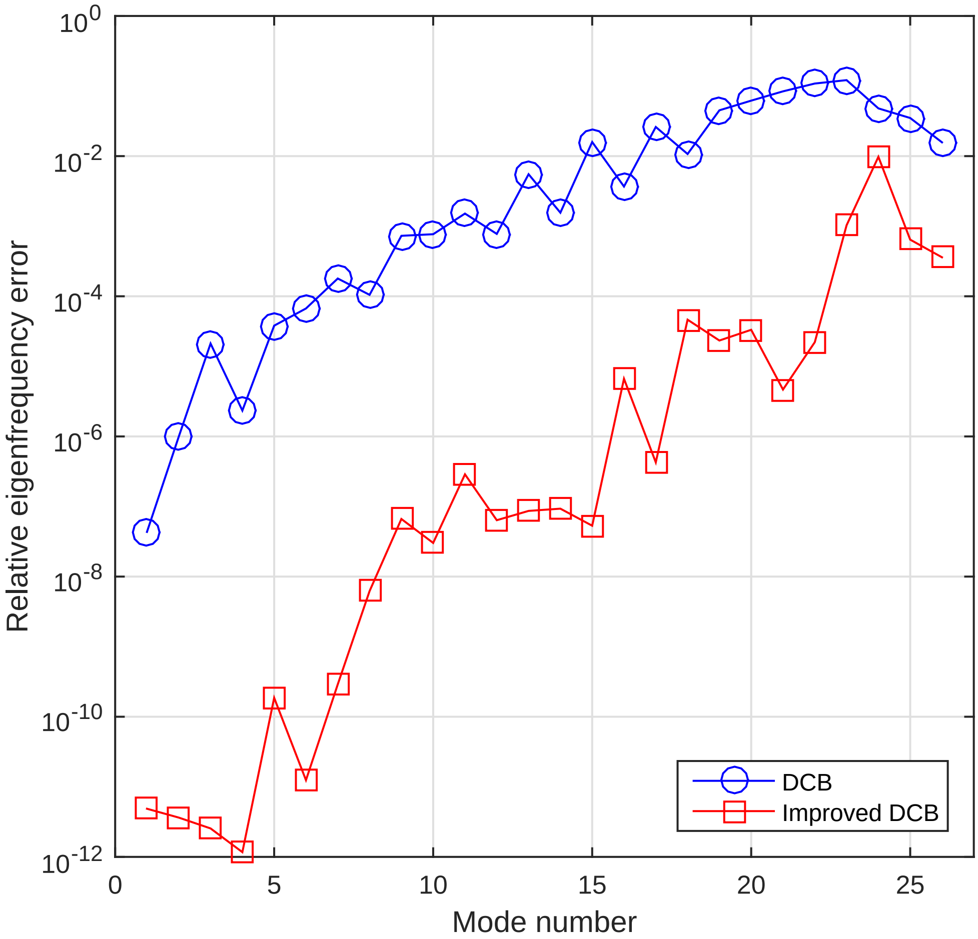

Figure 3.6. Relative eigenfrequency errors in the plate structure with a hole.

(a)

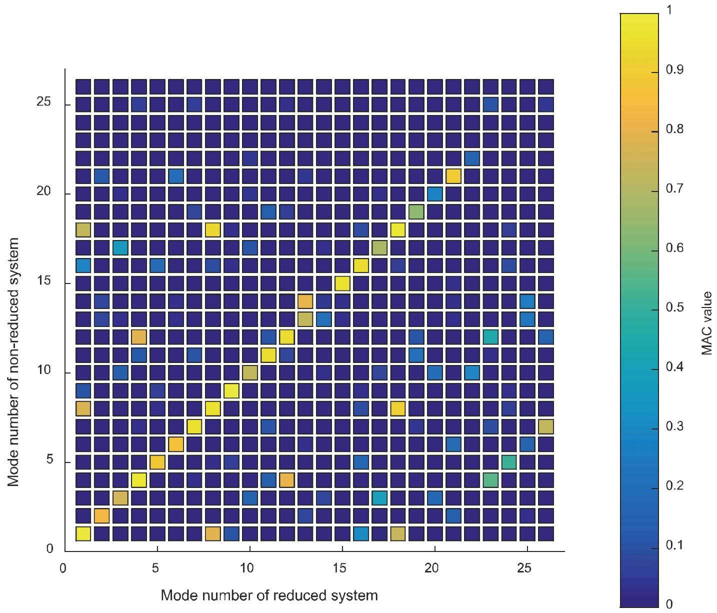

(b)

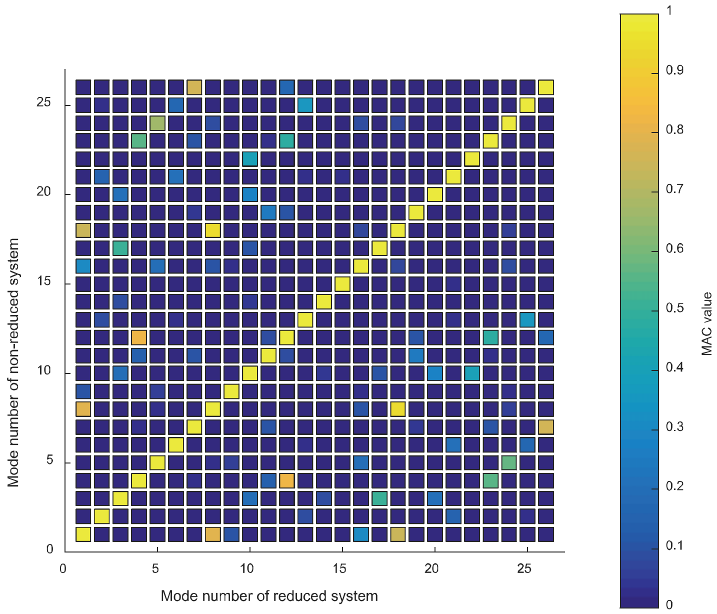

Figure 3.7. MAC for reduced system in the plate structure with a hole: (a) DCB method, (b) Improved DCB method

3.2.3 Hyperboloid shell problem

We here consider a hyperboloid shell structure with free boundary as shown in Fig. 3.8. Height H is 4.0 m and thickness h is 0.05 m. Young's modulus E is 69 GPa, Poisson's ratio ν is 0.35, and density ρ is 2700 $\mathrm{kg/m^3}$. The mid-surface of this shell structure is described by

$$x^2 + y^2 = 2 + z^2; \quad z \in [-2,2]. \tag{3.22}$$

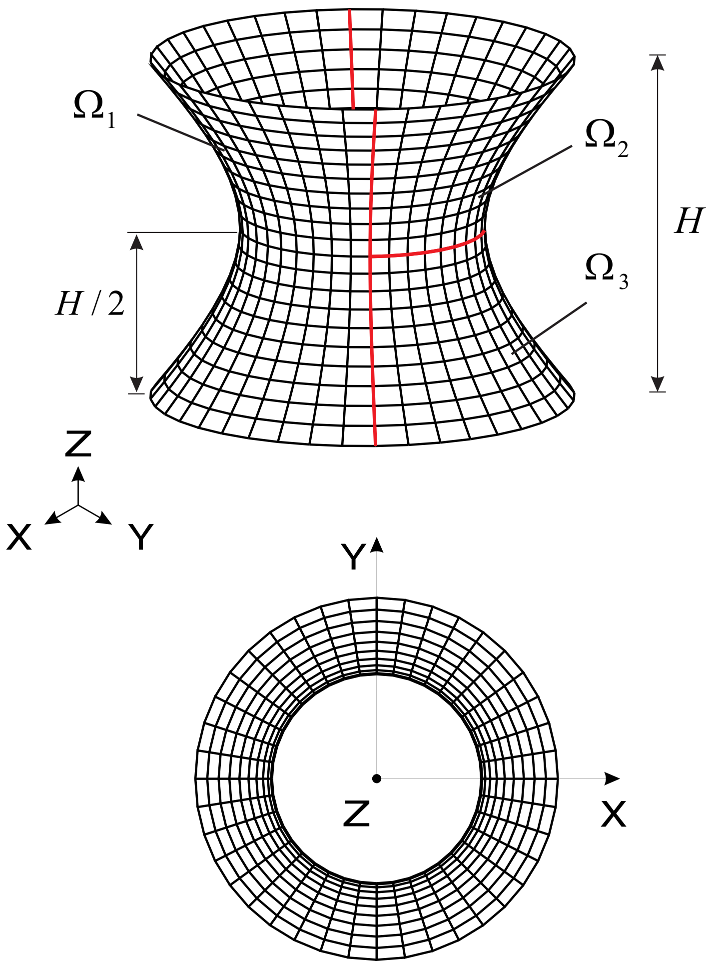

Figure 3.8. Hyperboloid shell problem.

Three substructures ($N_s = 3$) are assembled to construct the original FE model of the shell structures, in which 800 shell elements and 903 nodes are used (4200 DOFs). Table 3.4 lists the numbers of dominant modes used and the numbers of DOFs in the original and reduced systems. Fig. 3.9 presents the relative eigenfrequency errors obtained using the original and improved DCB methods. The graphs in the figure consistently show the accuracy of the improved DCB method.

Fig. 3.10 presents the MAC for reduced system by the original and improved DCB method. The results show that the approximated eigenvectors obtained with the improved DCB method give better consistency.

For this problem, we also compare the computational costs of the original and improved DCB methods. Table 3.5 shows the detailed computational costs. Compared to the original DCB method, the additional computation time required by the improved DCB method is 3.69% for accuracy improvement, and 13.25% for interface reduction.

Table 3.4. Number of dominant modes used and number of DOFs in original and reduced systems for the hyperboloid shell problem.

Methods	$N_d^{(1)}$	$N_d^{(2)}$	$N_d^{(3)}$	N_d	N_g	N_1
DCB	10	10	10	30	4830	363
Improved DCB	10	10	10	30	4830	363

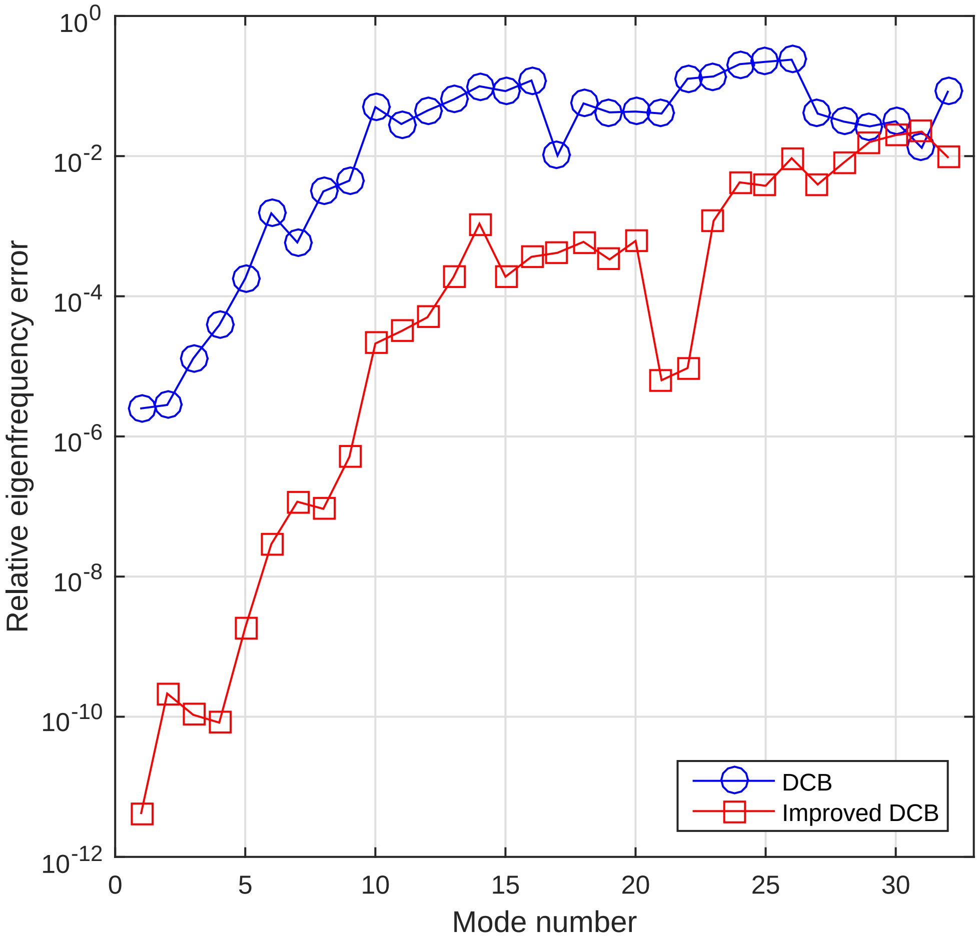

Figure 3.9. Relative eigenfrequency errors in the hyperboloid shell problem.

(a)

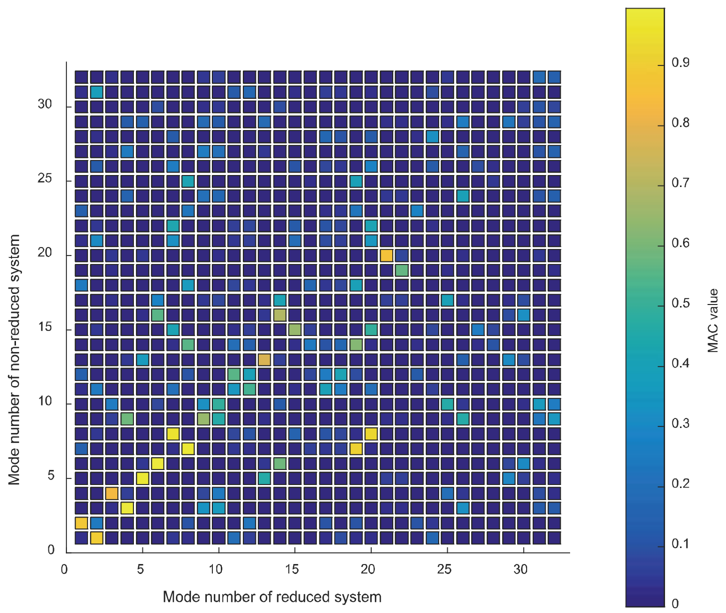

(b)

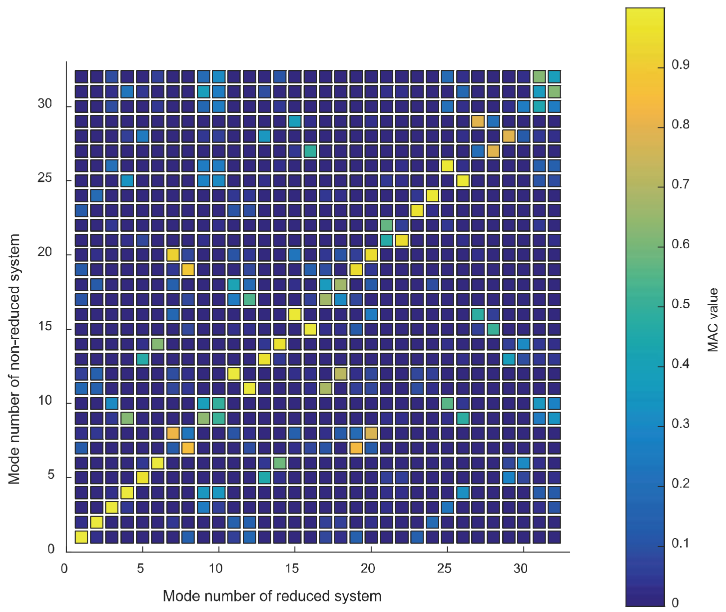

Figure 3.10. MAC for reduced system in the hyperboloid shell problem: (a) DCB method, (b) Improved DCB method

Table 3.5. Computational costs for the hyperboloid shell problem.

Methods	Items	Computation times [sec]	Ratio [%]
Original DCB method	Substructural mode matrices ($\mathbf{R}^{(i)}, \mathbf{\Theta}_d^{(i)}$)	0.28	1.77
	Substructural 1st order residual flexibility matrices ($\mathbf{F}_1^{(i)}$)	15.11	96.94
	Reduced system matrices ($\overline{\mathbf{M}}_1, \overline{\mathbf{K}}_1$)	0.20	1.29
	Total	15.59	100.00
Improved DCB method	Substructural mode matrices ($\mathbf{R}^{(i)}, \mathbf{\Theta}_d^{(i)}$)	0.28	1.77
	Substructural 1st order residual flexibility matrices ($\mathbf{F}_1^{(i)}$)	15.11	96.94
	Substructural 2nd order residual flexibility matrices ($\mathbf{F}_2^{(i)}$)	0.36	2.31
	Reduced system matrices ($\overline{\mathbf{M}}_2, \overline{\mathbf{K}}_2$)	0.42	2.67
	Subtotal	16.17	103.69
	Interface reduction ($\hat{\mathbf{M}}_2, \hat{\mathbf{K}}_2$)	2.06	13.25
	Total	18.23	116.94

3.2.4 Bended pipe problem

A bended pipe structure with clamped boundary at one end is considered as shown in Fig. 3.11, in which the structural configuration and specification are illustrated. Young's modulus E is 69 GPa, Poisson's ratio ν is 0.35, and density ρ is 2700 $\mathrm{kg/m^3}$. The FE model of the pipe structure is an assemblage of three substructural FE models ($N_s = 3$). The whole FE model has 2511 shell elements and 2592 nodes (12960 DOFs).

The following numerical cases are considered:

- The original DCB method is used with the reduced model size of $N_1 = 297$ ($N_d = 15$) and $N_1 = 567$ ($N_d = 285$).
- The improved DCB method is used with the reduced model size of $N_1 = 297$ ($N_d = 15$).

The number of dominant modes used and the number of DOFs in the original and reduced systems are listed in Table 3.6.

Fig. 3.12 presents the relative eigenfrequency errors obtained by the original and improved DCB methods. When reduced models of the same size ($N_1 = 297$; $N_d = 15$) are considered, the improved DCB method provides a much more accurate reduced model. It is also observed that the original DCB method shows accuracy comparable to the improved DCB method when 285 modes are used for the original DCB. For similarly accurate reduced models, the model size obtained by the original DCB method ($N_1 = 567$) is almost twice that obtained by the improved DCB method ($N_1 = 297$).

Fig. 3.13 presents the MAC for reduced system by the original and improved DCB method ($N_d = 15$). In this case, the approximated eigenvectors obtained by the original DCB method hardly show consistency with the correct eigenvectors. However, the improved DCB method provides consistently accurate results.

Next, the computational costs of the original and improved DCB methods are compared. Table 3.7 shows the detailed computational costs. For reduced models of the same size, additional computation time required for the improved DCB method is 2.05% for accuracy improvement and 0.5% for interface reduction, compared to the original DCB method. The table also presents the detailed computation time when 285 modes are used for the original DCB method.

At this point, it is important to note that the improved DCB method is very useful for obtaining an accurate reduced model when only a limited number of dominant modes are available. Such cases happen when dominant modes are obtained experimentally.

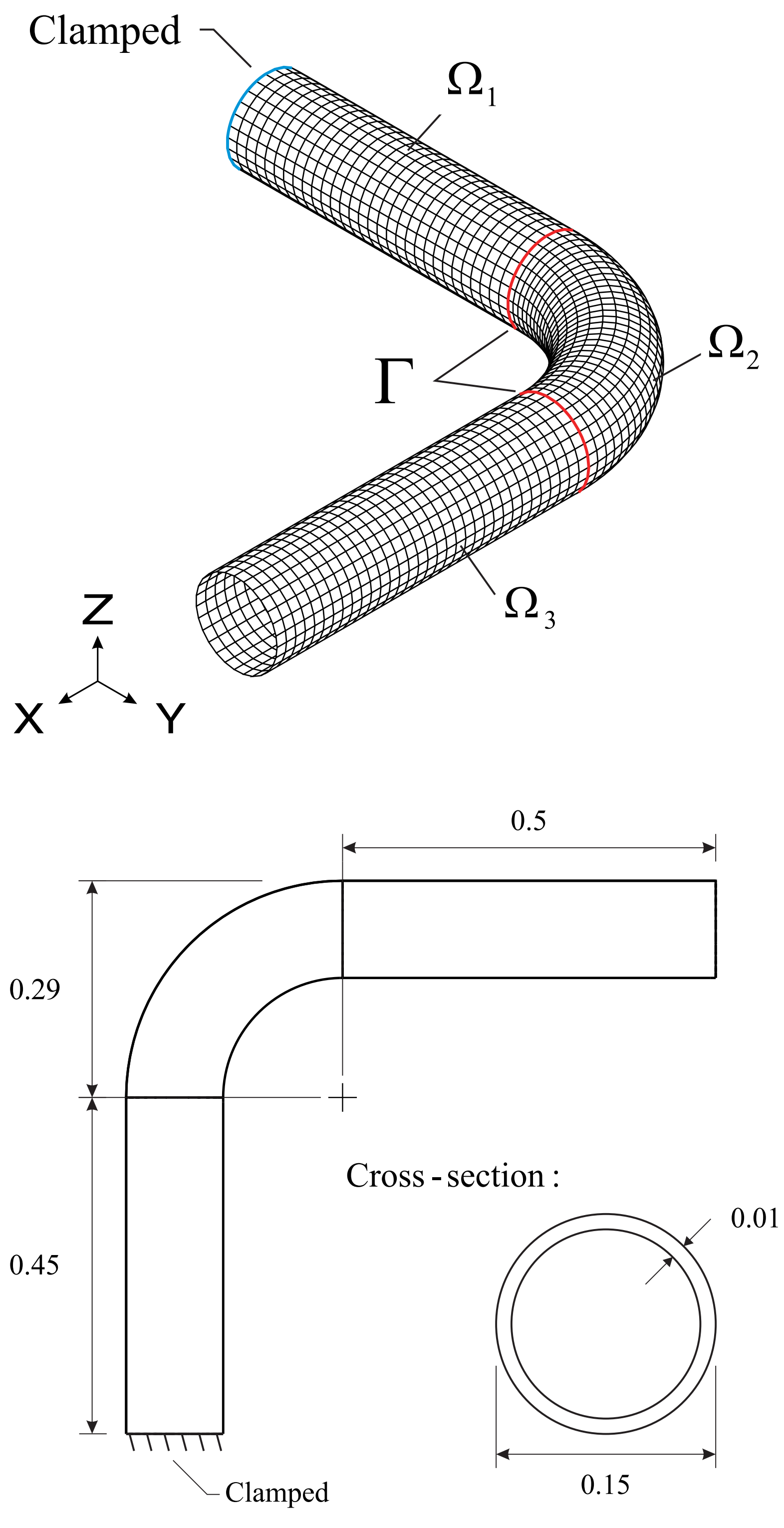

Figure 3.11. Bended pipe problem.

Table 3.6. Number of dominant modes used and number of DOFs in the original and reduced systems for the bended pipe problem.

Methods	$N_d^{(1)}$	$N_d^{(2)}$	$N_d^{(3)}$	N_d	N_g	N_1
DCB	5	5	5	15	13095	297
DCB	95	95	95	285	13095	567
Improved DCB	5	5	5	15	13095	297

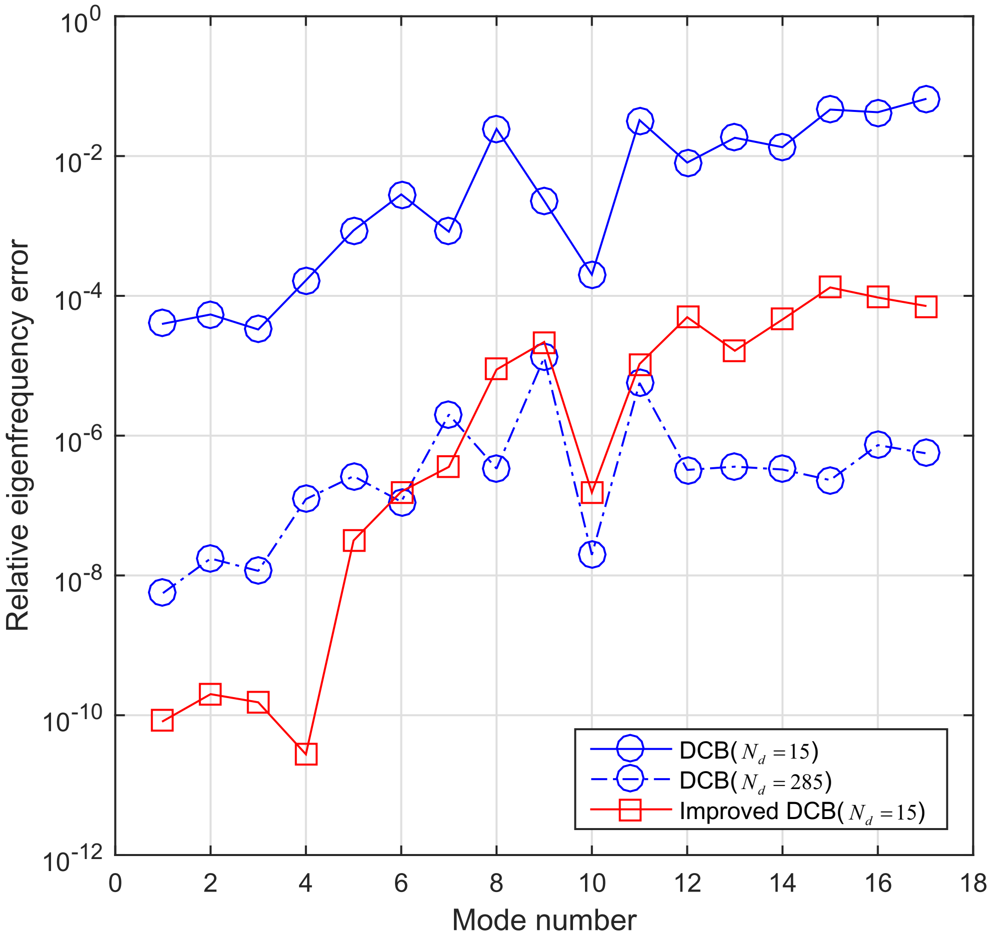

Figure 3.12. Relative eigenfrequency errors in the bended pipe problem.

(a)

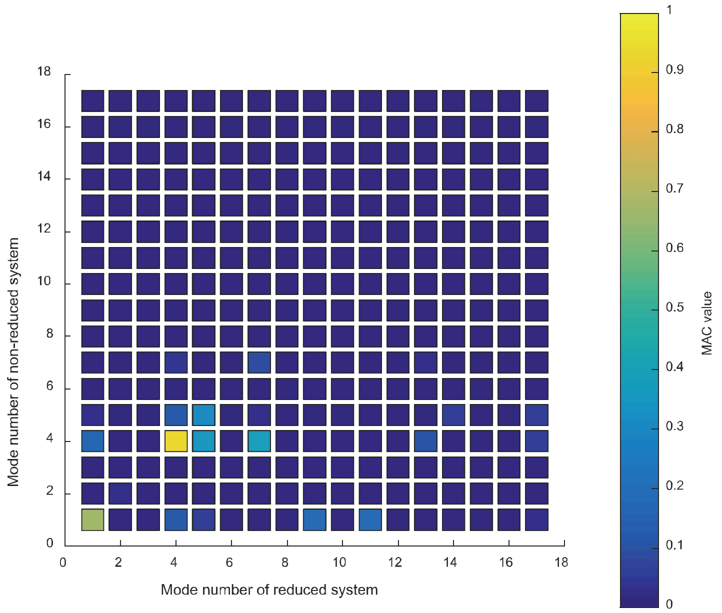

(b)

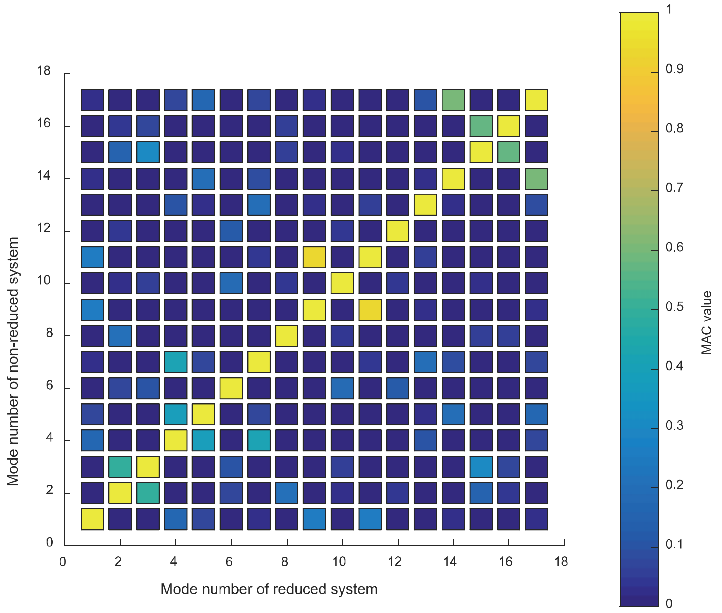

Figure 3.13. MAC for reduced system in the bended pipe problem ($N_d = 15$): (a) DCB method, (b) Improved DCB method

Table 3.7. Computational costs for the bended pipe problem.

Methods	Items	Computation times [sec]	Computation times Ratio [%]
Original DCB method ($N_d = 15$)	Substructural mode matrices ($\mathbf{R}^{(i)}, \mathbf{\Theta}_d^{(i)}$)	0.67	0.26
	Substructural 1st order residual flexibility matrices ($\mathbf{F}_1^{(i)}$)	256.40	99.44
	Reduced system matrices ($\overline{\mathbf{M}}_1, \overline{\mathbf{K}}_1$)	0.77	0.30
	Total	257.84	100.00
Original DCB method ($N_d = 285$)	Substructural mode matrices ($\mathbf{R}^{(i)}, \mathbf{\Theta}_d^{(i)}$)	3.61	1.40
	Substructural 1st order residual flexibility matrices ($\mathbf{F}_1^{(i)}$)	272.71	105.77
	Reduced system matrices ($\overline{\mathbf{M}}_1, \overline{\mathbf{K}}_1$)	0.81	0.31
	Total	277.13	107.48
Improved DCB method ($N_d = 15$)	Substructural mode matrices ($\mathbf{R}^{(i)}, \mathbf{\Theta}_d^{(i)}$)	0.67	0.26
	Substructural 1st order residual flexibility matrices ($\mathbf{F}_1^{(i)}$)	256.40	99.44
	Substructural 2nd order residual flexibility matrices ($\mathbf{F}_2^{(i)}$)	4.58	1.78
	Reduced system matrices ($\overline{\mathbf{M}}_2, \overline{\mathbf{K}}_2$)	1.46	0.57
	Subtotal	263.11	102.05
	Interface reduction ($\hat{\mathbf{M}}_2, \hat{\mathbf{K}}_2$)	1.29	0.50
	Total	264.40	102.55

3.2.5 NACA 2415 wing with ailerons problem

A NACA 2415 wing structure with clamped boundary at one end is considered as shown in Fig. 3.14, in which the structural configuration and specification are illustrated. The two ailerons are connected by a frictionless hinges to the first substructure. Due to the ailerons, the two rigid body modes are calculated in the eigenvalue analysis of both global and reduced eigenvalue problems. The modeling of hinge is simply implemented by the Lagrange multipliers.

The length L is 0.9144 m, width W is 0.2286 m, and thickness H is 0.0345 m. Young's modulus E is 71 GPa, Poisson's ratio ν is 0.33, and density ρ is 3000 $\mathrm{kg/m^3}$. The whole model is an assemblage of four substructural FE models ($N_s = 3$). The each substructure is discretized by 3873, 112 and 144 shell elements, respectively (19250, 725 and 925 DOFs).

Table 3.8 lists the numbers of dominant modes used and the numbers of DOFs in the original and reduced systems. Fig. 3.15 presents the relative eigenfrequency errors obtained using the original and improved DCB methods. The improved DCB method shows considerably accurate results for low-order modes with only the size of the reduce model corresponding to 1.15% of the total DOFs of global FE model.

Fig. 3.16 presents the MAC for reduced system by improved DCB method. The results show that the eigenvectors approximated by the improved DCB method maintain consistency with the global eigenvectors for each mode. The off-diagonal terms of the MAC occurring in the initial four normal modes are caused by the symmetry of the wing structure and the behavior close to the rigid body mode of the ailerons.

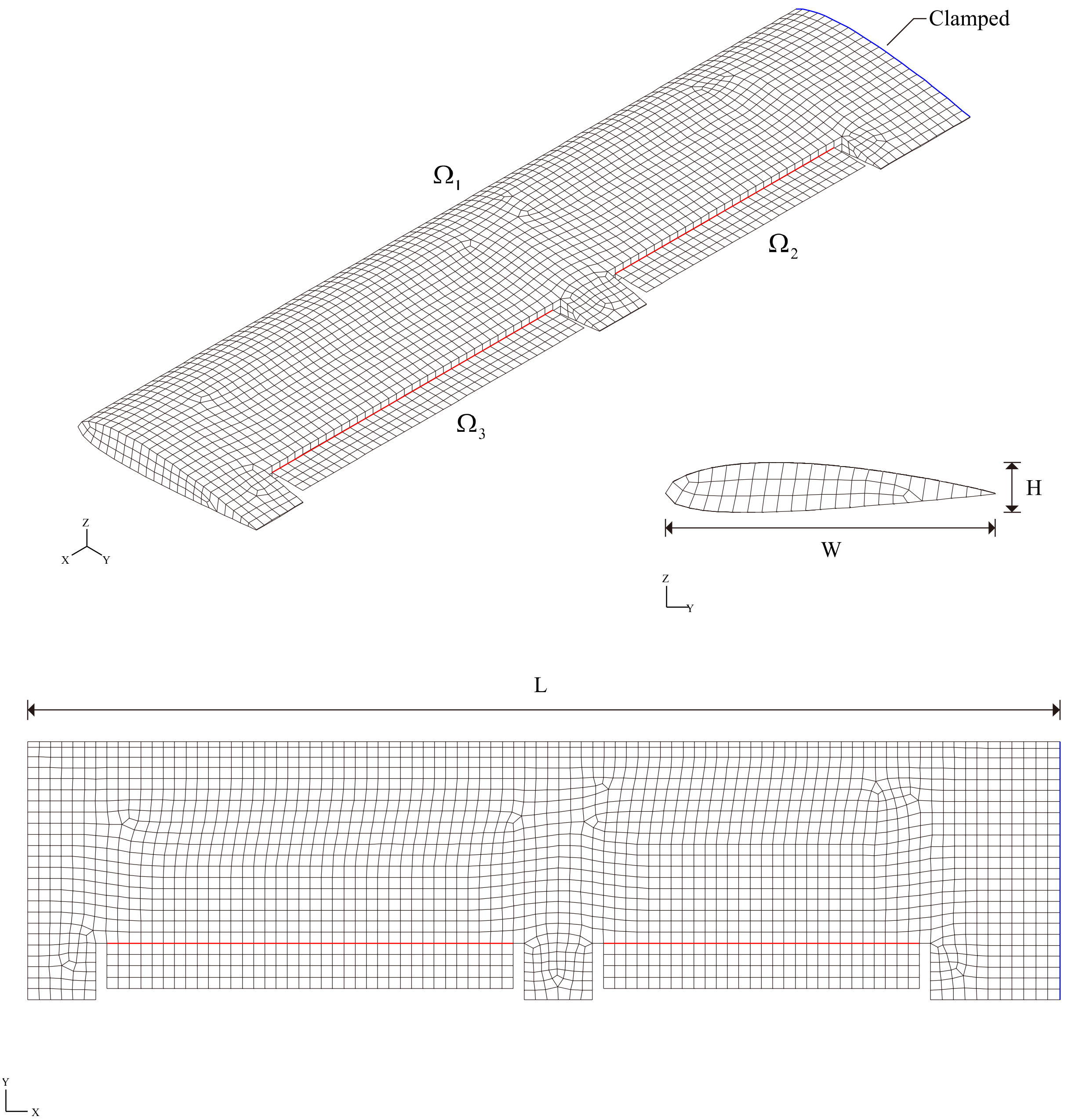

Figure 3.14. NACA 2415 wing with ailerons problem.

Table 3.8. Number of dominant modes used and number of DOFs in the original and reduced systems for the NACA 2415 wing with ailerons problem.

Methods	$N_d^{(1)}$	$N_d^{(2)}$	$N_d^{(3)}$	N_d	N_g	N_1
DCB	15	9	9	33	21098	243
Improved DCB	15	9	9	33	21098	243

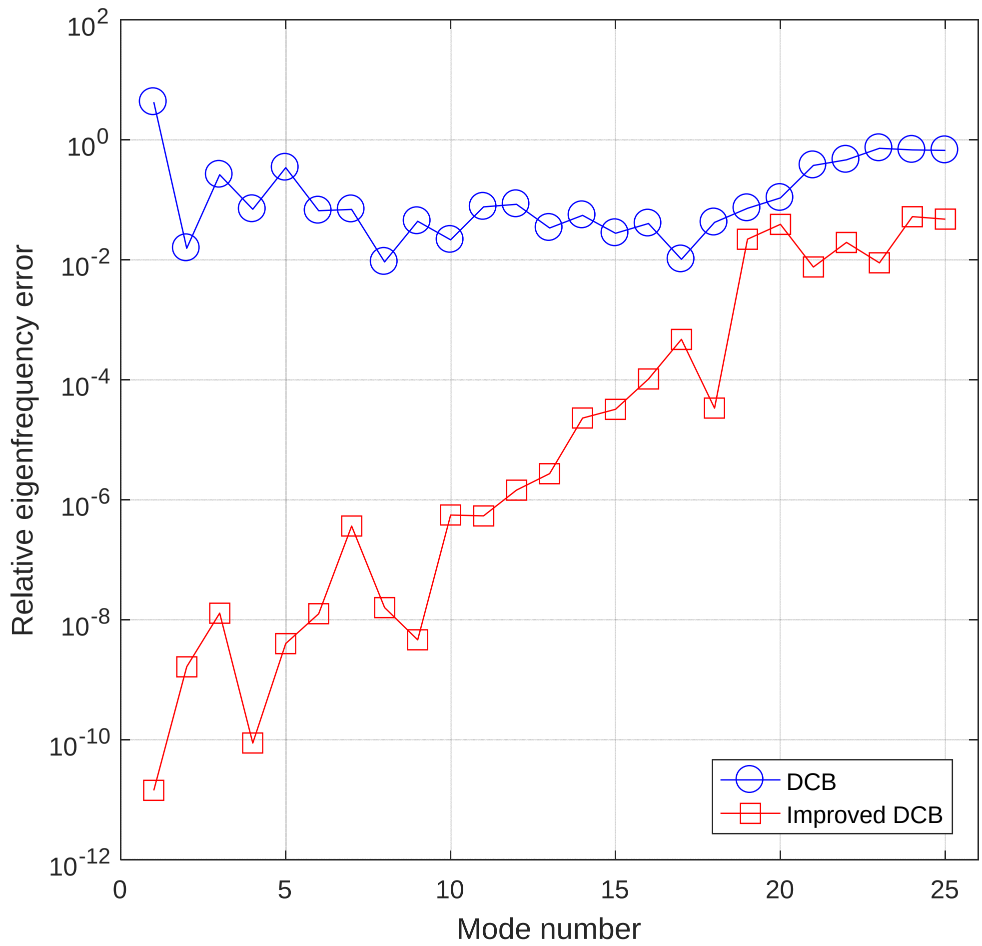

Figure 3.15. Relative eigenfrequency errors in the NACA 2415 wing with ailerons problem.

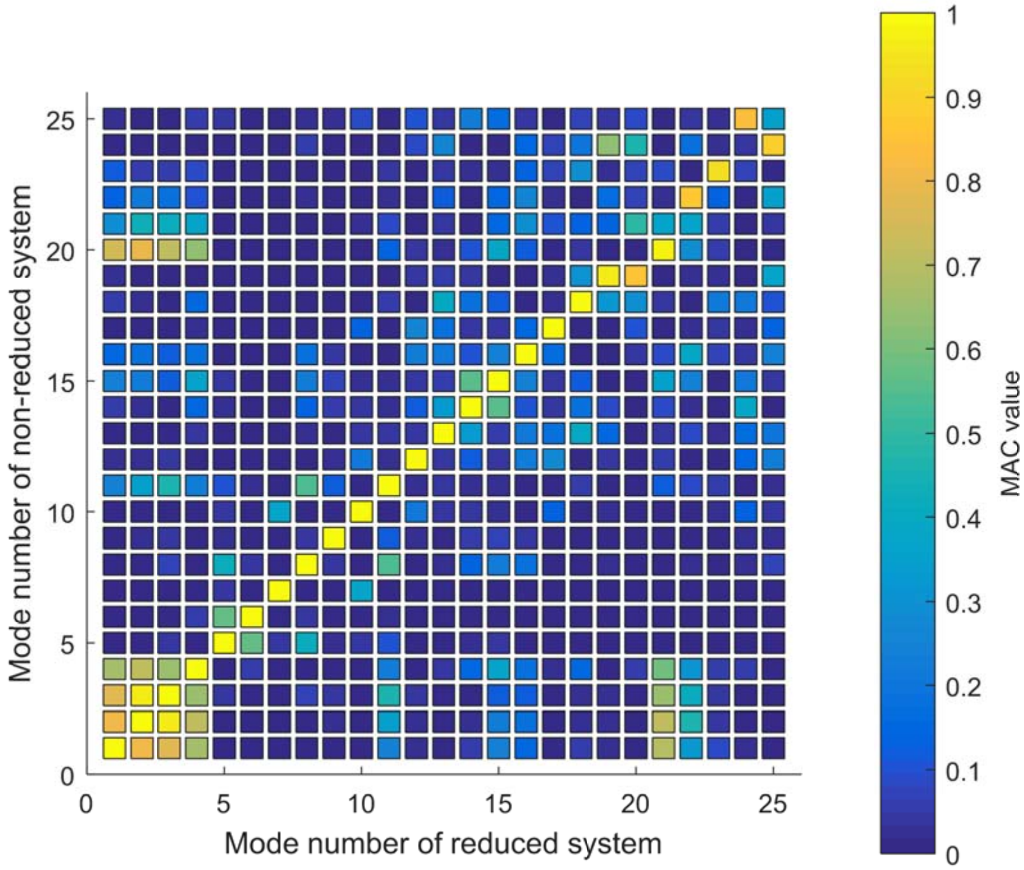

Figure 3.16. MAC for reduced system by the improved DCB method in the NACA 2415 wing with ailerons problem.

3.2.6 Cable-stayed bridge problem

We finally consider a cable-stayed bridge problem as shown in Fig. 3.17 and 3.18. The unit of length in this figure is feet (ft). The FE model and its mass and stiffness matrices are obtained by the well-known commercial FE analysis software, ADINA [70]. The structure is modeled using 504 shell elements for the girder, 50 3D solid elements for the tower, and 4 3D truss elements for the cable, respectively. The number of nodes is 1666, and total DOFs is 6878.

Here, we considered the bridge structure in Fig. 3.17 as one sub-structure and connected multiple substructures to make the long-span bridge structure as in Fig. 3.18. In this problem, we assemble the six substructures ($N_s = 6$), the dominant substructural modes, $N_d^{(i)} = 6$ is considered for each substructure. Then, the number of DOFs in the original assembled FE model (N_g) is 42293, and the number of DOFs in the reduced model (N_1) becomes 1061.

Fig. 3.19 presents the relative eigenfrequency errors obtained using the original and improved DCB methods. It is observed that the performance of the improved DCB method is much more accurate than the original DCB method. Fig. 3.20 presents the MAC for reduced system by original and improved DCB method. As expected, the results show that the eigenvector consistency of the improved DCB method is better than the original DCB method.

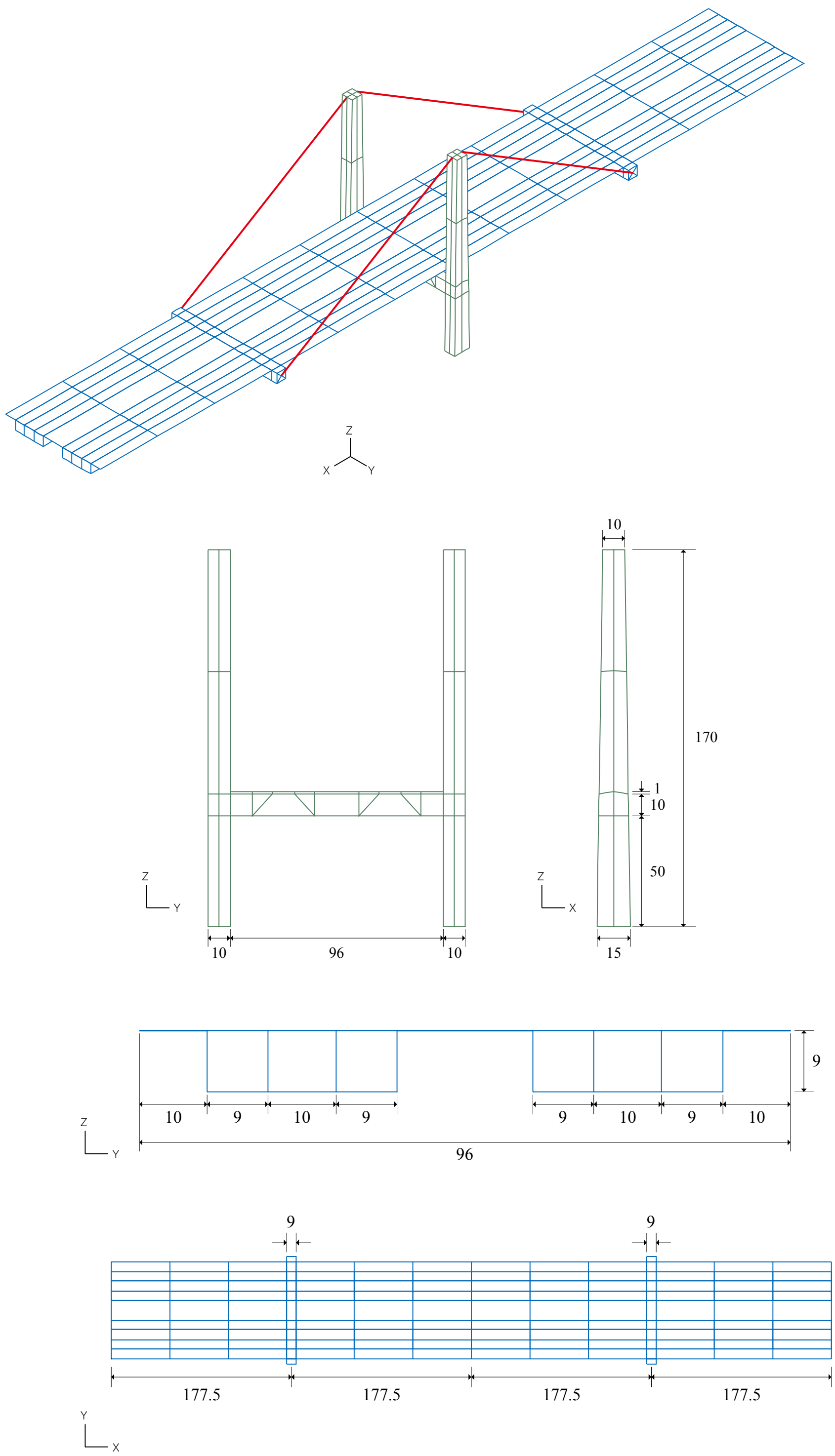

Figure 3.17. Cable-stayed bridge problem (1 substructure).

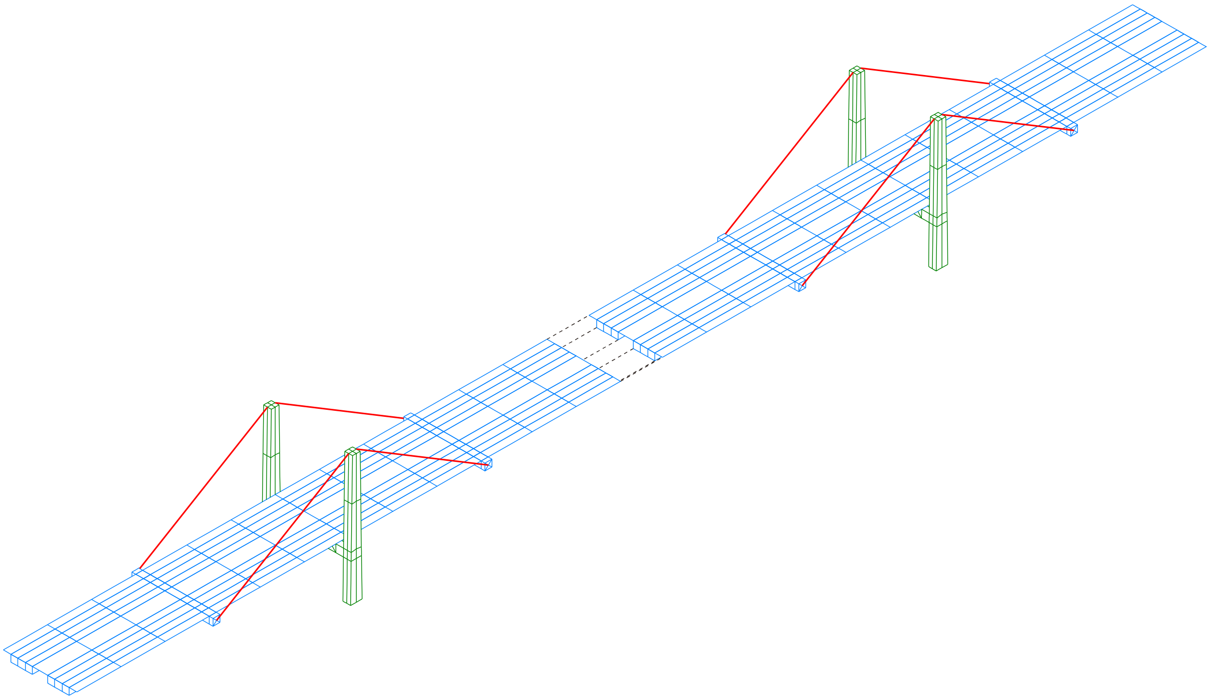

Figure 3.18. Connection of cable-stayed bridge substructures ($N_s = 2$).

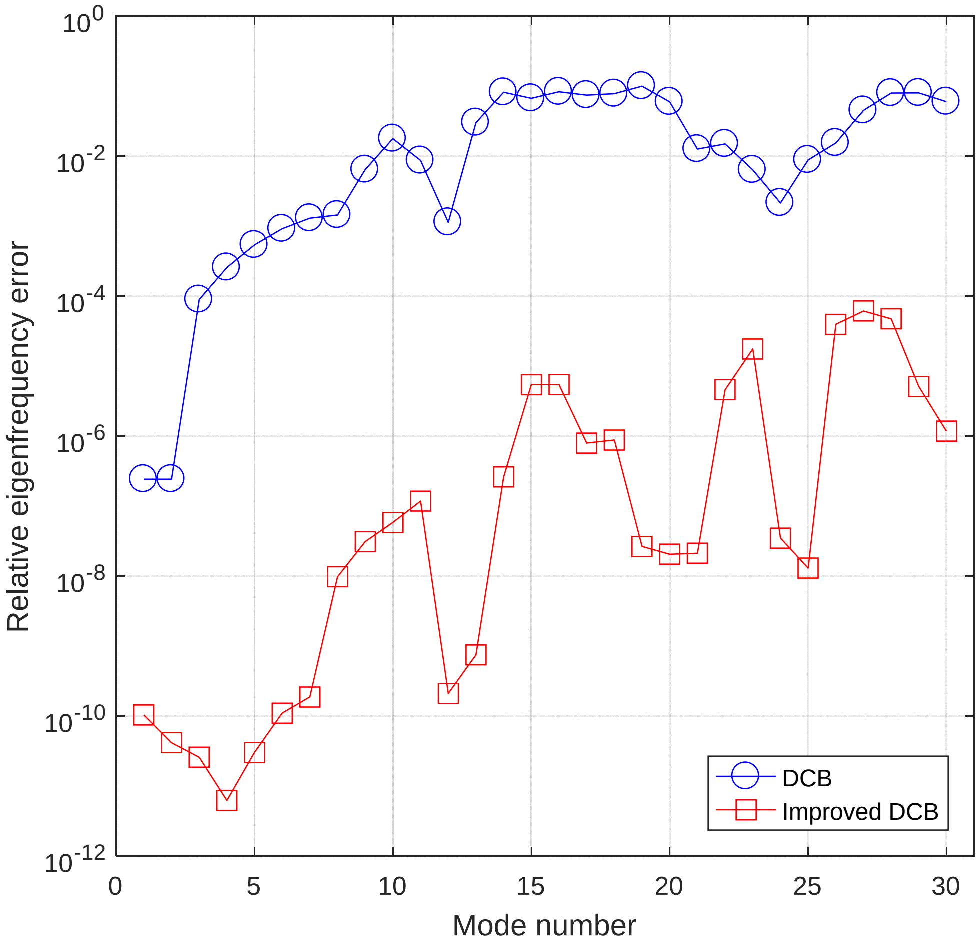

Figure 3.19. Relative eigenfrequency errors in the cable-stayed bridge problem ($N_s = 6$).

(a)

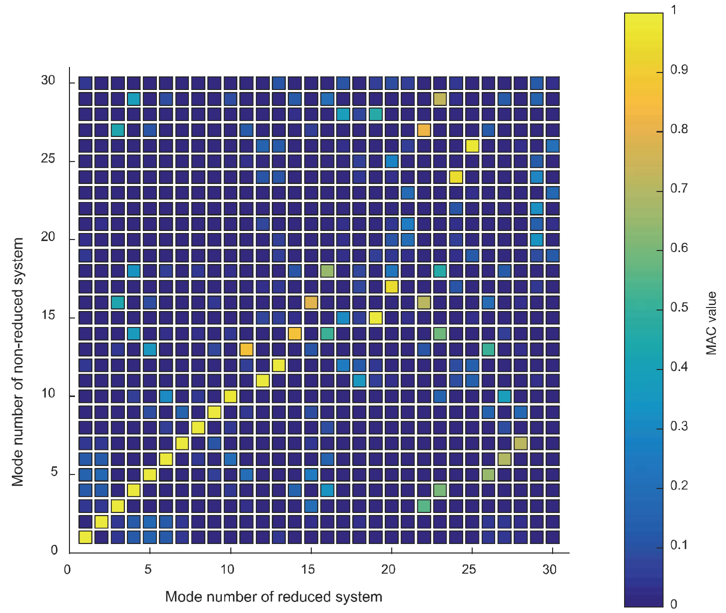

(b)

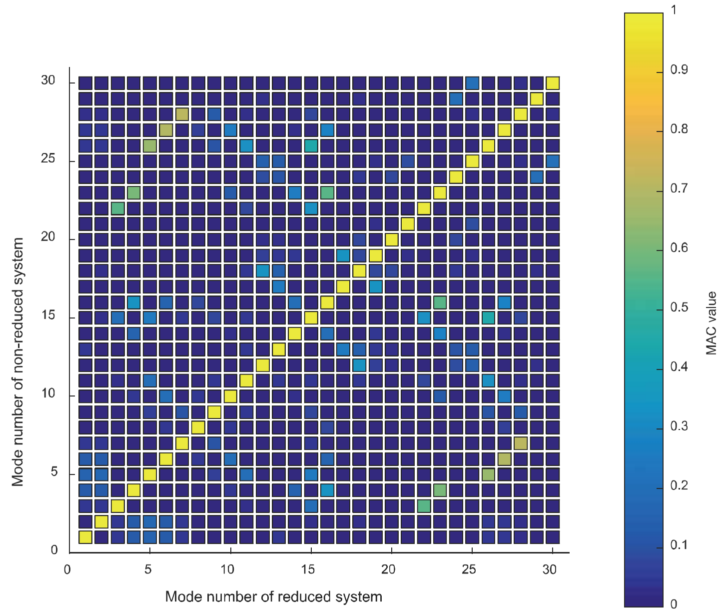

Figure 3.20. MAC for reduced system in the cable-stayed bridge problem ($N_s = 6$): (a) DCB method, (b) Improved DCB method.

3.3 Negative eigenvalues in lower modes

In the previous section, we demonstrated that the accuracy of the DCB method was significantly improved. When the improved DCB method is used, it is expected that spurious modes will be avoided in lower modes, when the selected dominant modes in the substructure are insufficient. Spurious modes in the reduced model could cause instability in various dynamic analyses. There have been several attempts to prevent this [26-27].

In this section, we compare the improved DCB method with the original DCB method for the ability to avoid negative eigenvalues and the corresponding spurious modes in lower modes. The plate with a hole in Fig. 3.5 is considered again. Only one vibration mode is selected in each substructure ($N_d = 4$); thus, the reduction basis is not well established. The number of DOFs in both reduced systems (N_1) is 158. Note that the rigid body modes are not considered for investigating spurious modes.

The first 25 eigenvalues calculated are listed in Table 3.9, in which mode numbers are sorted by the magnitude of eigenvalues. Fig. 3.21 presents the relative eigenfrequency errors in the FE models reduced by the original and improved DCB methods, in which only eigenfrequencies corresponding to positive eigenvalues are plotted. The first negative eigenvalue obtained by the original DCB method is found at the 9th mode and, after that, 40 negative eigenvalues appear until the 57th mode. That is, many spurious modes are calculated in lower modes. Eigenvalues obtained are infinite from the 58th to 152th modes. However, when the improved DCB method is used, the first negative eigenvalue is found at the 51th modes and no infinite eigenvalue is calculated. That is, the appearance of negative eigenvalues is shifted to relatively higher frequency range. This is an advantageous feature of the improved DCB method.

Table 3.9. Eigenvalues calculated for the plate with a hole. Negative eigenvalues are underlined.

No.	Original DCB	Improved DCB
1	3.7518E+02	3.7517E+02
2	5.9356E+02	5.9306E+02
3	3.3397E+03	3.2415E+03
4	3.3609E+03	3.3549E+03
5	6.7871E+03	6.7483E+03
6	1.0588E+04	9.5708E+03
7	1.0631E+04	1.0252E+04
8	1.3618E+04	1.3502E+04
9	-1.8564E+04	2.1398E+04
10	-2.0246E+04	2.4833E+04
11	-2.3018E+04	3.7087E+04
12	2.7750E+04	3.8271E+04
13	-4.0962E+04	5.5247E+04
14	5.0359E+04	5.5684E+04
15	6.8518E+04	7.0494E+04
16	7.1921E+04	7.9612E+04
17	-7.3877E+04	8.0927E+04
18	-7.8759E+04	1.0925E+05
19	9.2383E+04	1.2573E+05
20	-1.0689E+05	1.2642E+05
21	-1.1249E+05	1.3012E+05
22	-1.4226E+05	1.8680E+05
23	-1.4899E+05	2.1227E+05
24	-1.5146E+05	2.3759E+05
25	-2.2205E+05	2.4295E+05

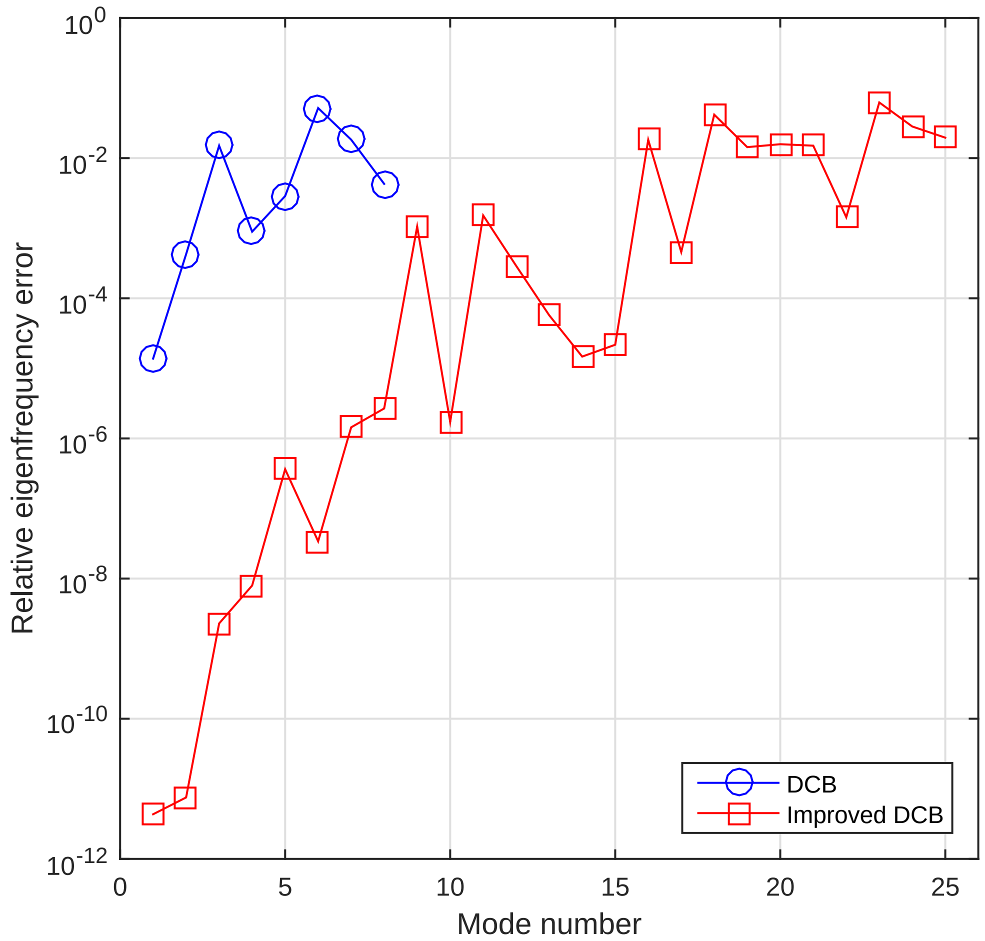

Figure 3.21. Relative eigenfrequency errors in the plate structure with a hole ($N_d = 4$).

Chapter 4. Error estimation method for DCB method

In structural engineering, the analyses of large and complex finite element (FE) models require a lot of time and computation cost, despite the development of computational hardware. Instead of directly handling the entire FE model, various studies have carried out to construct a reduced model to efficiently conduct the structural analyses. Among them, the component mode synthesis (CMS) methods [1-11, 26-44, 61] are widely used; these methods calculate the reduced model by considering only the dominant modes from partitioned substructures. In 1960s, Craig and Bampton (CB) [3] established the basic principles of CMS method after the pioneer work by Hurty [1]. Since then, various CMS methods have been presented such as automated multi-level substructuring (AMLS), dual CB (DCB), and F-CMS method [4-11].

The most important requirement of the reduced model is to have high reliability for the original FE model. However, since the eigenvalue analysis of the global FE model is not performed, it is difficult to measure the reliability of the reduced model. There have been attempts to solve this issue, but the previously proposed error estimation methods are only at the level of determining the tendency of relative eigenvalue error [12-15]. In this way, there is a difficulty in using the reduction method for practical use in engineering problems.

Recently, the accurate error estimation methods have been proposed for the representative CMS methods. Kim et al. proposed a method for accurately estimating the relative eigenvalue error for the CB method by computing an enhanced transformation matrix [45]. Boo et al. developed a simplified version of CB error estimation method and applied the same principle of error estimator to the AMLS method [46-47]. Kim et al. also developed the error estimation method for F-CMS method by approximating the residual flexibility matrix more precisely [48]. However, it is impossible to estimate the reliability of the reduced model by the DCB method [9].

The DCB method proposed by Rixen [9] has the same accuracy as the F-CMS method. The difference is that DCB method uses a classical Lagrange multiplier for interconnecting the neighboring substructures, unlike the F-CMS method, which uses a localized Lagrange multiplier. We have already proposed an improved DCB method by effectively considering the second order residual flexibility matrix [44]. The objective of this study is to adopt the same principle for accurately estimating the relative eigenvalue errors for the DCB method.

In the derivation procedure, the additional terms necessary for the present error estimation method can be efficiently computed by reusing the residual flexibility matrices of the DCB method. We propose the simplified calculation with the component matrices of each substructure. The accurately estimated errors are simply obtained by summation of the eigenvalue errors calculated for each substructure.

In the following sections, the detailed formulation of the error estimation method for DCB method is presented. Then, we investigate the performance of the error estimator using various numerical examples.

4.1 Formulation

In this section, we introduce the formulation to constructing the improved transformation matrix, which consider the second order residual flexibility. After that, we derive an error estimator for the DCB method.

4.1.1 Improved transformation matrix

From the Improved DCB method [44] in section 3, the substructural displacement can be rewritten as

$$\mathbf{u}^{(k)} = \mathbf{\Theta}_d^{(k)}\mathbf{q}_d^{(k)} - \mathbf{\Theta}_r^{(k)}(\mathbf{\Lambda}_r^{(k)} - \lambda\mathbf{I}_r^{(k)})^{-1}\mathbf{\Theta}_r^{(k)^T}\mathbf{B}^{(k)}\boldsymbol{\mu} + \mathbf{R}^{(k)}\boldsymbol{\alpha}^{(k)} \tag{4.1}$$

with $\mathbf{\Theta}_d^{(k)}\mathbf{q}_d^{(k)} = -\mathbf{\Theta}_d^{(k)}(\mathbf{\Lambda}_d^{(k)} - \lambda\mathbf{I}_d^{(k)})^{-1}\mathbf{\Theta}_d^{(k)^T}\mathbf{B}^{(k)}\boldsymbol{\mu}$.

Recalling Eq. (4.5), to construct the improved transformation matrix, we here consider the residual flexibility up to the second order term as

$$\mathbf{\Theta}_r^{(k)}(\mathbf{\Lambda}_r^{(k)} - \lambda^{(k)}\mathbf{I}_r^{(k)})^{-1}\mathbf{\Theta}_r^{(k)^T} \approx \mathbf{F}_1^{(k)} + \lambda^{(k)}\mathbf{F}_2^{(k)}. \tag{4.2}$$

Substituting Eq. (4.2) into Eq. (4.1), the approximated displacement of k^{th} substructure is newly defined as

$$\mathbf{u}^{(k)} \approx \mathbf{\Theta}_d^{(k)}\mathbf{q}_d^{(k)} - \mathbf{F}_1^{(k)}\mathbf{B}^{(k)}\boldsymbol{\mu} - \lambda^{(k)}\mathbf{F}_2^{(k)}\mathbf{B}^{(k)}\boldsymbol{\mu} + \mathbf{R}^{(k)}\boldsymbol{\alpha}^{(k)} \quad \text{with} \quad \mathbf{F}_2^{(k)} = \mathbf{\Theta}_r^{(k)}\mathbf{\Lambda}_r^{(k)^{-2}}\mathbf{\Theta}_r^{(k)^T}, \tag{4.3}$$

in which $\mathbf{F}_2^{(k)}$ is the second order residual flexibility matrix of the k^{th} substructure. Since $\mathbf{\Theta}_r^{(k)}$ has orthogonality for the substructural mass and stiffness matrices ($\mathbf{M}^{(k)}$ and $\mathbf{K}^{(k)}$), $\mathbf{F}_2^{(k)}$ can be easily calculated by reusing $\mathbf{F}_1^{(k)}$ in Eq. (2.23)

$$\mathbf{F}_2^{(k)} = \mathbf{F}_1^{(k)}\mathbf{M}^{(k)}\mathbf{F}_1^{(k)}. \tag{4.4}$$

The improved substructural transformation matrix $\widetilde{\mathbf{T}}^{(k)}$ is obtained as

$$\begin{bmatrix} \mathbf{u}^{(k)} \\ \boldsymbol{\mu} \end{bmatrix} \approx \tilde{\mathbf{T}}^{(k)} \begin{bmatrix} \boldsymbol{\alpha}^{(k)} \\ \mathbf{q}_d^{(k)} \\ \hline \boldsymbol{\mu} \end{bmatrix} \quad \text{with} \quad \tilde{\mathbf{T}}^{(k)} = \mathbf{T}^{(k)} + \lambda^{(k)} \mathbf{T}_a^{(k)}, \tag{4.5}$$

in which $\mathbf{T}_a^{(k)}$ is the additional substructural transformation matrix with the second order residual flexibility matrix

$$\mathbf{T}_a^{(k)} = \left[\begin{array}{cc|c} \mathbf{0} & \mathbf{0} & -\mathbf{F}_2^{(k)}\mathbf{B}^{(k)} \\ \mathbf{0} & \mathbf{0} & \mathbf{0} \end{array}\right]. \tag{4.6}$$

Using the substructural transformation matrices in Eq. (2.24) and Eq. (4.6), the global transformation matrix with improved approximation is given by

$$\tilde{\mathbf{T}} = \mathbf{T} + \lambda \mathbf{T}_a \tag{4.7}$$

with $\mathbf{T} = \left[\begin{array}{cc|c} \mathbf{R} & \boldsymbol{\Theta}_d & \boldsymbol{\Psi}_1 \\ \mathbf{0} & \mathbf{0} & \mathbf{I} \end{array}\right]$, $\mathbf{T}_a = \left[\begin{array}{cc|c} \mathbf{0} & \mathbf{0} & \boldsymbol{\Psi}_2 \\ \mathbf{0} & \mathbf{0} & \mathbf{0} \end{array}\right]$, $\boldsymbol{\Psi}_1 = \begin{bmatrix} -\mathbf{F}_1^{(1)}\mathbf{B}^{(1)} \\ \vdots \\ -\mathbf{F}_1^{(N_s)}\mathbf{B}^{(N_s)} \end{bmatrix}$, $\boldsymbol{\Psi}_2 = \begin{bmatrix} -\mathbf{F}_2^{(1)}\mathbf{B}^{(1)} \\ \vdots \\ -\mathbf{F}_2^{(N_s)}\mathbf{B}^{(N_s)} \end{bmatrix}$,

where $\mathbf{R}$ and $\boldsymbol{\Theta}_d$ are the block-diagonal rigid body mode and dominant free interface mode matrices that consist of substructural quantities ($\mathbf{R}^{(k)}$ and $\boldsymbol{\Theta}_d^{(k)}$), respectively. Note that the improved transformation matrix contains the transformation matrix of the original DCB method and the additional transformation matrix considering the second order residual flexibility.

4.1.2 Error estimator for the DCB method

The following relative eigenvalue error is commonly used to measure the reliability of the reduced model

$$\xi_i = \frac{\bar{\lambda}_i - \lambda_i}{\lambda_i} = \frac{\bar{\lambda}_i}{\lambda_i} - 1 , \tag{4.8}$$

where ξ_i is the i^{th} relative eigenvalue error, λ_i and $\bar{\lambda}_i$ are the i^{th} exact and approximated eigenvalue calculated from the eigenvalue problems in Eq. (2.13) and (2.27), respectively.

From Eq. (2.13), the global eigenvalue problem can be rewritten as

$$\frac{1}{\lambda_i}(\boldsymbol{\varphi}_g)_i^T \mathbf{K}_g (\boldsymbol{\varphi}_g)_i = (\boldsymbol{\varphi}_g)_i^T \mathbf{M}_g (\boldsymbol{\varphi}_g)_i , \tag{4.9}$$

in which the global eigenvector $(\boldsymbol{\varphi}_g)_i$ can be approximated by the improved transformation matrix $\widetilde{\mathbf{T}}$

$$(\boldsymbol{\varphi}_g)_i \approx \widetilde{\mathbf{T}}\bar{\boldsymbol{\varphi}}_i = (\mathbf{T} + \lambda_i \mathbf{T}_a)\bar{\boldsymbol{\varphi}}_i . \tag{4.10}$$

Substituting Eq. (4.10) into (4.9), to obtain

$$\frac{1}{\lambda_i}\bar{\boldsymbol{\varphi}}_i^T [\mathbf{T} + \lambda_i \mathbf{T}_a]^T \mathbf{K}_g [\mathbf{T} + \lambda_i \mathbf{T}_a]\bar{\boldsymbol{\varphi}}_i \approx \bar{\boldsymbol{\varphi}}_i^T [\mathbf{T} + \lambda_i \mathbf{T}_a]^T \mathbf{M}_g [\mathbf{T} + \lambda_i \mathbf{T}_a]\bar{\boldsymbol{\varphi}}_i \tag{4.11}$$

From the transformation in the DCB method, $(\bar{\boldsymbol{\varphi}})_i$ has the orthogonality for the reduced mass and stiffness matrices

$$\bar{\boldsymbol{\varphi}}_i^T \bar{\mathbf{K}} \bar{\boldsymbol{\varphi}}_i = \bar{\lambda}_i , \quad \bar{\boldsymbol{\varphi}}_i^T \bar{\mathbf{M}} \bar{\boldsymbol{\varphi}}_i = 1 , \tag{4.12}$$

and then, derivation of Eq. (4.11) results the following equation

$$\frac{\bar{\lambda}_i}{\lambda_i} - 1 \approx \bar{\boldsymbol{\varphi}}_i^T [\lambda_i \mathbf{T}^T \mathbf{M}_g \mathbf{T}_a + \lambda_i \mathbf{T}_a^T \mathbf{M}_g \mathbf{T} + \lambda_i^2 \mathbf{T}_a^T \mathbf{M}_g \mathbf{T}_a - \mathbf{T}^T \mathbf{K}_g \mathbf{T}_a - \mathbf{T}_a^T \mathbf{K}_g \mathbf{T} - \lambda_i \mathbf{T}_a^T \mathbf{K}_g \mathbf{T}_a]\bar{\boldsymbol{\varphi}}_i . \tag{4.13}$$

Since the symmetry of mass and stiffness matrices, the identical terms on the right side is expressed as

$$\frac{\bar{\lambda}_i}{\lambda_i} - 1 \approx \bar{\boldsymbol{\varphi}}_i^T [2\lambda_i \mathbf{T}^T \mathbf{M}_g \mathbf{T}_a - 2\mathbf{T}^T \mathbf{K}_g \mathbf{T}_a + \lambda_i^2 \mathbf{T}_a^T \mathbf{M}_g \mathbf{T}_a - \lambda_i \mathbf{T}_a^T \mathbf{K}_g \mathbf{T}_a] \bar{\boldsymbol{\varphi}}_i, \tag{4.14}$$

where the relative eigenvalue error on the left side is approximated by using $\bar{\lambda}_i$ instead of unknown λ_i on the right side

$$\frac{\bar{\lambda}_i}{\lambda_i} - 1 \approx \eta_i \quad \text{with} \quad \eta_i = \bar{\boldsymbol{\varphi}}_i^T [2\bar{\lambda}_i \mathbf{T}^T \mathbf{M}_g \mathbf{T}_a - 2\mathbf{T}^T \mathbf{K}_g \mathbf{T}_a + \bar{\lambda}_i^2 \mathbf{T}_a^T \mathbf{M}_g \mathbf{T}_a - \bar{\lambda}_i \mathbf{T}_a^T \mathbf{K}_g \mathbf{T}_a] \bar{\boldsymbol{\varphi}}_i, \tag{4.15}$$

in which η_i is the error estimator for the i^{th} approximated eigenvalue in the DCB method [9].

Using Eq. (4.7), each term to calculate the error estimator in Eq. (4.15) can be represented as

$$\mathbf{T}^T \mathbf{M}_g \mathbf{T}_a = \left[\begin{array}{cc:c} \mathbf{0} & \mathbf{0} & \mathbf{0} \\ \mathbf{0} & \mathbf{0} & \mathbf{0} \\ \hdashline \mathbf{0} & \mathbf{0} & \boldsymbol{\Psi}_1^T \mathbf{M} \boldsymbol{\Psi}_2 \end{array}\right], \quad \mathbf{T}^T \mathbf{K}_g \mathbf{T}_a = \mathbf{0}, \tag{4.16a}$$

$$\mathbf{T}_a^T \mathbf{M}_g \mathbf{T}_a = \left[\begin{array}{cc:c} \mathbf{0} & \mathbf{0} & \mathbf{0} \\ \mathbf{0} & \mathbf{0} & \mathbf{0} \\ \hdashline \mathbf{0} & \mathbf{0} & \boldsymbol{\Psi}_2^T \mathbf{M} \boldsymbol{\Psi}_2 \end{array}\right], \quad \mathbf{T}_a^T \mathbf{K}_g \mathbf{T}_a = \left[\begin{array}{cc:c} \mathbf{0} & \mathbf{0} & \mathbf{0} \\ \mathbf{0} & \mathbf{0} & \mathbf{0} \\ \hdashline \mathbf{0} & \mathbf{0} & \boldsymbol{\Psi}_2^T \mathbf{K} \boldsymbol{\Psi}_2 \end{array}\right]. \tag{4.16b}$$

It is important to note that all terms in Eq. (4.16) have only diagonal component matrices corresponding to the Lagrange multipliers.

The component matrices in Eq. (4.16) are obtained by the calculation of the substructural quantities as

$$\boldsymbol{\Psi}_1^T \mathbf{M} \boldsymbol{\Psi}_2 = \sum_{k=1}^{N_s} \mathbf{B}^{(k)^T} \mathbf{F}_1^{(k)} \mathbf{M}^{(k)} \mathbf{F}_2^{(k)} \mathbf{B}^{(k)}, \tag{4.17a}$$

$$\boldsymbol{\Psi}_2^T \mathbf{M} \boldsymbol{\Psi}_2 = \sum_{k=1}^{N_s} \mathbf{B}^{(k)^T} \mathbf{F}_2^{(k)} \mathbf{M}^{(k)} \mathbf{F}_2^{(k)} \mathbf{B}^{(k)}, \tag{4.17b}$$

$$\boldsymbol{\Psi}_2^T \mathbf{K} \boldsymbol{\Psi}_2 = \sum_{k=1}^{N_s} \mathbf{B}^{(k)^T} \mathbf{F}_2^{(k)} \mathbf{K}^{(k)} \mathbf{F}_2^{(k)} \mathbf{B}^{(k)}. \tag{4.17c}$$

Through the Eq. (4.17), the global matrix multiplications are efficiently replaced by reusing the substructural matrices.

Due to orthogonality, multiplications of residual flexibility matrices with $\mathbf{M}^{(k)}$ and $\mathbf{K}^{(k)}$ can be expressed by using the higher order residual flexibility matrices

$$\mathbf{\Psi}_1^T\mathbf{M}\mathbf{\Psi}_2 = \mathbf{\Psi}_2^T\mathbf{K}\mathbf{\Psi}_2 = \sum_{k=1}^{N_s}\mathbf{B}^{(k)^T}\mathbf{F}_3^{(k)}\mathbf{B}^{(k)}, \tag{4.18a}$$

$$\mathbf{\Psi}_2^T\mathbf{M}\mathbf{\Psi}_2 = \sum_{k=1}^{N_s}\mathbf{B}^{(k)^T}\mathbf{F}_4^{(k)}\mathbf{B}^{(k)}. \tag{4.18b}$$

From the relation in Eq. (4.18a), the term $\mathbf{T}^T\mathbf{M}_g\mathbf{T}_a$ is equal to $\mathbf{T}_a^T\mathbf{K}_g\mathbf{T}_a$, then Eq. (4.15) becomes

$$\eta_i = \overline{\boldsymbol{\varphi}}_i^T[\overline{\lambda}_i\mathbf{T}^T\mathbf{M}_g\mathbf{T}_a + \overline{\lambda}_i^2\mathbf{T}_a^T\mathbf{M}_g\mathbf{T}_a]\overline{\boldsymbol{\varphi}}_i. \tag{4.19}$$

The approximated eigenvector $\overline{\boldsymbol{\varphi}}_i$ in Eq. (4.19) can be decomposed by the substructural and the Lagrange multiplier parts

$$\overline{\boldsymbol{\varphi}}_i = \begin{bmatrix}\overline{\boldsymbol{\varphi}}_s \\ \overline{\boldsymbol{\varphi}}_\mu\end{bmatrix}_i, \tag{4.20}$$

Finally, substituting Eqs. (4.16), (4.18) and (4.20) into Eq. (4.19), the error estimator for the i^{th} approximated eigenvalue is redefined by a summation of the independently estimated errors in each substructure

$$\eta_i = \sum_{k=1}^{N_s}\eta_i^{(k)} \quad \text{with} \tag{4.21}$$

$$\eta_i^{(k)} = \overline{\lambda}_i(\overline{\boldsymbol{\varphi}}_\mu)_i^T\mathbf{B}^{(k)^T}\mathbf{F}_3^{(k)}\mathbf{B}^{(k)}(\overline{\boldsymbol{\varphi}}_\mu)_i + \overline{\lambda}_i^2(\overline{\boldsymbol{\varphi}}_\mu)_i^T\mathbf{B}^{(k)^T}\mathbf{F}_4^{(k)}\mathbf{B}^{(k)}(\overline{\boldsymbol{\varphi}}_\mu)_i.$$

The type of Eq. (4.21) has been attempted to measure the contribution of each substructure to the accuracy of the model reduction methods and to control the eigenvalue error [45].

In the following sections, the performance of the error estimator is investigated using various numerical examples.

4.2 Numerical examples

In this section, we investigate the performance of the error estimator for the DCB method. We considered four structural problems: a rectangular plate with matching and non-matching meshes, a hyperboloid shell, a pipe intersection, and a cable-stayed bridge.

For the finite element modeling, the 4-node MITC shell [65-70], 3D solid, and truss elements are used and free or fixed boundary conditions are imposed differently according to the problem. The frequency cut-off method is employed to select dominant substructural modes [21-23]. All the computer codes are implemented in MATLAB and computation is performed in a personal computer (Inter core (TM) i7-4770, 3.40 GHz CPU, 32 GB RAM).

We compare the present error estimator with a previous error estimator proposed by Elssel and Voss [13].

$$\hat{\eta}_i = \frac{\bar{\lambda}_i}{\left|\lambda_r - \bar{\lambda}_i\right|}, \tag{4.22}$$

in which λ_r is the smallest substructural eigenvalue in the residual parts. This error estimator was proposed for the CB [3] and Automated multi-level substructuring (AMLS) method [11] as an upper bound of the relative eigenvalue error, it also could evaluate the eigenvalue errors in the DCB method

$$0 \le \xi_i \le \hat{\eta}_i . \tag{4.23}$$

Through numerical examples, we attempted to correct the eigenvalues approximated by the DCB method [9] using the estimated error

$$\lambda_i' = \frac{\bar{\lambda}_i}{\eta_i + 1}, \tag{4.24}$$

where λ_i' is the corrected eigenvalue of the present method.

4.2.1 Rectangular plate problem

Let us consider a rectangular plate with free boundary, see Fig. 4.1. Length L is 0.6096 m, width B is 0.3048 m, and thickness h is 3.18×10^{-3} m. Young's modulus E is 72 GPa, Poisson's ratio ν is 0.33, and density ρ is 2796 $\mathrm{kg/m^3}$. The whole structure is an assemblage of two substructures ($N_s = 2$) modeled by 4-node MITC shell elements. We consider two numerical cases, with matching and non-matching meshes between neighboring substructures. For the both cases, the numbers of dominant modes used and the numbers of DOFs in original and reduced systems are listed in Table 4.1.

We firstly consider the matching mesh case as shown in Fig. 4.1a. Fig. 4.2 presents the exact and estimated relative eigenvalue errors, respectively. The results show that the present error estimator can estimate the relative eigenvalue errors very accurately. Using the estimated errors, the corrected eigenvalues are obtained by Eq. (4.24), Fig. 4.3 presents the more accurately approximated eigenvalues.

For the non-matching mesh case as shown in Fig. 4.1b, the second substructure is modeled by an 8×12 mesh. In this case, the interface compatibility is considered through nodal collocation and thus the matrices $\mathbf{B}^{(i)}$ are no longer Boolean, see Fig. 4.1c. Fig. 4.4 presents the exact and estimated relative eigenvalue errors, and Fig. 4.5 presents the improved accuracy of the corrected eigenvalues by using the present error estimator. The results also show that the excellent performance of the present method.

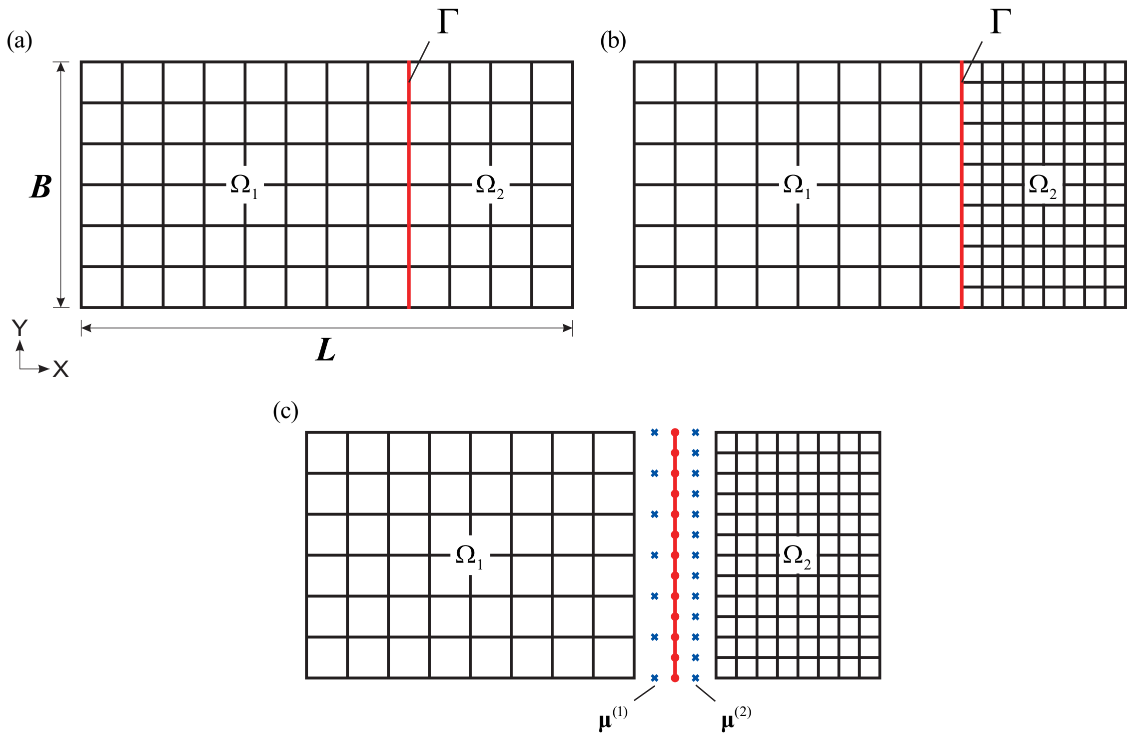

Figure 4.1 Rectangular plate problem: (a) Matching mesh on the interface (12×6 mesh), (b) Non-matching mesh between neighboring substructures, (c) Interface boundary treatment.

Table 4.1 Number of dominant modes used and number of DOFs in original and reduced systems for the rectangular plate problem.

Cases	$N_d^{(1)}$	$N_d^{(2)}$	N_d	N_g	N_1
Matching mesh	20	11	31	455	78
Non-matching mesh	14	8	22	965	99

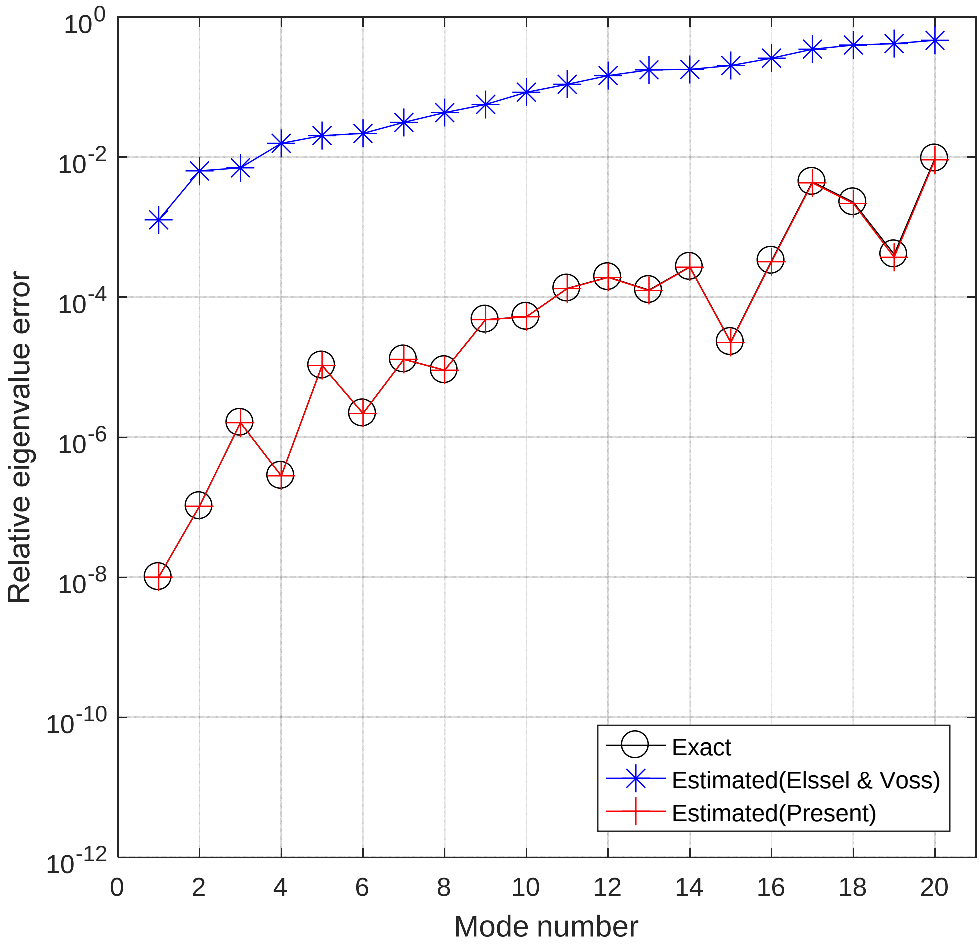

Figure 4.2. Exact and estimated relative eigenvalue errors in the rectangular plate problem with matching mesh.

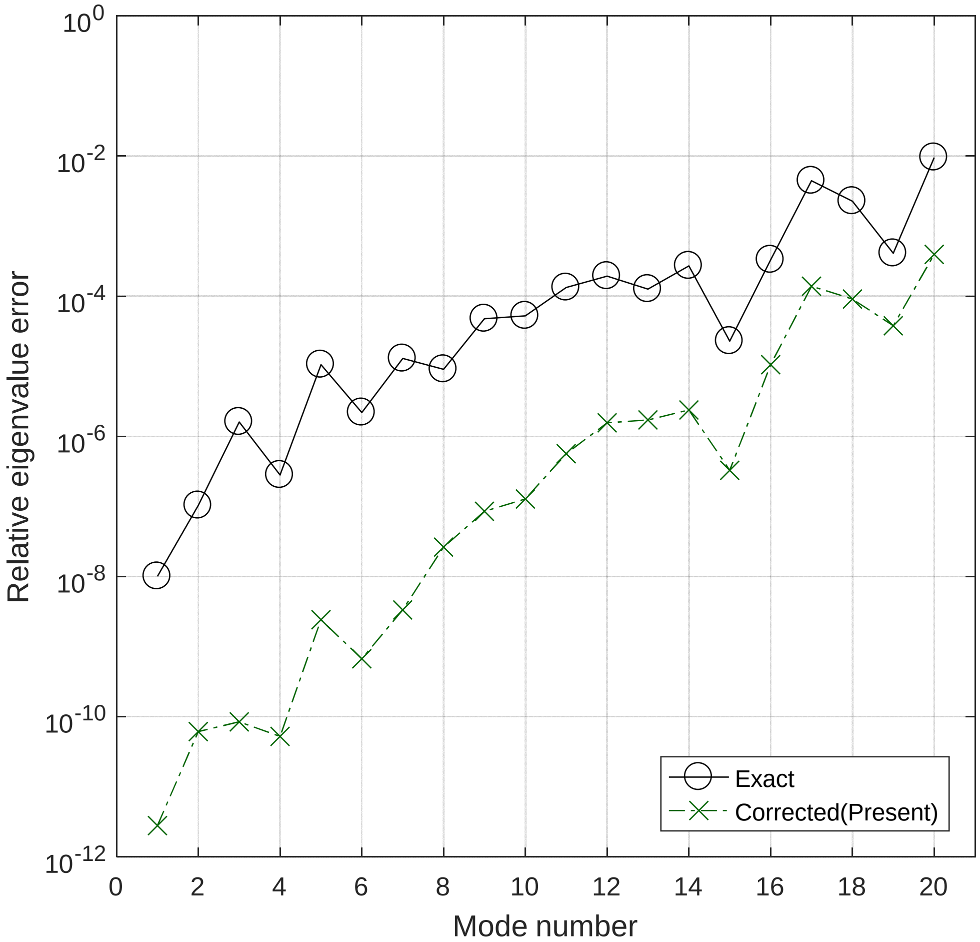

Figure 4.3. Relative errors for the corrected eigenvalues in the rectangular plate problem with matching mesh.

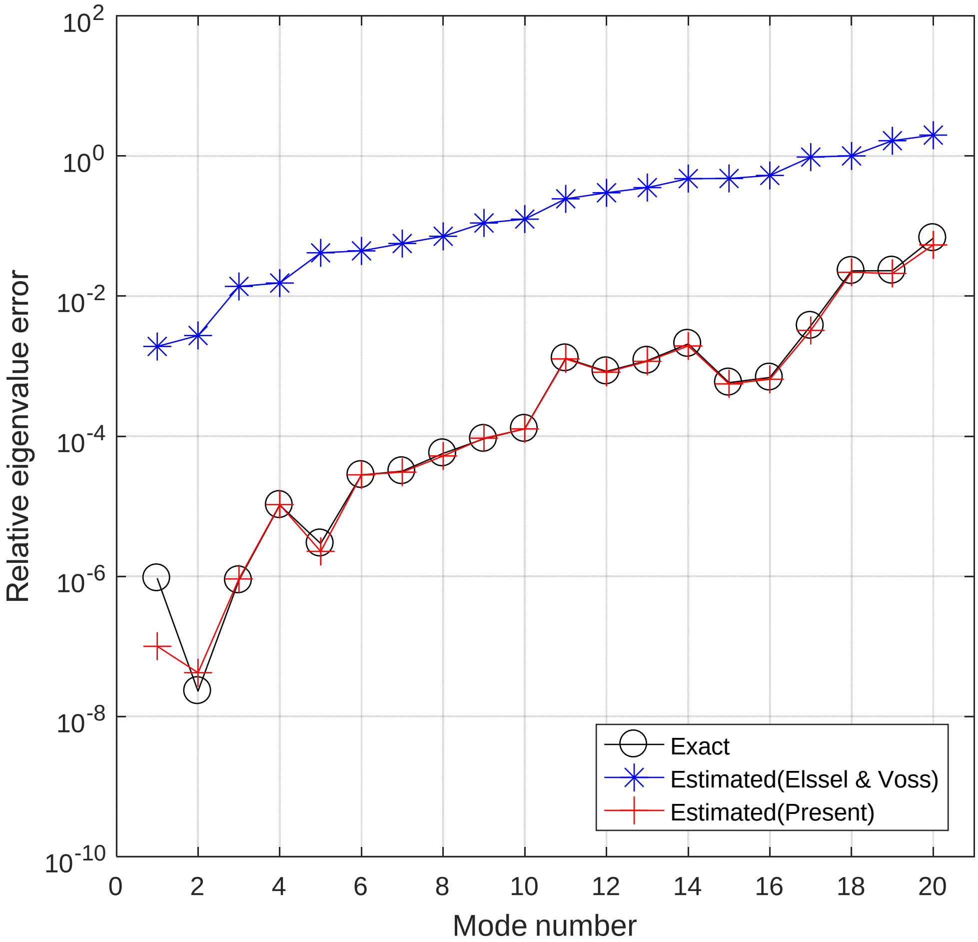

Figure 4.4. Exact and estimated relative eigenvalue errors in the rectangular plate problem with non-matching mesh.

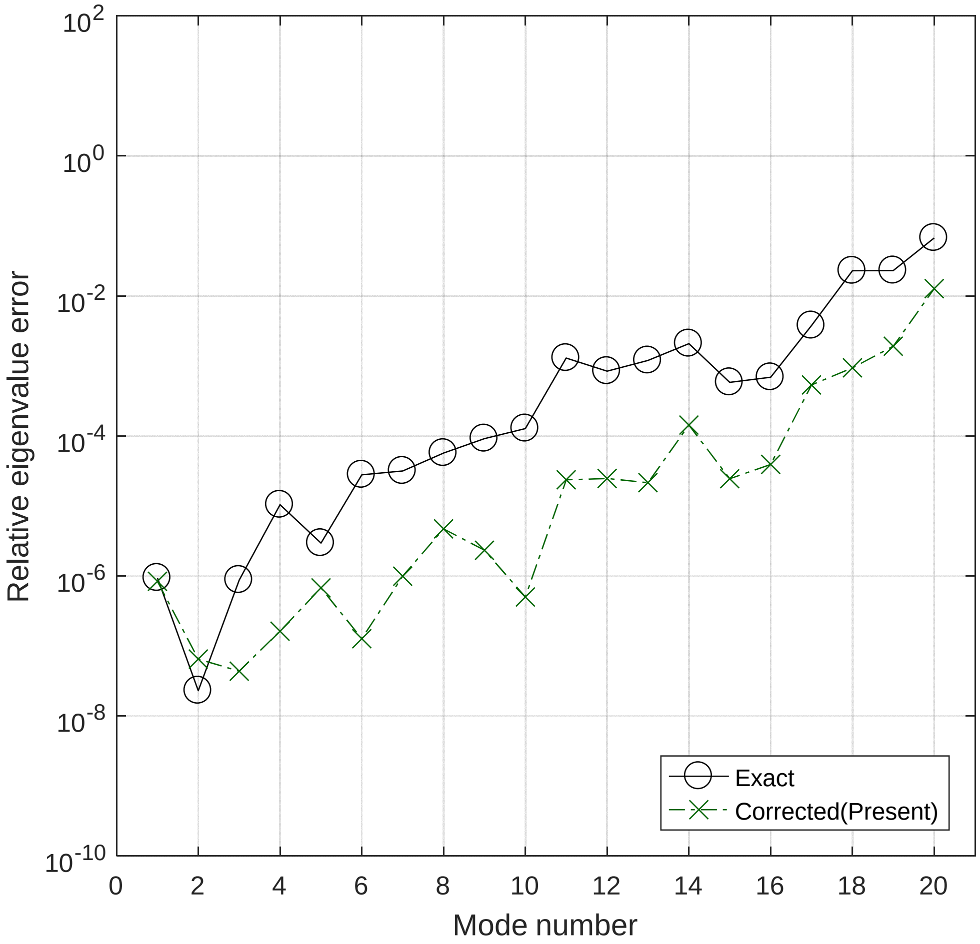

Figure 4.5. Relative errors for the corrected eigenvalues in the rectangular plate problem with non-matching mesh.

4.2.2 Hyperboloid shell problem

We here consider a hyperboloid shell structure with free boundary as shown in Fig. 4.6. Height H is 4.0 m and thickness h is 0.05 m. Young's modulus E is 69 GPa, Poisson's ratio ν is 0.35, and density ρ is 2700 $\mathrm{kg/m^3}$. The mid-surface of this shell structure is described by

$$x^2 + y^2 = 2 + z^2; \quad z \in [-2,2]. \tag{4.25}$$

Three substructures ($N_s = 3$) are assembled to construct the original FE model of the shell structures, in which 800 shell elements and 903 nodes are used (4200 DOFs). Table 4.2 lists the numbers of dominant modes used and the numbers of DOFs in the original and reduced systems.

Fig. 4.7 presents the exact and estimated relative eigenvalue errors, respectively. Compare to the previously proposed method [], the results demonstrate the solution accuracy of the present error estimation method. Through the Fig. 4.8, the corrected eigenvalues show the effect of further improving the reliability of the solutions by simple calculation.

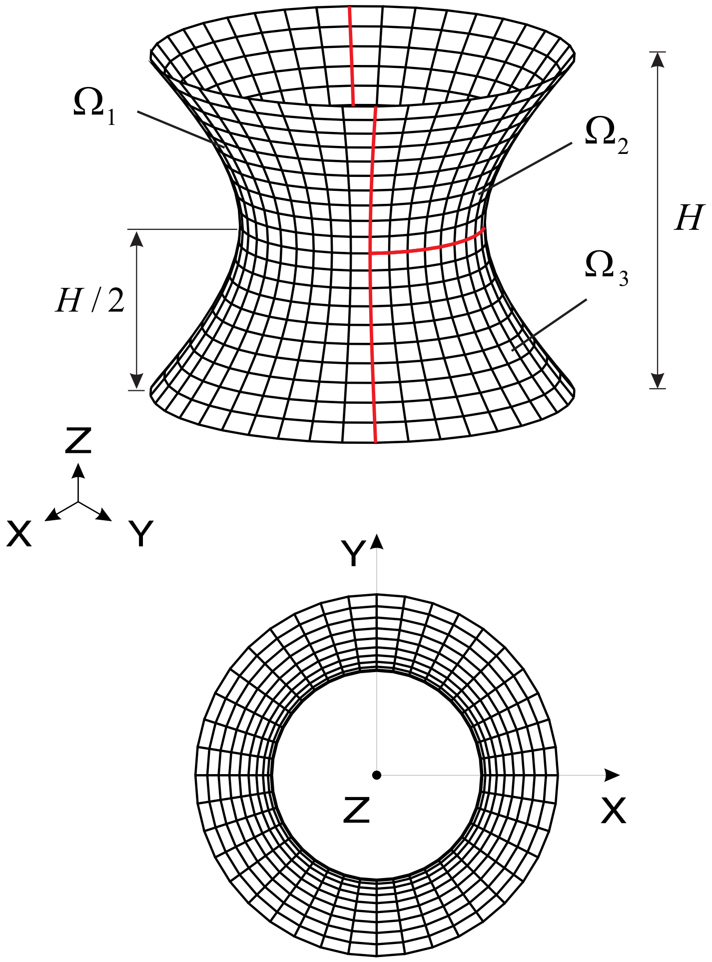

Figure 4.6. Hyperboloid shell problem.

Table 4.2. Number of dominant modes used and number of DOFs in original and reduced systems for the hyperboloid shell problem.

Methods	$N_d^{(1)}$	$N_d^{(2)}$	$N_d^{(3)}$	N_d	N_g	N_1
Present	26	14	14	54	4830	387

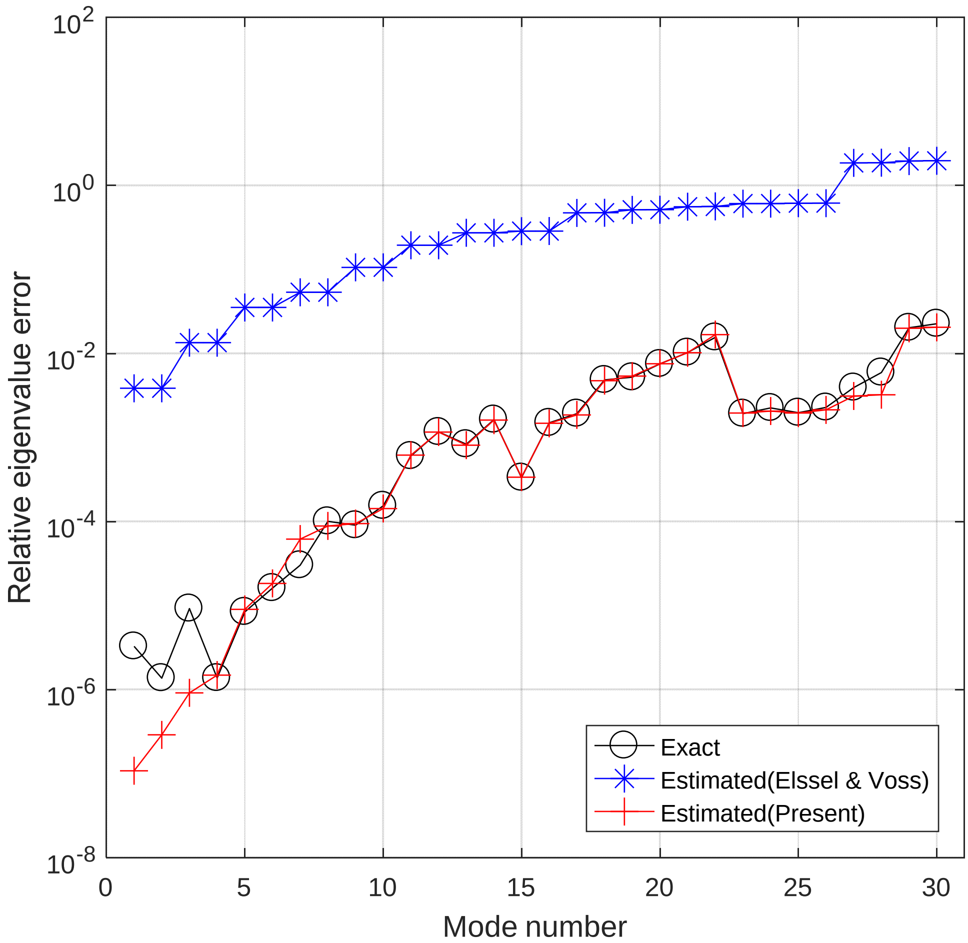

Figure 4.7. Exact and estimated relative eigenvalue errors in the hyperboloid shell problem.

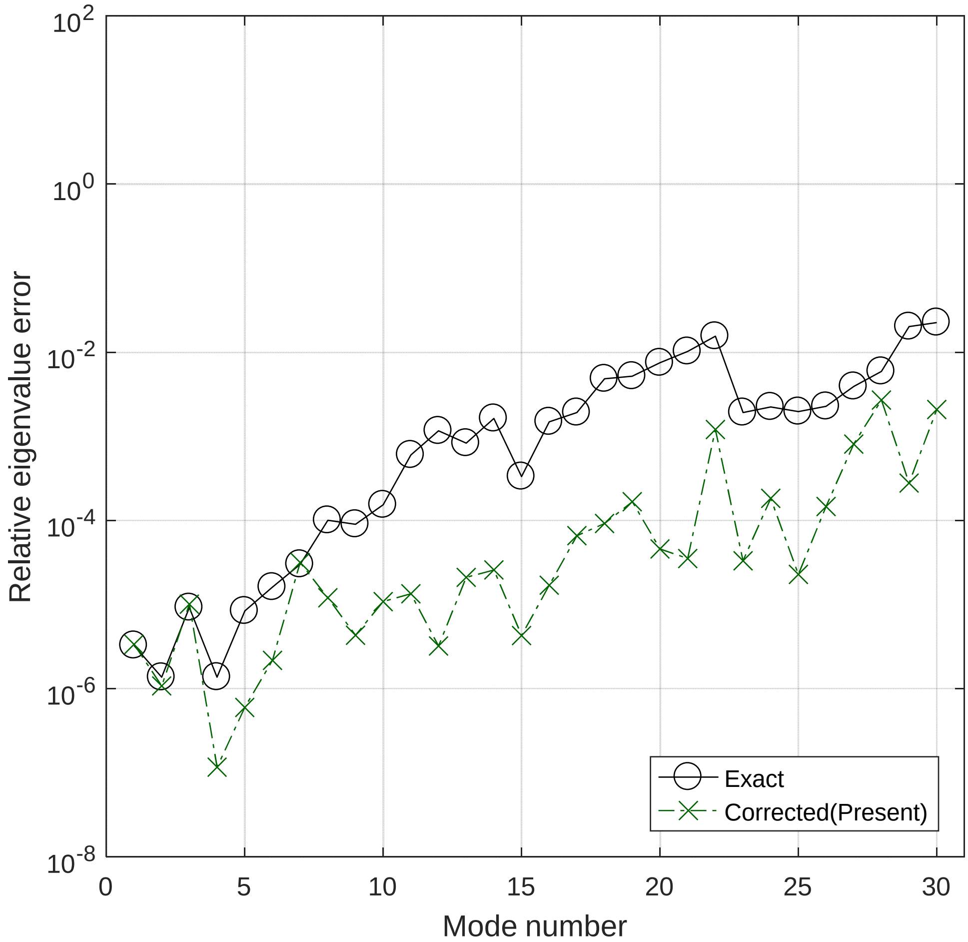

Figure 4.8. Relative errors for the corrected eigenvalues in the hyperboloid shell problem.

4.2.3 Pipe intersection problem

A pipe intersection structure with clamped boundary at one end is considered as shown in Fig. 4.9, in which the structural configuration and specification are illustrated. Young's modulus E is 69 GPa, Poisson's ratio ν is 0.35, and density ρ is 2700 $\mathrm{kg/m^3}$. The whole structure is an assemblage of two substructures ($N_s = 2$) modeled by 4-node MITC shell elements. The whole FE model has 948 shell elements and 976 nodes (5736 DOFs).

The number of DOFs in the non-reduced system (N_g) is 5952, the number of dominant modes retained in each substructure ($N_d^{(k)}$) are 51 and 38, respectively. Then, the reduced model by the DCB method has 203 DOFs.

Fig. 4.10 presents the exact and estimated relative eigenvalue errors, respectively. Although slightly over-estimations are made in some low-order modes, the corrected eigenvalues can solve these cases because it has an accuracy higher than the approximated eigenvalues by the DCB method. The accuracy of the corrected eigenvalues can be checked by Fig. 4.11.

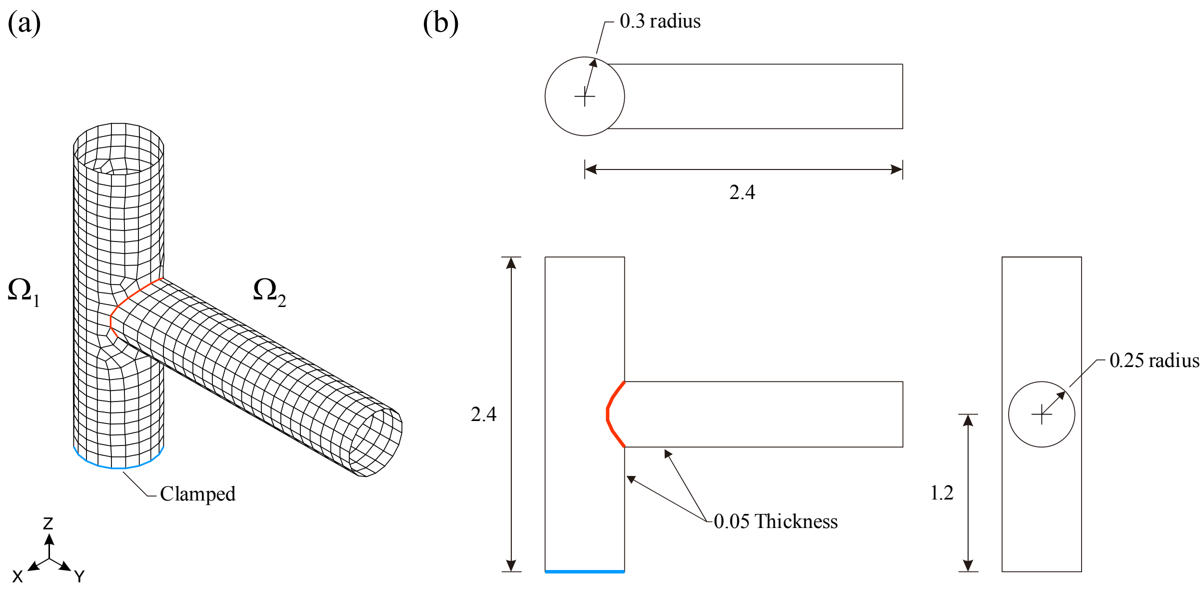

Figure 4.9. Pipe intersection problem.

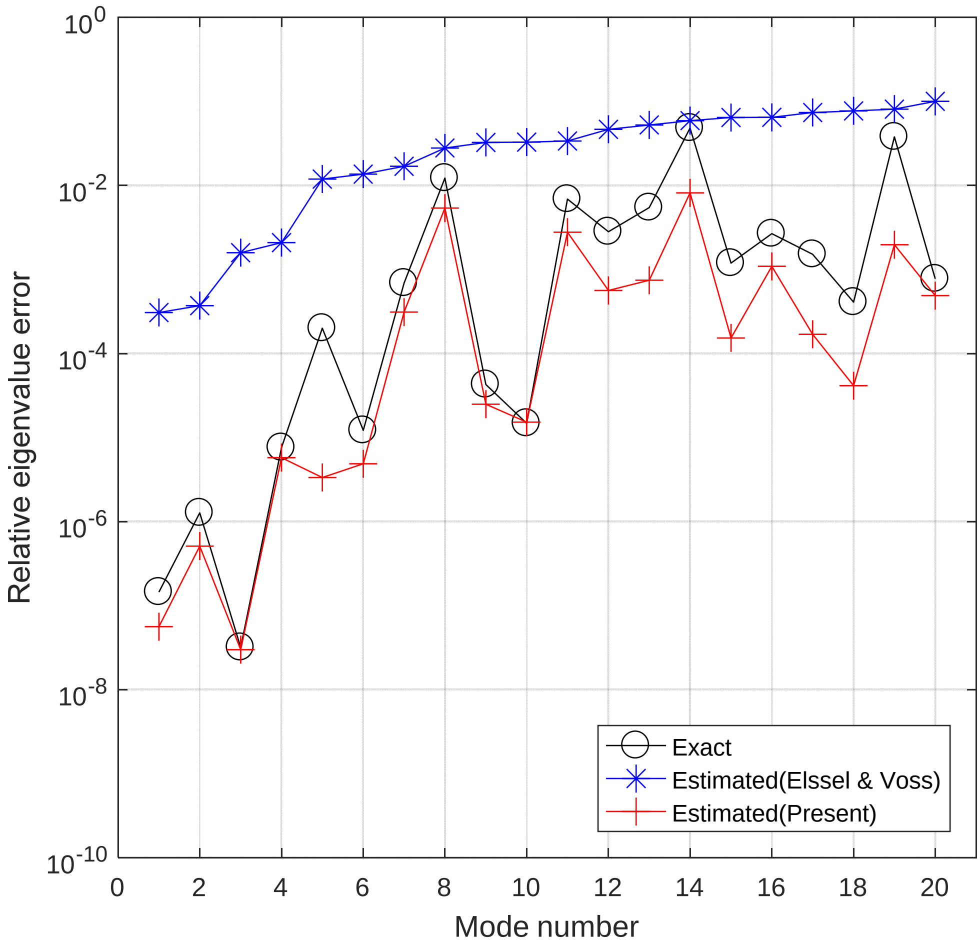

Figure 4.10. Exact and estimated relative eigenvalue errors in the Pipe intersection problem.

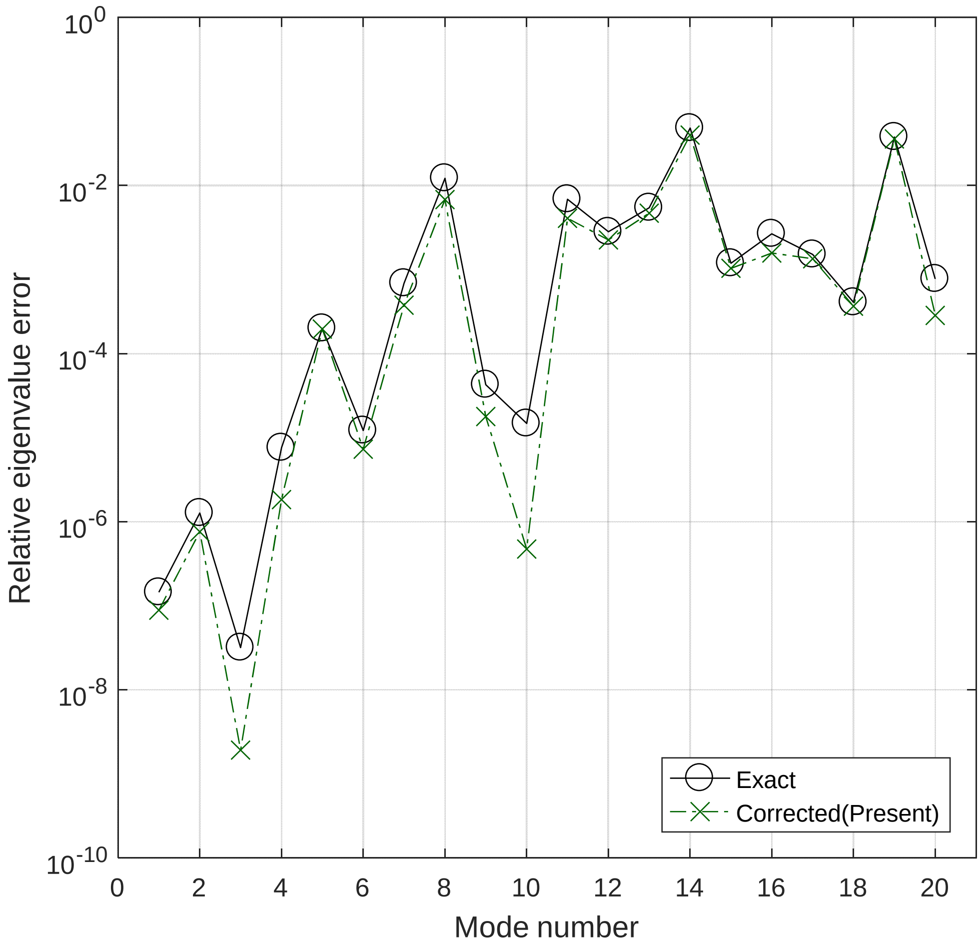

Figure 4.11. Relative errors for the corrected eigenvalues in the Pipe intersection problem.

4.2.4 Cable-stayed bridge problem

We finally consider a cable-stayed bridge problem as shown in Fig. 4.12 and 4.13. The unit of length in this figure is feet (ft). The FE model and its mass and stiffness matrices are obtained by the well-known commercial FE analysis software, ADINA [70]. The structure is modeled using 504 shell elements for the girder, 50 3D solid elements for the tower, and 4 3D truss elements for the cable, respectively. The number of nodes is 1666, and total DOFs is 6878.

Here, we considered the bridge structure in Fig. 4.12 as one sub-structure and connected multiple substructures to make the long-span bridge structure as in Fig. 4.13. In this problem, we assemble the six substructures ($N_s = 6$), Table 4.3 lists the numbers of dominant modes used and the numbers of DOFs in the original and reduced systems.

Fig. 4.14 presents the exact and estimated relative eigenvalue errors, respectively. The proposed error estimation method provides consistently accurate results. Fig. 4.15 present the relative errors for the corrected eigenvalues with improving the solution accuracy.

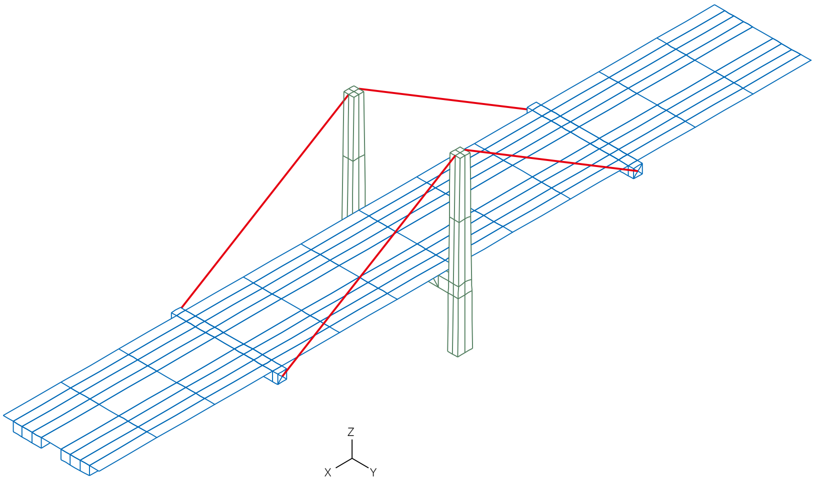

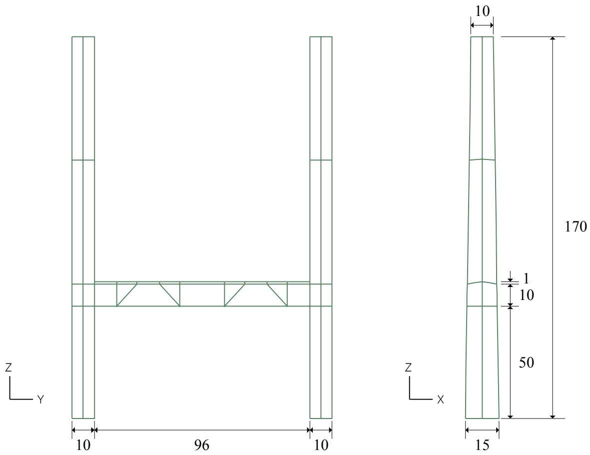

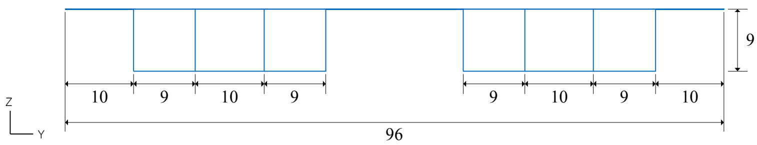

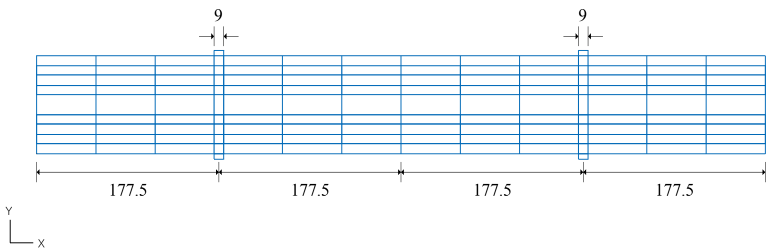

Figure 4.12. Cable-stayed bridge problem (1 substructure).

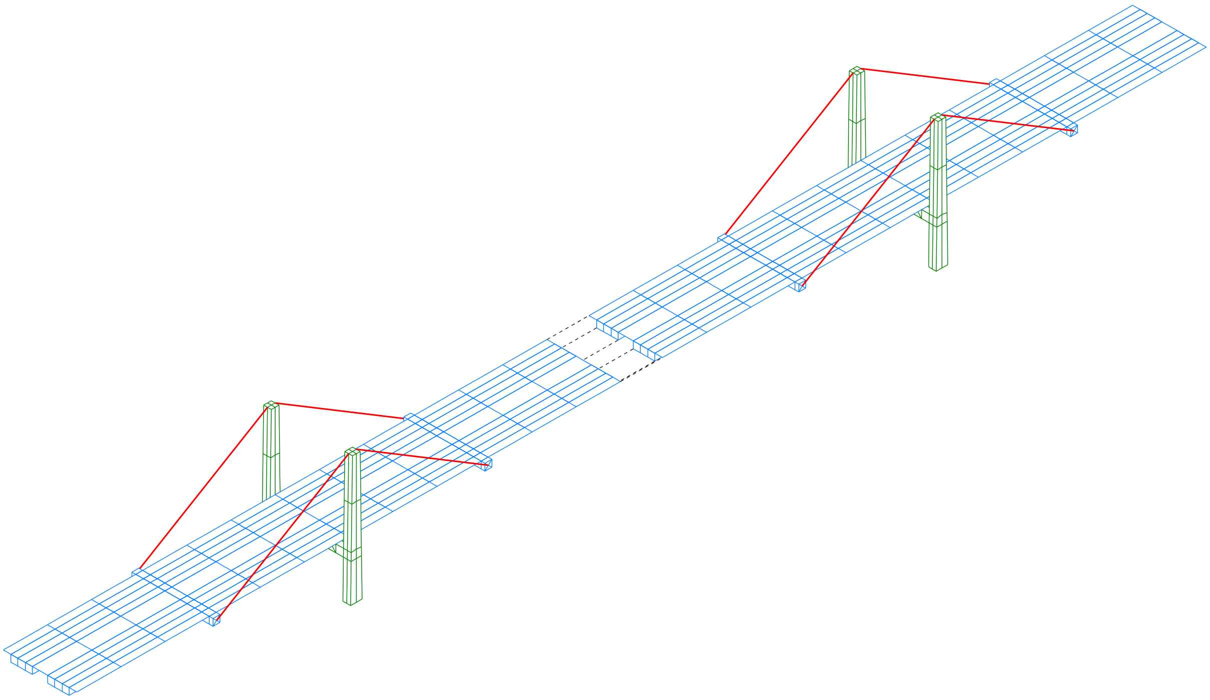

Figure 4.13. Connection of cable-stayed bridge substructures ($N_s = 2$).

Table 4.3. Number of dominant modes used and number of DOFs in original and reduced systems for the cable-stayed bridge problem ($N_s = 6$).

Method	$N_d^{(1)}$	$N_d^{(2)}$	$N_d^{(3)}$	$N_d^{(4)}$	$N_d^{(5)}$	$N_d^{(6)}$	N_g	N_1
Present	8	8	8	8	8	8	42293	1073

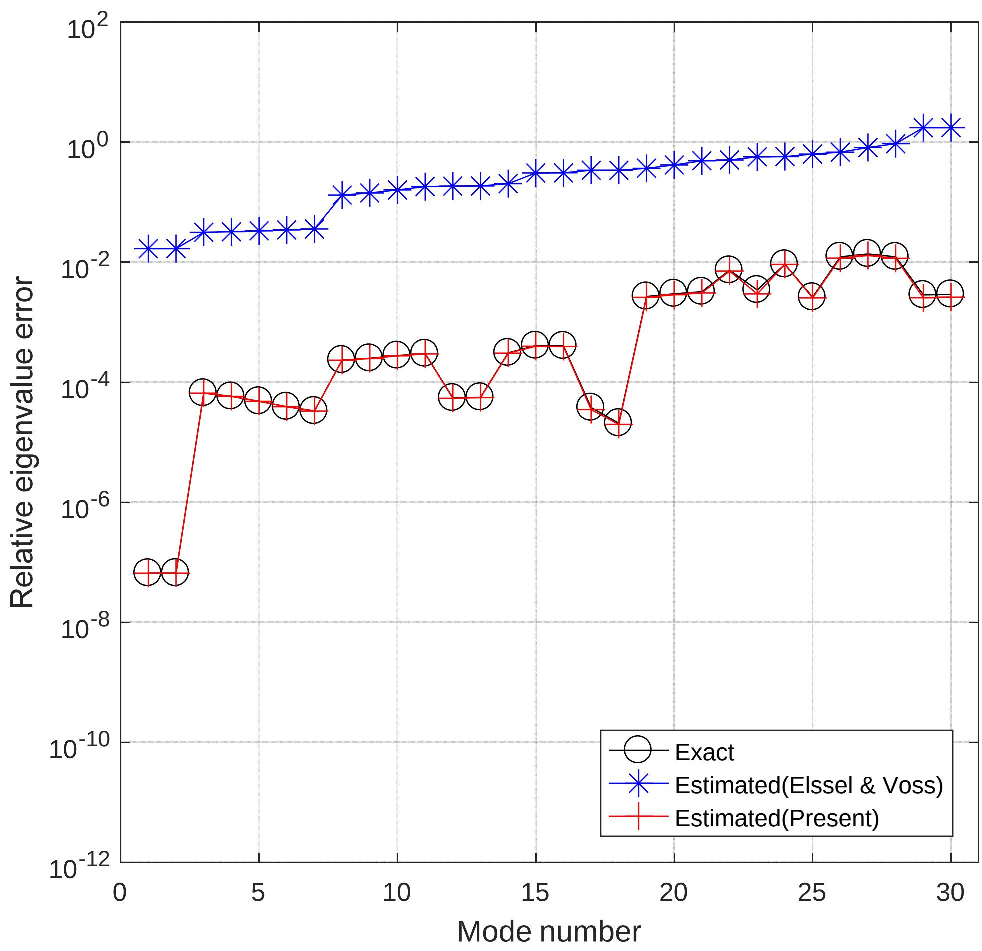

Figure 4.14. Exact and estimated relative eigenvalue errors in the cable-stayed bridge problem ($N_s = 6$).

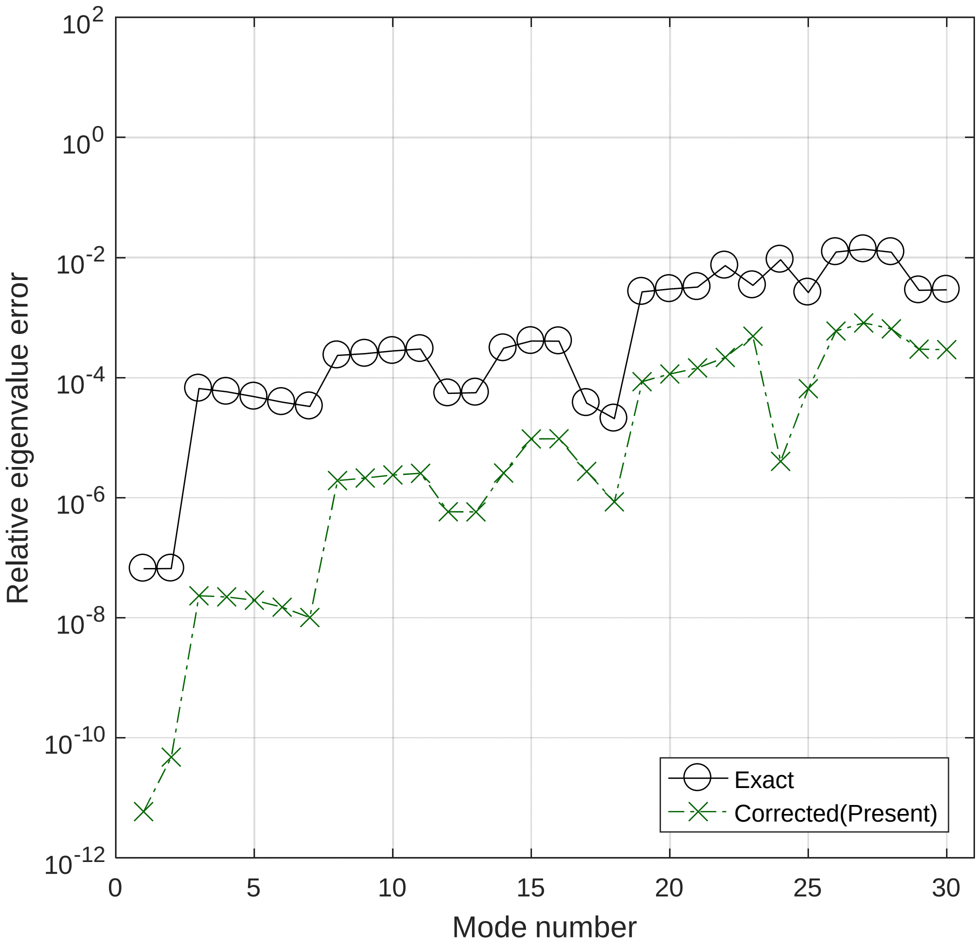

Figure 4.15. Relative errors for the corrected eigenvalues in the cable-stayed bridge problem ($N_s = 6$).

Chapter 5. A dynamic condensation method with free-interface based substructuring

With the development of design and manufacturing in engineering practice, structures have become huge and complex in shape. The large structures are partitioned with various substructures and individually constructed. It means that repeated design modifications including re-analyses and experiments are required in both local and global configurations. By these reasons, constructing FE model of the entire structure is very difficult because the time required to the design and analyses of the substructures are different. A number of model reduction methods have spotlighted its necessity to solve these difficulties, especially, in the structural dynamics community [1-11, 16-20, 26-58, 61-62].

The model reduction methods [1-37] can be classified into DOF based and mode based methods. In the 1960s, the pioneering works for both methods were proposed by Guyan [16] and Hurty [1], respectively. The mode based reduction methods (also called component mode synthesis, CMS) have been studied extensively for practical application [1-11, 26-39] because of the reduction procedure fundamentally including the substructuring. In contrast, the DOF based reduction methods have a lack of research in spite of their necessities. These included such as structural health monitoring, FE model updating, experimental modal analysis and experimental-FE model correlation [49-58].

In the DOF based reduction methods, a reduced model is calculated by classifying the master and slave DOFs in the FE model, then properly condensing the slave DOFs into the master DOFs. Since the Guyan reduction [16] uses only static condensation, it is difficult to obtain the required accuracy for dynamic analysis. O'Callahan [17] developed an IRS method considering inertial effects, and iterative IRS (IIRS) method was developed by Blair and Friswell et al [19-20]. Through the introduced methods, they focused on improving the accuracy, but it is difficult to obtain the reduced model within a reasonable computation time for the large-scale FE model.

Since the 1990s, several substructuring algorithms have been applied to the DOF based reduction method. Bouhaddi and Fillod applied substructuring to the Guyan reduction [49-50]. Cho et al. applied physical domain based substructuring to the IRS and IIRS methods and employed the penalty frame method for considering non-matched subdomains [51-54]. The applied substructuring algorithms were based on the primal assembly technique, which considers the interface between neighboring substructures as fixed. For primal assembly, the substructures are coupled through a unique set of physical interface DOFs. There have the simplicity and robustness, but it requires a fully assembled FE model in advance to obtain a reduced model.

In the dual assembly technique [9-10, 26-27, 44], the all substructures are defined as a free boundary when there are no physical constraint conditions. The most important feature of the dual assembly technique can ensure the substructural independence and easily treat the complicated physical boundary conditions and the non-matching mesh problems of assembling the numerical model [9-10, 44, 52-53]. This is also suitable to use the experimentally obtained substructural model. Because of these advantages, it is necessary to apply the substructuring with dual assembly technique to the model reduction methods. Recently, it has been successfully applied to the CMS methods [9-10, 26-27], and improved by our research group [44].

The motivation of this study is that the free-interface based substructuring can be adapted to the DOF based reduction. In this study, we focus on improving the efficiency of the IRS method. We introduce the algorithm for reducing each substructure independently by defining equations of motion and compatibility conditions in dual assembly form. Finally, the reduced mass and stiffness matrices are obtained by the simple assemblage of reduced substructural matrices. By using the present method, the local changes of substructure do not cause the entire update of reduced model. The present method is expected to be a powerful tool for experiments and structural health monitoring in local scale instead of global scale analyses.

The formulation of the present method is described in Section 5.1. The performance of the present method through various numerical examples in Section 5.2.

5.1 Formulation

In this section, we derive the formulation of the proposed method. The dual assembly technique is applied for substructuring, and each substructure is reduced independently by using its transformation matrix constructing with the IRS method [17]. Then, the reduced model is simply obtained by an assemblage of substructural matrices calculated.

The dynamic equilibrium equation of the assembled global FE model [9, 26, 44] in Eq. (2.12) is rewritten as

$$\begin{bmatrix} \mathbf{M} & \mathbf{0} \\ \mathbf{0} & \mathbf{0} \end{bmatrix} \begin{bmatrix} \ddot{\mathbf{U}} \\ \ddot{\boldsymbol{\gamma}} \end{bmatrix} + \begin{bmatrix} \mathbf{K} & \mathbf{B} \\ \mathbf{B}^T & \mathbf{0} \end{bmatrix} \begin{bmatrix} \mathbf{U} \\ \boldsymbol{\gamma} \end{bmatrix} = \begin{bmatrix} \mathbf{f} \\ \mathbf{0} \end{bmatrix}, \tag{5.1}$$

with $\mathbf{M} = \begin{bmatrix} \mathbf{M}^{(1)} & & \mathbf{0} \\ & \ddots & \\ \mathbf{0} & & \mathbf{M}^{(N_s)} \end{bmatrix}$, $\mathbf{K} = \begin{bmatrix} \mathbf{K}^{(1)} & & \mathbf{0} \\ & \ddots & \\ \mathbf{0} & & \mathbf{K}^{(N_s)} \end{bmatrix}$, $\mathbf{U} = \begin{bmatrix} \mathbf{U}^{(1)} \\ \vdots \\ \mathbf{U}^{(N_s)} \end{bmatrix}$, $\mathbf{f} = \begin{bmatrix} \mathbf{f}^{(1)} \\ \vdots \\ \mathbf{f}^{(N_s)} \end{bmatrix}$, $\mathbf{B} = \begin{bmatrix} \mathbf{B}^{(1)} \\ \vdots \\ \mathbf{B}^{(N_s)} \end{bmatrix}$,

where $\mathbf{M}$ and $\mathbf{K}$ are block-diagonal mass and stiffness matrices that consist of substructural mass and stiffness matrices ($\mathbf{M}^{(k)}$ and $\mathbf{K}^{(k)}$), $\mathbf{U}^{(k)}$ is the corresponding displacement vector, and $\mathbf{f}^{(k)}$ is the external load vector applied to the substructure. To satisfy the force equilibrium in the assembly, $\mathbf{B}^{(k)}\boldsymbol{\gamma}$ is applied as the interconnecting force between substructures with Boolean matrix $\mathbf{B}^{(k)} = \begin{bmatrix} \mathbf{0} \\ \mathbf{b}^{(k)} \end{bmatrix}$ and the Lagrange multiplier vector $\boldsymbol{\gamma}$.

Then, the global eigenpairs are obtained from the following eigenvalue problem

$$\mathbf{K}_g (\boldsymbol{\varphi}_g)_i = \lambda_i \mathbf{M}_g (\boldsymbol{\varphi}_g)_i \quad \text{for } i = 1, \cdots, N_g, \tag{5.2}$$

with $\mathbf{K}_g = \begin{bmatrix} \mathbf{K} & \mathbf{B} \\ \mathbf{B}^T & \mathbf{0} \end{bmatrix}$, $\mathbf{M}_g = \begin{bmatrix} \mathbf{M} & \mathbf{0} \\ \mathbf{0} & \mathbf{0} \end{bmatrix}$, in which $(\lambda_g)_i$ and $(\boldsymbol{\varphi}_g)_i$ are the global eigenvalue and corresponding eigenvector of the i^{th} global mode, respectively, and N_g is the number of DOFs in the assembled global FE model. This number consists of interface and substructural DOFs ($N_g = N_\mu + \sum_{k=1}^{N_s} N^{(k)}$, where N_μ is the number of Lagrange multipliers and $N^{(k)}$ is the number of DOFs of the k^{th} substructure).

In Eq. (5.1), the dynamic equilibrium equation corresponding to the k^{th} substructure can be extracted as

$$\begin{bmatrix} \mathbf{M}^{(k)} & \mathbf{0} \\ \mathbf{0} & \mathbf{0} \end{bmatrix} \begin{bmatrix} \ddot{\mathbf{U}}^{(k)} \\ \ddot{\boldsymbol{\gamma}} \end{bmatrix} + \begin{bmatrix} \mathbf{K}^{(k)} & \mathbf{B}^{(k)} \\ \mathbf{B}^{(k)T} & \mathbf{0} \end{bmatrix} \begin{bmatrix} \mathbf{U}^{(k)} \\ \boldsymbol{\gamma} \end{bmatrix} = \begin{bmatrix} \mathbf{f}^{(k)} \\ \mathbf{0} \end{bmatrix}, \quad k = 1, \cdots, N_s . \tag{5.3}$$

The eigenvalue problem of k^{th} substructure is given by

$$\begin{bmatrix} \mathbf{K}^{(k)} & \mathbf{B}^{(k)} \\ \mathbf{B}^{(k)T} & \mathbf{0} \end{bmatrix} \begin{bmatrix} \mathbf{u}^{(k)} \\ \boldsymbol{\mu} \end{bmatrix} = \lambda^{(k)} \begin{bmatrix} \mathbf{M}^{(k)} & \mathbf{0} \\ \mathbf{0} & \mathbf{0} \end{bmatrix} \begin{bmatrix} \mathbf{u}^{(k)} \\ \boldsymbol{\mu} \end{bmatrix}, \tag{5.4}$$

in which $\mathbf{u}^{(k)}$ and $\boldsymbol{\mu}$ are the eigenvectors corresponding to the substructural displacement vector $\mathbf{U}^{(k)}$ and the Lagrange multiplier vector $\boldsymbol{\gamma}$, respectively. $\lambda^{(k)}$ is the eigenvalue of the k^{th} substructure.

The substructural quantities ($\mathbf{M}^{(k)}$, $\mathbf{K}^{(k)}$, $\mathbf{B}^{(k)}$, and $\mathbf{u}^{(k)}$) are decomposed into master and slave parts as follows

$$\mathbf{M}^{(k)} = \begin{bmatrix} \mathbf{M}_{ss}^{(k)} & \mathbf{M}_{sm}^{(k)} \\ \mathbf{M}_{ms}^{(k)} & \mathbf{M}_{mm}^{(k)} \end{bmatrix}, \quad \mathbf{K}^{(k)} = \begin{bmatrix} \mathbf{K}_{ss}^{(k)} & \mathbf{K}_{sm}^{(k)} \\ \mathbf{K}_{ms}^{(k)} & \mathbf{K}_{mm}^{(k)} \end{bmatrix}, \quad \mathbf{B}^{(k)} = \begin{bmatrix} \mathbf{B}_{s}^{(k)} \\ \mathbf{B}_{m}^{(k)} \end{bmatrix}, \quad \mathbf{u}^{(k)} = \begin{bmatrix} \mathbf{u}_{s}^{(k)} \\ \mathbf{u}_{m}^{(k)} \end{bmatrix}, \tag{5.5}$$

where the master DOFs are selected by using the ratio of the diagonal terms of mass and stiffness matrices [24-25].

Substituting Eq. (5.5) into Eq. (5.4), the eigenvalue problem of k^{th} substructure can be rewritten as

$$\begin{bmatrix} \mathbf{K}_{ss}^{(k)} & \mathbf{K}_{sm}^{(k)} & \mathbf{B}_{s}^{(k)} \\ \mathbf{K}_{ms}^{(k)} & \mathbf{K}_{mm}^{(k)} & \mathbf{B}_{m}^{(k)} \\ \mathbf{B}_{s}^{(k)T} & \mathbf{B}_{m}^{(k)T} & \mathbf{0} \end{bmatrix} \begin{bmatrix} \mathbf{u}_{s}^{(k)} \\ \mathbf{u}_{m}^{(k)} \\ \boldsymbol{\mu} \end{bmatrix} = \lambda^{(k)} \begin{bmatrix} \mathbf{M}_{ss}^{(k)} & \mathbf{M}_{sm}^{(k)} & \mathbf{0} \\ \mathbf{M}_{ms}^{(k)} & \mathbf{M}_{mm}^{(k)} & \mathbf{0} \\ \mathbf{0} & \mathbf{0} & \mathbf{0} \end{bmatrix} \begin{bmatrix} \mathbf{u}_{s}^{(k)} \\ \mathbf{u}_{m}^{(k)} \\ \boldsymbol{\mu} \end{bmatrix}. \tag{5.6}$$

From the first row equation in Eq. (5.6), $\mathbf{u}_{s}^{(k)}$ is represented by

$$\mathbf{u}_{s}^{(k)} = -(\mathbf{K}_{ss}^{(k)} - \lambda^{(k)}\mathbf{M}_{ss}^{(k)})^{-1}[(\mathbf{K}_{sm}^{(k)} - \lambda^{(k)}\mathbf{M}_{sm}^{(k)})\mathbf{u}_{m}^{(k)} + \mathbf{B}_{s}^{(k)}\boldsymbol{\mu}]. \tag{5.7}$$

Eq. (5.7) can be expanded by Neumann series [8, 10, 27, 40-48] and neglecting higher order terms of $\lambda^{(k)}$, $\mathbf{u}_{s}^{(k)}$ is approximated as

$$\mathbf{u}_{s}^{(k)} \approx \overline{\mathbf{u}}_{s}^{(k)} = [\mathbf{t}_{s}^{(k)} + \lambda^{(k)}\boldsymbol{\Theta}_{s}^{(k)}]\mathbf{u}_{m}^{(k)} + (\mathbf{t}_{\mu}^{(k)} + \lambda^{(k)}\boldsymbol{\Theta}_{\mu}^{(k)})\boldsymbol{\mu}, \tag{5.8}$$

with

$$\mathbf{t}_{s}^{(k)} = -(\mathbf{K}_{ss}^{(k)})^{-1}\mathbf{K}_{sm}^{(k)}, \;\; \boldsymbol{\Theta}_{s}^{(k)} = (\mathbf{K}_{ss}^{(k)})^{-1}(\mathbf{M}_{sm}^{(k)} + \mathbf{M}_{ss}^{(k)}\mathbf{t}_{s}^{(k)}), \tag{5.9a}$$

$$\mathbf{t}_{\mu}^{(k)} = -(\mathbf{K}_{ss}^{(k)})^{-1}\mathbf{B}_{s}^{(k)}, \;\; \boldsymbol{\Theta}_{\mu}^{(k)} = (\mathbf{K}_{ss}^{(k)})^{-1}\mathbf{M}_{ss}^{(k)}\mathbf{t}_{\mu}^{(k)}. \tag{5.9b}$$

Then, using $\overline{\mathbf{u}}_{s}^{(k)}$ instead of $\mathbf{u}_{s}^{(k)}$, the eigenvector of k^{th} substructure in Eq. (5.6) is approximated as

$$\begin{bmatrix} \mathbf{u}_{s}^{(k)} \\ \mathbf{u}_{m}^{(k)} \\ \boldsymbol{\mu} \end{bmatrix} \approx \begin{bmatrix} \overline{\mathbf{u}}_{s}^{(k)} \\ \mathbf{u}_{m}^{(k)} \\ \boldsymbol{\mu} \end{bmatrix} = \mathbf{T}_{0}^{(k)} \begin{bmatrix} \mathbf{u}_{m}^{(k)} \\ \boldsymbol{\mu} \end{bmatrix} + \lambda^{(k)}\mathbf{T}_{a}^{(k)} \begin{bmatrix} \mathbf{u}_{m}^{(k)} \\ \boldsymbol{\mu} \end{bmatrix} \quad \text{with} \tag{5.10a}$$

$$\mathbf{T}_0^{(k)} = \begin{bmatrix} \mathbf{t}_s^{(k)} & \mathbf{t}_\mu^{(k)} \\ \mathbf{I}_m^{(k)} & \mathbf{0} \\ \mathbf{0} & \mathbf{I}_\mu \end{bmatrix}, \mathbf{T}_a^{(k)} = \begin{bmatrix} \mathbf{\Theta}_s^{(k)} & \mathbf{\Theta}_\mu^{(k)} \\ \mathbf{0} & \mathbf{0} \\ \mathbf{0} & \mathbf{0} \end{bmatrix}, \tag{5.10b}$$

where $\mathbf{T}_0^{(k)}$ is the Guyan transformation matrix reflecting the dual substructuring, $\mathbf{T}_a^{(k)}$ is the additional transformation matrix containing the inertial effects of the slave DOFs of the k^{th} substructure. $\mathbf{I}_m^{(k)}$ and $\mathbf{I}_\mu$ are the identity matrices corresponding to the master DOFs of the k^{th} substructure and Lagrange multiplier, respectively.

By considering only the transformation matrix $\mathbf{T}_0^{(k)}$ in Eq. (5.10b), the eigenvalue problem corresponding to the k^{th} substructure in Eq. (5.6) is reduced as follows

$$\overline{\mathbf{K}}_0^{(k)} \begin{bmatrix} \mathbf{u}_m^{(k)} \\ \boldsymbol{\mu} \end{bmatrix} = \overline{\lambda}^{(k)} \overline{\mathbf{M}}_0^{(k)} \begin{bmatrix} \mathbf{u}_m^{(k)} \\ \boldsymbol{\mu} \end{bmatrix} \tag{5.11a}$$

$$\text{with } \overline{\mathbf{M}}_0^{(k)} = \mathbf{T}_0^{(k)T} \begin{bmatrix} \mathbf{M}^{(k)} & \mathbf{0} \\ \mathbf{0} & \mathbf{0} \end{bmatrix} \mathbf{T}_0^{(k)},\ \overline{\mathbf{K}}_0^{(k)} = \mathbf{T}_0^{(k)T} \begin{bmatrix} \mathbf{K}^{(k)} & \mathbf{B}^{(k)} \\ \mathbf{B}^{(k)T} & \mathbf{0} \end{bmatrix} \mathbf{T}_0^{(k)}, \tag{5.11b}$$

in which $\overline{\lambda}^{(k)}$ is the approximated eigenvalue of the k^{th} substructure.

Multiplying $(\overline{\mathbf{M}}_0^{(k)})^{-1}$ on the both sides of Eq. (5.11a), the following relation is obtained

$$\overline{\lambda}^{(k)} \begin{bmatrix} \mathbf{u}_m^{(k)} \\ \boldsymbol{\mu} \end{bmatrix} = \mathbf{H}^{(k)} \begin{bmatrix} \mathbf{u}_m^{(k)} \\ \boldsymbol{\mu} \end{bmatrix} \text{ with } \mathbf{H}^{(k)} = (\overline{\mathbf{M}}_0^{(k)})^{-1} \overline{\mathbf{K}}_0^{(k)}. \tag{5.12}$$

Substituting Eq. (5.12) into Eq. (5.10a), the approximated eigenvector of k^{th} substructure is newly defined as

$$\begin{bmatrix} \bar{\mathbf{u}}_s^{(k)} \\ \mathbf{u}_m^{(k)} \\ \boldsymbol{\mu} \end{bmatrix} = \mathbf{T}_1^{(k)} \begin{bmatrix} \mathbf{u}_m^{(k)} \\ \boldsymbol{\mu} \end{bmatrix} \text{ with } \mathbf{T}_1^{(k)} = \mathbf{T}_0^{(k)} + \mathbf{T}_a^{(k)} \mathbf{H}^{(k)}, \tag{5.13}$$

where $\mathbf{T}_1^{(k)}$ is the transformation matrix of the proposed method. Here, $\mathbf{H}^{(k)}$ is decomposed into the master and Lagrange multiplier parts as follows

$$\mathbf{H}^{(k)} = \begin{bmatrix} \mathbf{H}_{mm}^{(k)} & \mathbf{H}_{\mu m}^{(k)} \\ \mathbf{H}_{m\mu}^{(k)} & \mathbf{H}_{\mu\mu}^{(k)} \end{bmatrix}. \tag{5.14}$$

From Eq. (5.10b), (5.13) and (5.14), $\mathbf{T}_1^{(k)}$ can be expressed as

$$\mathbf{T}_1^{(k)} = \begin{bmatrix} \mathbf{A}^{(k)} & \boldsymbol{\Psi}^{(k)} \\ \mathbf{0} & \mathbf{I}_\mu \end{bmatrix} \text{ with } \mathbf{A}^{(k)} = \begin{bmatrix} \hat{\mathbf{t}}_s^{(k)} \\ \mathbf{I}_m^{(k)} \end{bmatrix}, \ \boldsymbol{\Psi}^{(k)} = \begin{bmatrix} \hat{\mathbf{t}}_\mu^{(k)} \\ \mathbf{0} \end{bmatrix}, \tag{5.15}$$

in which the component matrices $\hat{\mathbf{t}}_s^{(k)}$ and $\hat{\mathbf{t}}_\mu^{(k)}$ are calculated as

$$\hat{\mathbf{t}}_s^{(k)} = \mathbf{t}_s^{(k)} + \boldsymbol{\Theta}_s^{(k)} \mathbf{H}_{mm}^{(k)} + \boldsymbol{\Theta}_\mu^{(k)} \mathbf{H}_{\mu m}^{(k)}, \ \hat{\mathbf{t}}_\mu^{(k)} = \mathbf{t}_\mu^{(k)} + \boldsymbol{\Theta}_s^{(k)} \mathbf{H}_{m\mu}^{(k)} + \boldsymbol{\Theta}_\mu^{(k)} \mathbf{H}_{\mu\mu}^{(k)}. \tag{5.16}$$

The reduced substructural system matrices are calculated as

$$\overline{\mathbf{M}}_1^{(k)} = \mathbf{T}_1^{(k)T} \begin{bmatrix} \mathbf{M}^{(k)} & \mathbf{0} \\ \mathbf{0} & \mathbf{0} \end{bmatrix} \mathbf{T}_1^{(k)}, \overline{\mathbf{K}}_1^{(k)} = \mathbf{T}_1^{(k)T} \begin{bmatrix} \mathbf{K}^{(k)} & \mathbf{B}^{(k)} \\ \mathbf{B}^{(k)T} & \mathbf{0} \end{bmatrix} \mathbf{T}_1^{(k)}, \tag{5.17}$$

and considering the master DOFs and Lagrange multipliers, $\overline{\mathbf{M}}_1^{(k)}$ and $\overline{\mathbf{K}}_1^{(k)}$ are decomposed as

$$\overline{\mathbf{M}}_1^{(k)} = \begin{bmatrix} \overline{\mathbf{M}}_{mm}^{(k)} & \overline{\mathbf{M}}_{m\mu}^{(k)} \\ \overline{\mathbf{M}}_{\mu m}^{(k)} & \overline{\mathbf{M}}_{\mu\mu}^{(k)} \end{bmatrix}, \ \overline{\mathbf{K}}_1^{(k)} = \begin{bmatrix} \overline{\mathbf{K}}_{mm}^{(k)} & \overline{\mathbf{K}}_{m\mu}^{(k)} \\ \overline{\mathbf{K}}_{\mu m}^{(k)} & \overline{\mathbf{K}}_{\mu\mu}^{(k)} \end{bmatrix}. \tag{5.18}$$

Then, after obtaining Eq. (5.18) for all substructures, the reduced mass and stiffness matrices for the global FE model considered is simply assembled as follows

$$\overline{\mathbf{M}} = \left[\begin{array}{ccc|c} \overline{\mathbf{M}}_{mm}^{(1)} & & \mathbf{0} & \overline{\mathbf{M}}_{m\mu}^{(1)} \\ & \ddots & & \vdots \\ \mathbf{0} & & \overline{\mathbf{M}}_{mm}^{(N_s)} & \overline{\mathbf{M}}_{m\mu}^{(N_s)} \\ \hline \overline{\mathbf{M}}_{\mu m}^{(1)} & \cdots & \overline{\mathbf{M}}_{\mu m}^{(N_s)} & \overline{\mathbf{M}}_{\mu\mu} \end{array}\right], \quad \overline{\mathbf{K}} = \left[\begin{array}{ccc|c} \overline{\mathbf{K}}_{mm}^{(1)} & & \mathbf{0} & \overline{\mathbf{K}}_{m\mu}^{(1)} \\ & \ddots & & \vdots \\ \mathbf{0} & & \overline{\mathbf{K}}_{mm}^{(N_s)} & \overline{\mathbf{K}}_{m\mu}^{(N_s)} \\ \hline \overline{\mathbf{K}}_{\mu m}^{(1)} & \cdots & \overline{\mathbf{K}}_{\mu m}^{(N_s)} & \overline{\mathbf{K}}_{\mu\mu} \end{array}\right], \tag{5.19a}$$

$$\text{with } \overline{\mathbf{M}}_{\mu\mu} = \sum_{k=1}^{N_s} \overline{\mathbf{M}}_{\mu\mu}^{(k)}, \ \overline{\mathbf{K}}_{\mu\mu} = \sum_{k=1}^{N_s} \overline{\mathbf{K}}_{\mu\mu}^{(k)}, \tag{5.19b}$$

note that N_1 is the number of DOFs in the reduced FE model: $N_1 = N_\mu + \sum_{k=1}^{N_s} N_m^{(k)}$, where $N_m^{(k)}$ is the number of master DOFs of the k^{th} substructure.

The reduced eigenvalue problem of the present method is given by

$$\overline{\mathbf{K}}(\overline{\boldsymbol{\varphi}})_i = \bar{\lambda}_i \overline{\mathbf{M}}(\overline{\boldsymbol{\varphi}})_i, \ i = 1,2,\cdots,N_1, \tag{5.20}$$

where $\bar{\lambda}_i$ and $(\overline{\boldsymbol{\varphi}})_i$ are the approximated i^{th} eigenvalues and corresponding eigenvectors in the present method.

The approximated global eigenvector $(\overline{\boldsymbol{\varphi}}_g)_i$ can be calculated by

$$(\overline{\boldsymbol{\varphi}}_g)_i = \overline{\mathbf{T}}(\overline{\boldsymbol{\varphi}})_i \ \text{ with } \ \overline{\mathbf{T}} = \left[\begin{array}{ccc|c} \mathbf{A}^{(1)} & & \mathbf{0} & \boldsymbol{\Psi}^{(1)} \\ & \ddots & & \vdots \\ \mathbf{0} & & \mathbf{A}^{(N_s)} & \boldsymbol{\Psi}^{(N_s)} \\ \hline \mathbf{0} & \cdots & \mathbf{0} & \mathbf{I}_\mu \end{array}\right], \tag{5.21}$$

in which $\overline{\mathbf{T}}$ is assembled by using the already calculated transformation matrices $\mathbf{T}_1^{(k)}$ in Eq. (5.15).

In the present method, it is possible to independently perform the process for each substructure from construction to reduction. Since we do not have to deal with the global FE model, we can efficiently reduce the large structural FE model that cannot be handled by the original IRS method [17]. The flow chart of the present reduction method is shown in the Fig. 5.1. In the following sections, the accuracy and computational cost is investigated using various examples.

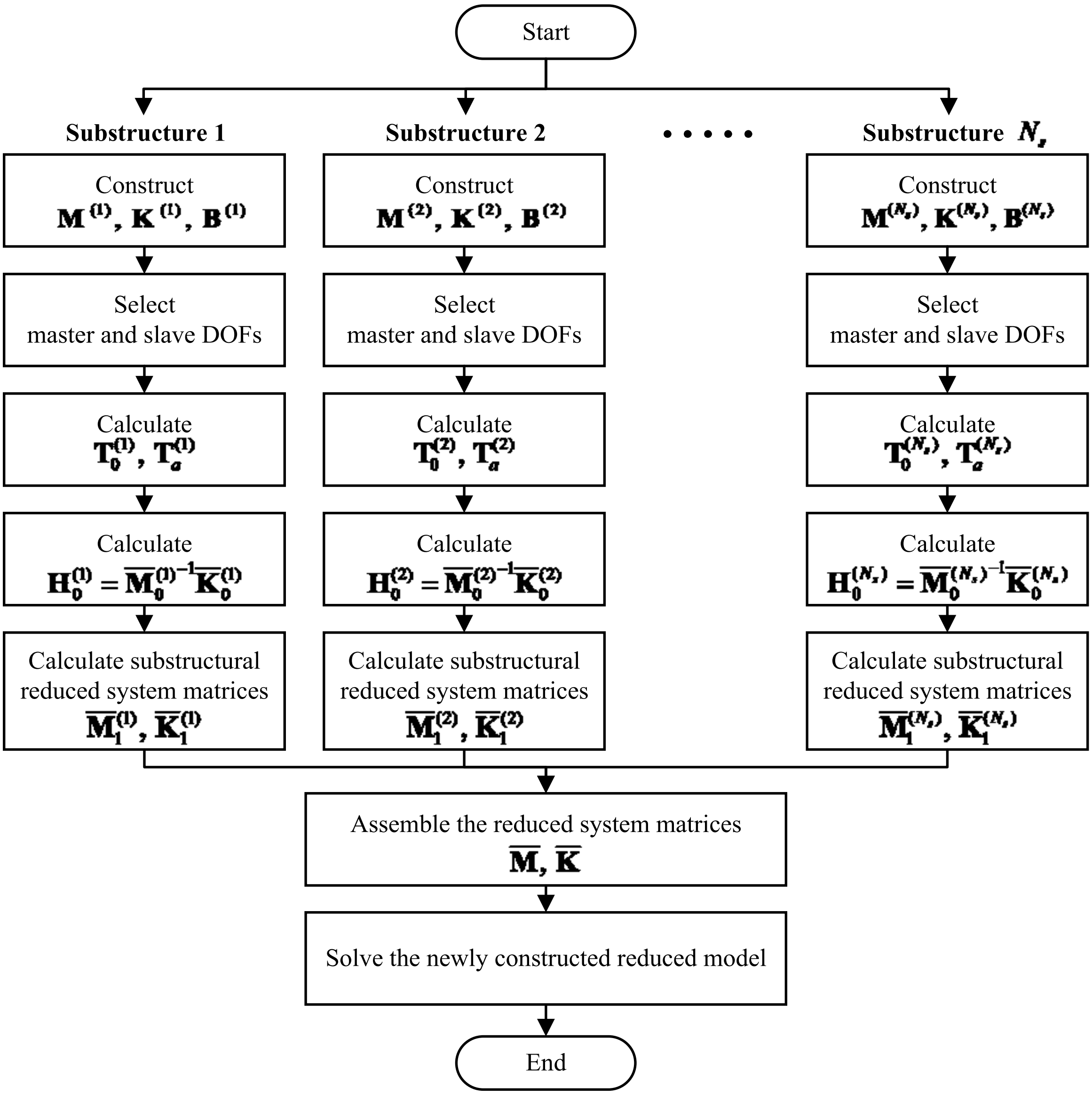

Figure 5.1. Flow chart for the FE model reduction

5.2 Numerical examples

In this section, we investigate the performance of the present method compared to the original IRS method [17]. We considered seven structural problems: a rectangular plate with matching and non-matching meshes, a plate with a hole, a hyperboloid shell, a bended pipe with matching and non-matching meshes, a wind turbine rotor, a NACA 2415 wing with ailerons, and a cable-stayed bridge.

For the finite element modeling, the 4-node MITC shell [65-70], 3D solid, and truss elements are used and free or fixed boundary conditions are imposed differently according to the problem. All the computer codes are implemented in MATLAB and computation is performed in a personal computer (Inter core (TM) i7-4770, 3.40 GHz CPU, 32 GB RAM).

The relative eigenvalue error is adopted to measure the accuracy of the reduced models

$$\xi_i = \frac{\left|\lambda_i - \bar{\lambda}_i\right|}{\lambda_i} \tag{5.22}$$

in which ξ_i is the i^{th} relative eigenvalue error, λ_i is the i^{th} exact eigenvalue calculated from the global eigenvalue problem in Eq. (5.2); and $\bar{\lambda}_i$ is the i^{th} approximated eigenvalue calculated from the reduced eigenvalue problem. Note that the rigid body modes are not considered in measuring the accuracy.

The accuracy of approximated eigenvector of the present method is measured by the modal assurance criterion (MAC) [59-60] as

$$\text{MAC}(i,j) = \frac{|(\boldsymbol{\varphi}_g)_i^T(\bar{\boldsymbol{\varphi}}_g)_j|^2}{((\boldsymbol{\varphi}_g)_i^T(\boldsymbol{\varphi}_g)_i)((\bar{\boldsymbol{\varphi}}_g)_j^T(\bar{\boldsymbol{\varphi}}_g)_j)} \quad \text{for } i,j = 1,2,\cdots,N_g, \tag{5.23}$$

in which $(\boldsymbol{\varphi}_g)$ and $(\bar{\boldsymbol{\varphi}}_g)$ are the global and approximated eigenvector calculated by Eq. (5.2) and (5.21), respectively. The resulting scalars are assembled into the MAC matrix. The MAC indicate the consistency between eigenvectors by its value from zero to unity. If the MAC has a value near unity, the eigenvectors are considered consistent. Note that the rigid body modes are not considered in measuring the consistency of eigenvectors.

5.2.1 Rectangular plate problem

Let us consider a rectangular plate with free boundary. Length L is 0.6096 m, width B is 0.3048 m, and thickness h is 3.18×10^{-3} m. Young's modulus E is 72 GPa, Poisson's ratio ν is 0.33, and density ρ is 2796 $\mathrm{kg/m^3}$. The whole structure is an assemblage of two substructures ($N_s = 2$) modeled by 4-node MITC shell elements [65-70]. We consider two numerical cases, with matching and non-matching meshes between neighboring substructures.

For the matching mesh case, the first substructure is modeled using an 8×6 mesh and the second substructure is modeled using a 4×6 mesh, as shown in Fig. 5.2. Here, we consider original IRS method and the present method with same master DOFs selected. The selected nodes are illustrated as in Fig. 5.2a and b. At each selected nodes, all DOFs are considered as master DOFs. The number of master DOFs used and the number of DOFs in original and reduced are listed in Table 5.1.

Fig. 5.3 presents the eigenvalues obtained by the non-reduced exact FE model, the original Guyan and IRS methods and the present method. Fig. 5.4 presents the relative eigenvalue errors obtained by the original Guyan, IRS and present methods. The present method has similar accuracy to the original IRS. The original IRS method can reduce the structural FE model more stably because it does not require the assumption of substructuring and interface boundary. However, it is difficult to utilize the original IRS method when the structural FE model has large DOFs or non-matching mesh. In the following numerical examples will show that the present method can solve these drawbacks.

For the non-matching mesh case, see Fig. 5.5a, the first substructure is modeled by an 8×6 mesh and the second substructure is modeled by an 8×12 mesh. The interface compatibility is considered through nodal collocation and thus the matrices $\mathbf{B}^{(i)}$ are no longer Boolean. The selected nodes are illustrated as in Fig. 5.5b. At each selected nodes, all DOFs are considered as master DOFs.

Fig. 5.6 the relative eigenvalue errors obtained by the present methods. The original IRS method cannot be directly applied to these non-matching mesh problems. Compared to the accuracy of the matching mesh case, the results also show that the present method provides accurate solutions for this non-matching mesh case.

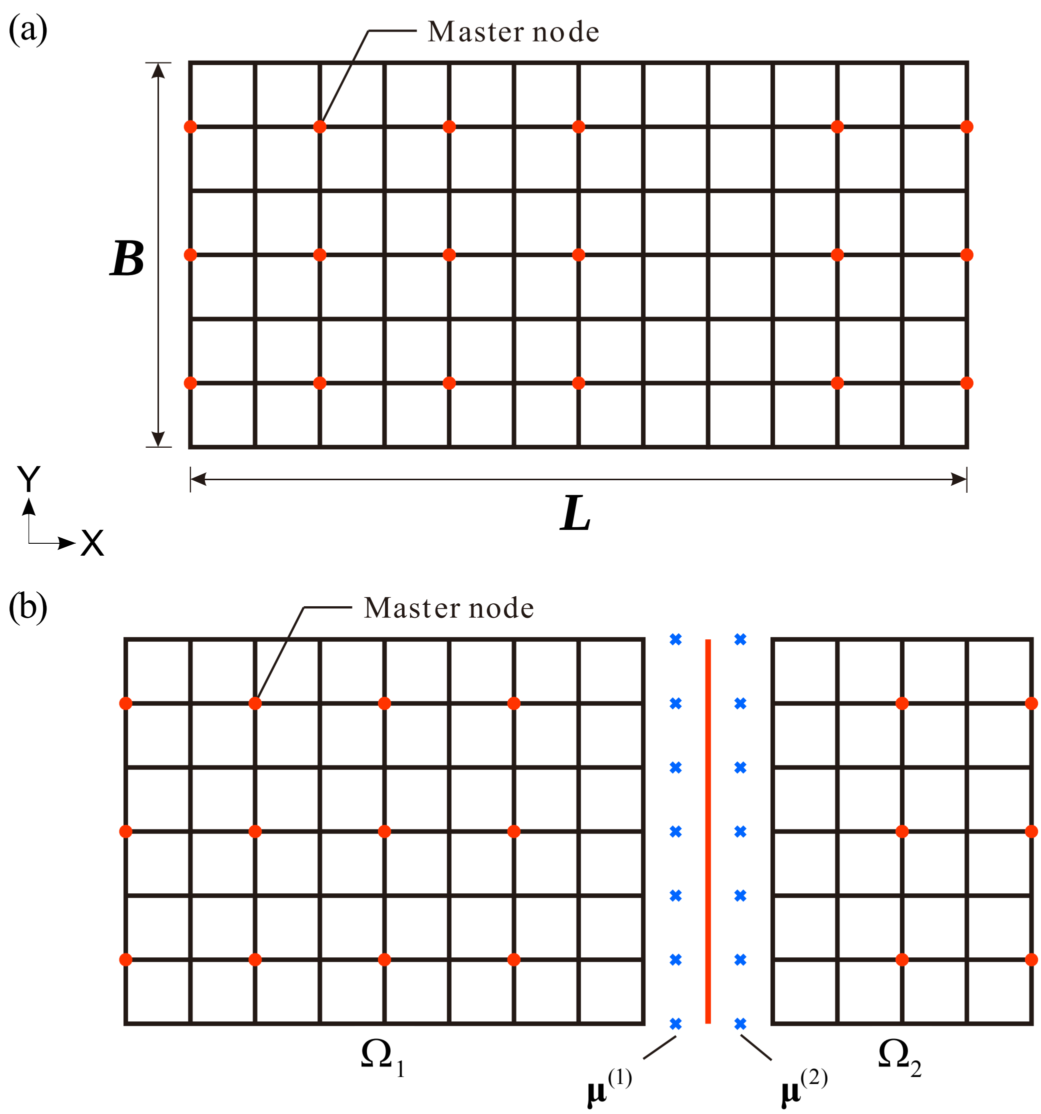

Figure 5.2. Rectangular plate problem with matching mesh: (a) Selected nodes in the original IRS method, (b) Selected nodes in the present method.

Table 5.1. Number of master DOFs used and number of DOFs in original and reduced systems for the rectangular plate problem (12×6 mesh).

Methods	$N_m^{(1)}$	$N_m^{(2)}$	N_m	N_b	N_g	N_1
Original Guyan	-	-	90	-	455	90
Original IRS	-	-	90	-	455	90
Present	60	30	90	35	525	125

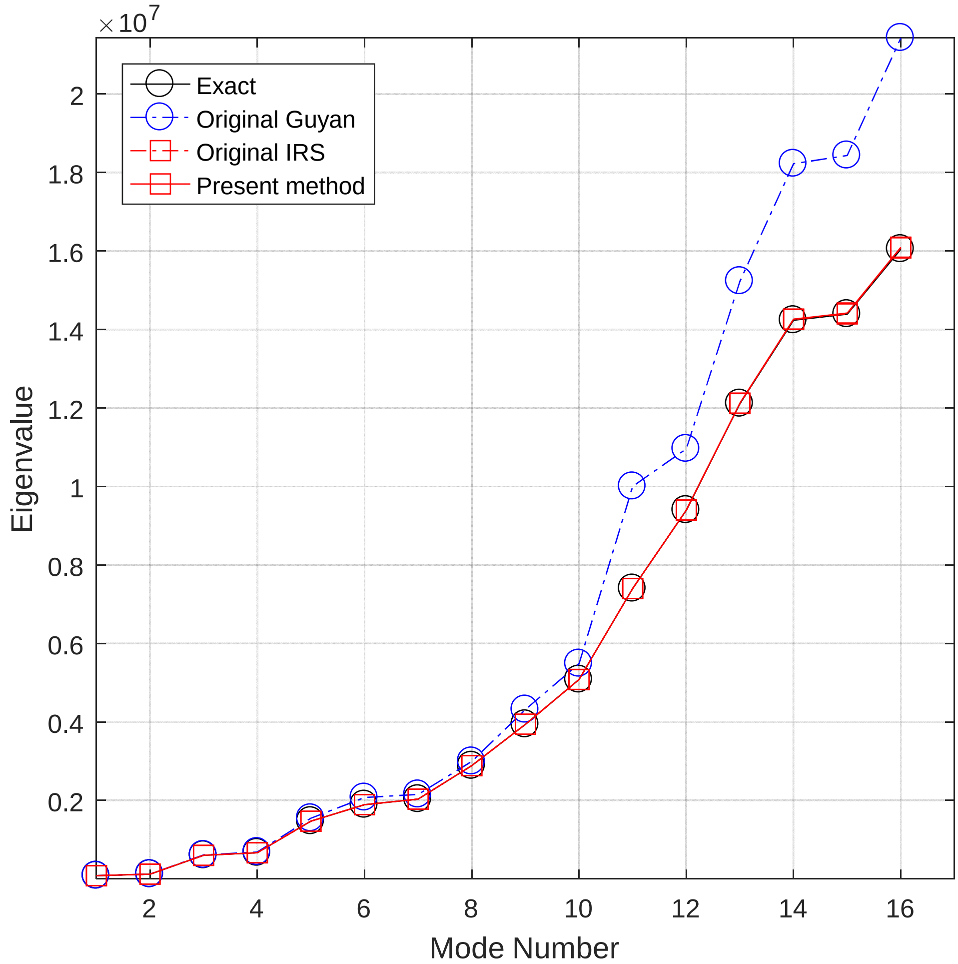

Figure 5.3. Exact and approximated eigenvalues in the rectangular plate problem with matching mesh.

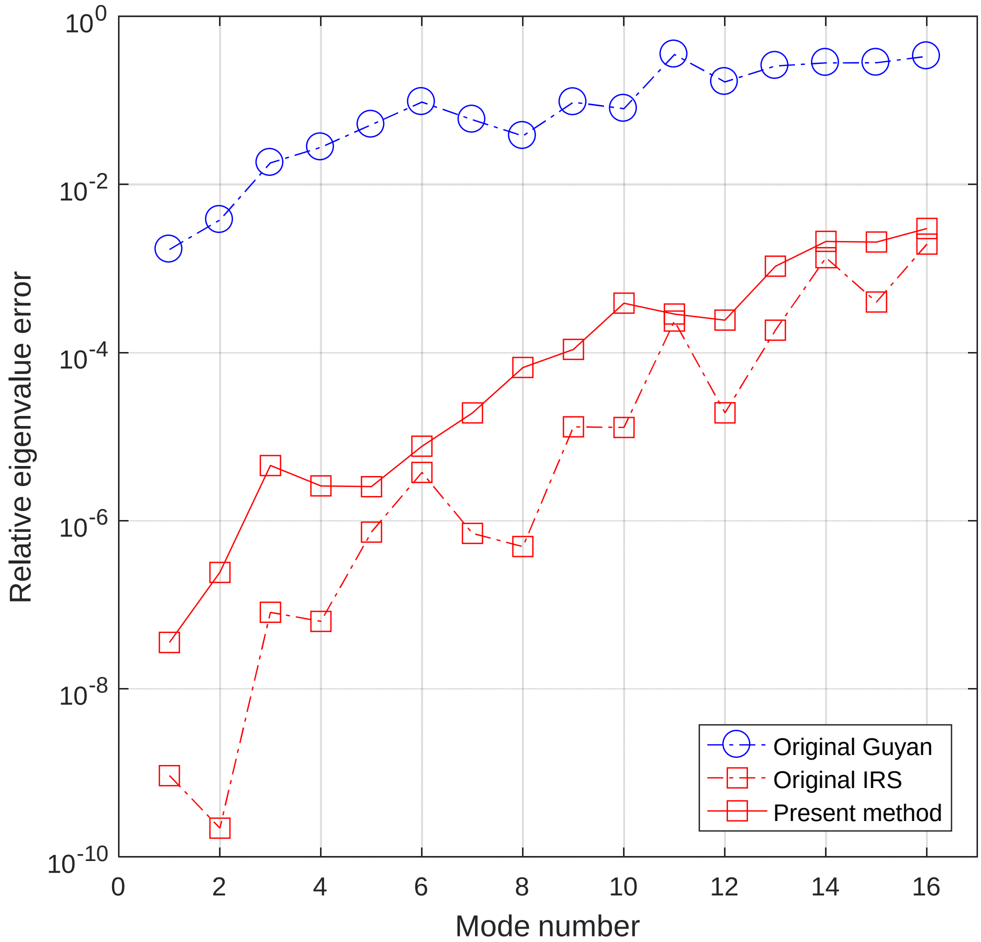

Figure 5.4. Relative eigenvalue errors in the rectangular plate problem with matching mesh.

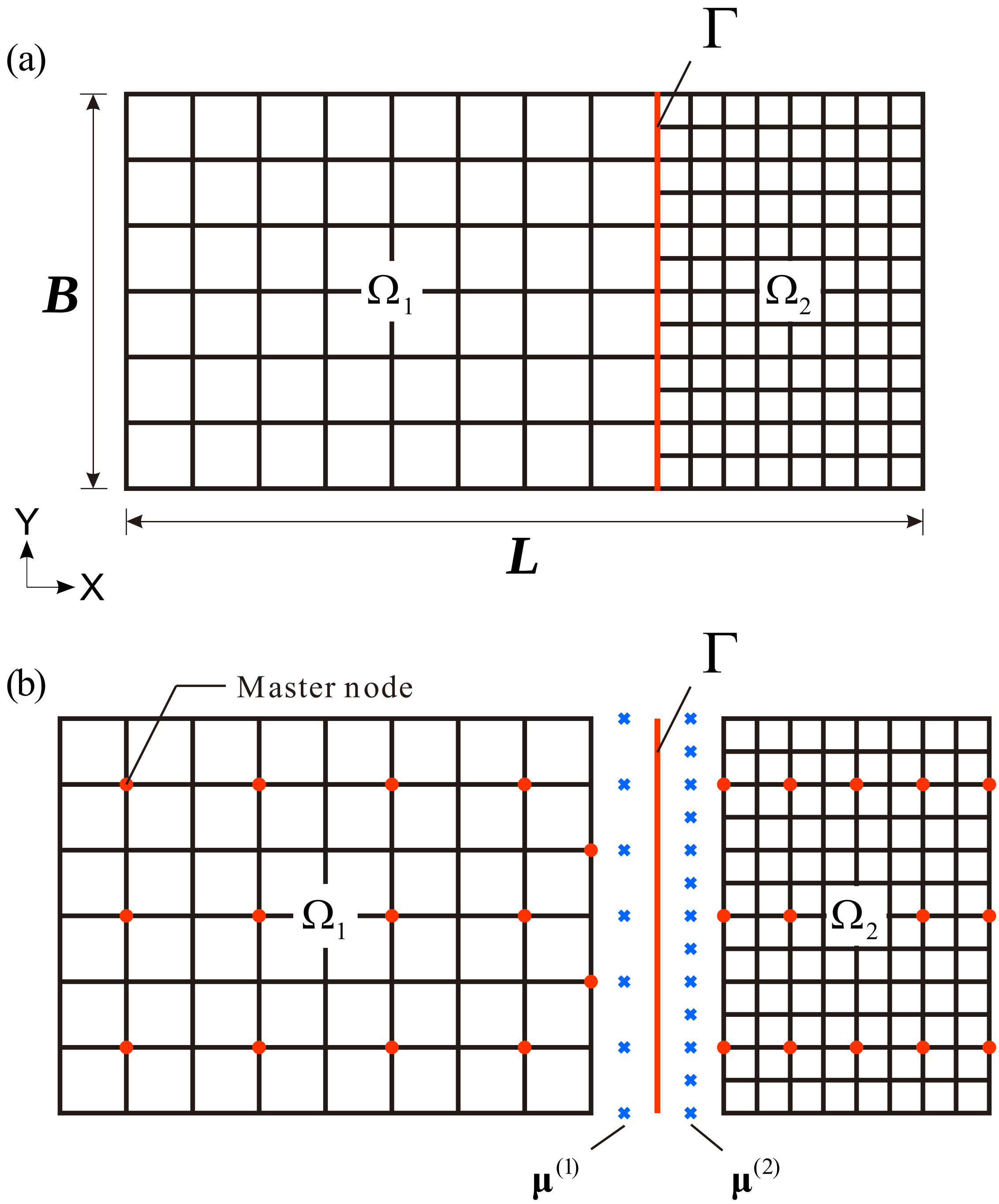

Figure 5.5. Rectangular plate problem with non-matching mesh: (a) Non-matching mesh between neighboring substructures, (b) Selected nodes in the present method.

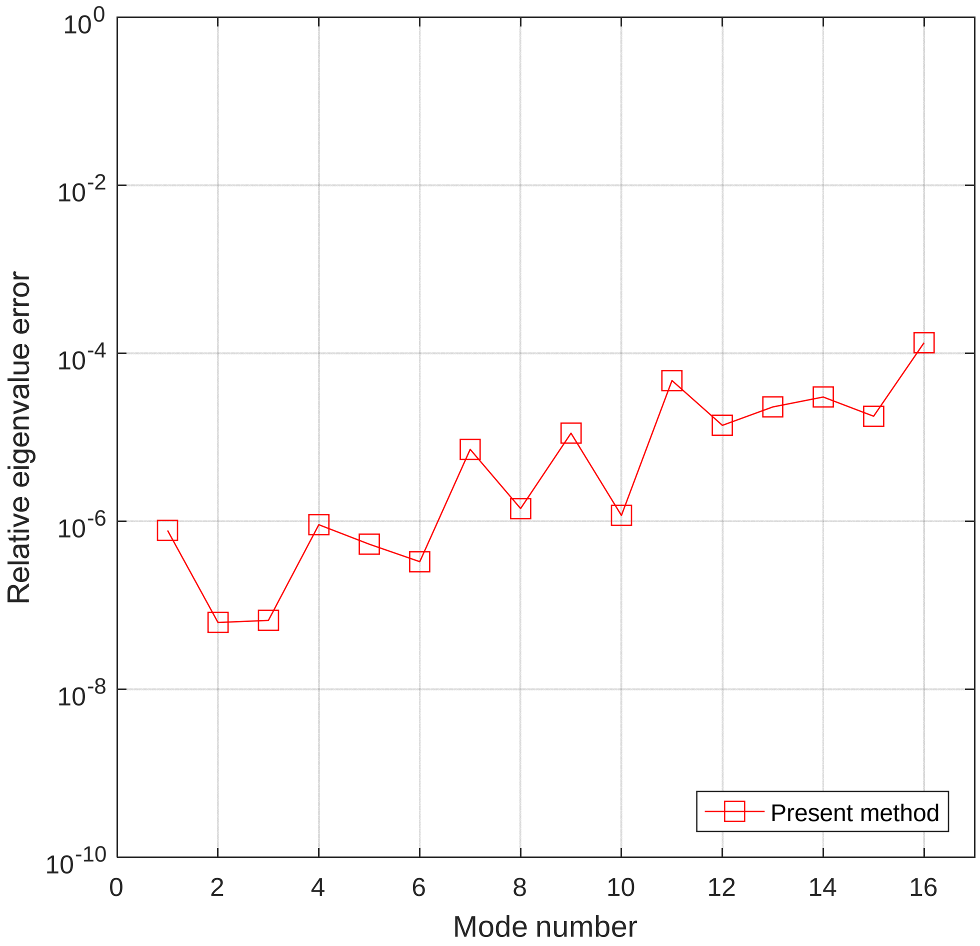

Figure 5.6. Relative eigenvalue errors in the rectangular plate problem with non-matching mesh.

5.2.2 Plate structure with a hole

Let us consider a rectangular plate with a hole, see Fig. 5.7. No boundary condition is imposed. The length L is 20 m, width B is 10 m, and thickness h is 0.25 m. Young's modulus E is 210 GPa, Poisson's ratio ν is 0.3, and density ρ is 7850 $\mathrm{kg/m^3}$. The whole model is an assemblage of four substructural FE models ($N_s = 4$). The whole model is discretized by 208 shell elements (1360 DOFs). The substructures are symmetrically positioned about the hole in center.

We consider two numerical cases with different master DOFs selected. The master DOFs are selected as shown in Fig. 5.7a and b. The numbers of master DOFs used and the numbers of DOFs in the original and reduced systems are presented in Table 5.2. Fig. 5.8 presents the relative eigenvalue errors obtained using the present methods. The results show that it is possible to accurately predict the low-order mode even if only the interface DOFs of each sub-structure are selected and it is obvious that the accuracy to the higher modes can be improved when the internal DOFS are further selected.

Fig. 5.9 presents the MAC for reduced system by the present method. In both cases, the diagonal component of the MAC in low frequency range has a value close to unity. Therefore, it is observed that consistency is satisfied corresponding to the eigenvectors of the non-reduced global FE model.

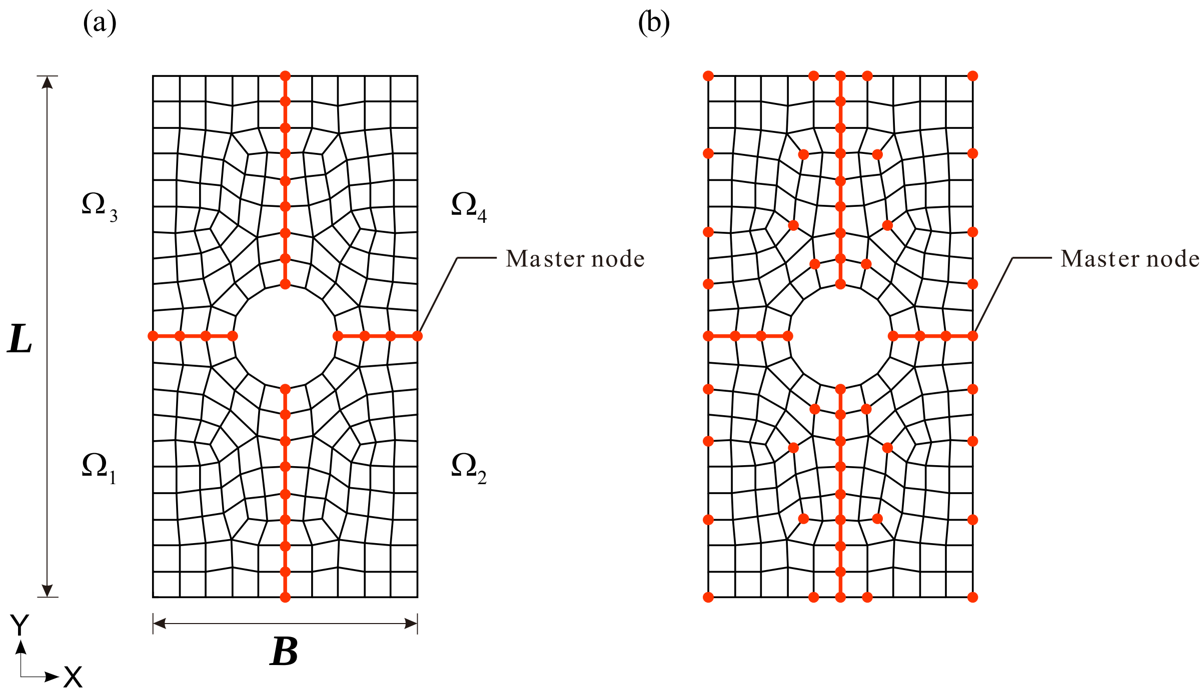

Figure 5.7. Selected nodes in the plate structure with a hole: (a) only interface nodes selected, (b) interface nodes and 8 interior nodes selected in each substructure.

Table 5.2. Number of master DOFs used and number of DOFs in original and reduced systems for the plate structure with a hole.

Methods	$N_m^{(1)}$	$N_m^{(2)}$	$N_m^{(3)}$	$N_m^{(4)}$	N_m	N_b	N_g	N_1
Present (Case 1)	65	65	65	65	260	130	1490	390
Present (Case 2)	105	105	105	105	420	130	1490	550

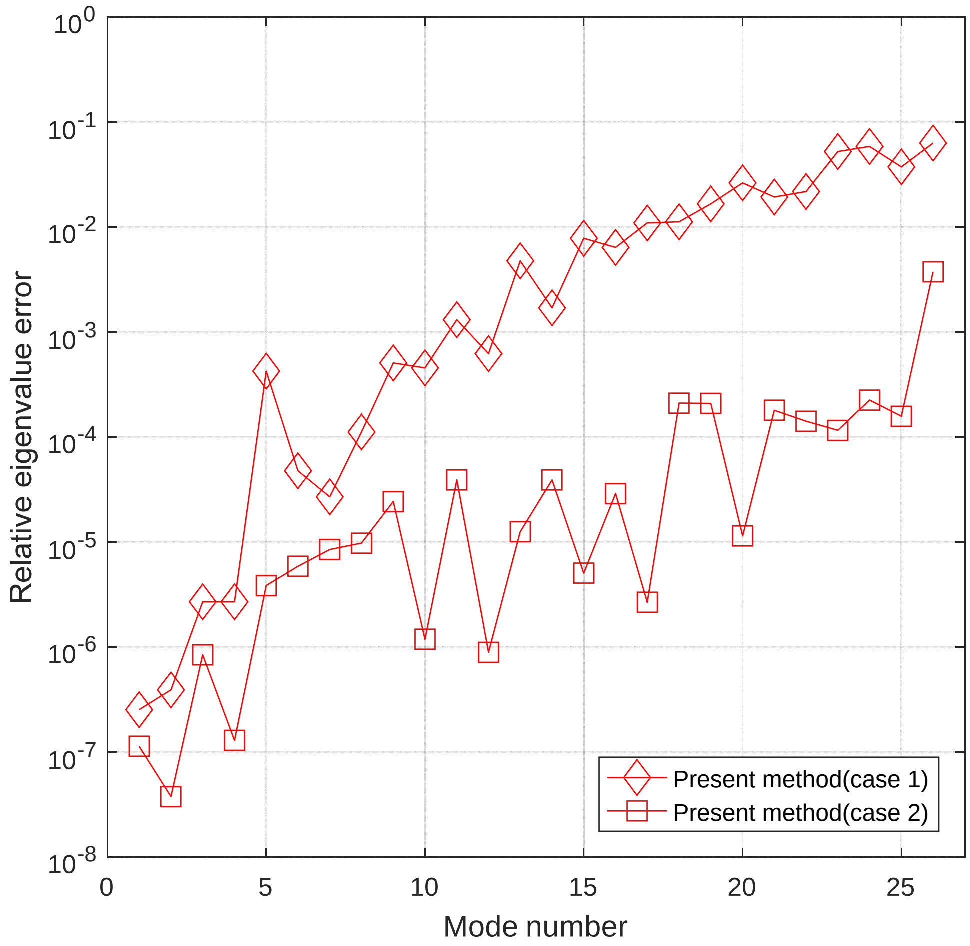

Figure 5.8. Relative eigenvalue errors in the plate structure with a hole.

(a)

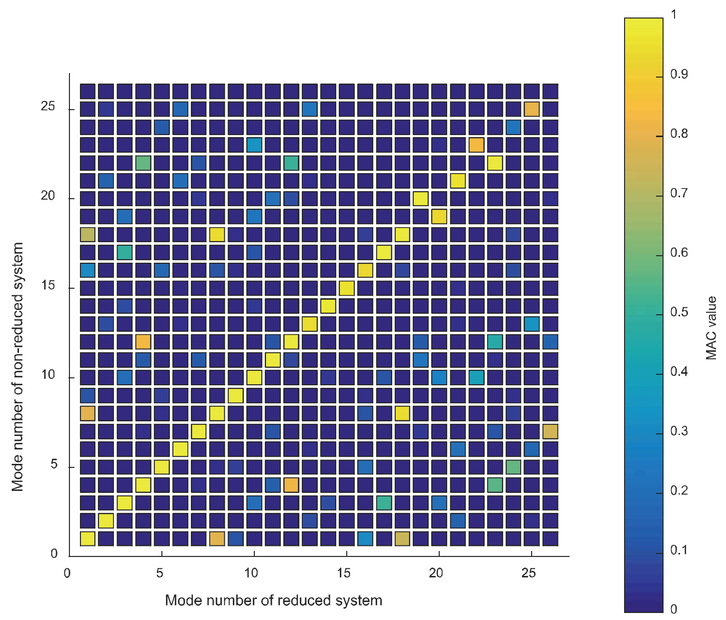

(b)

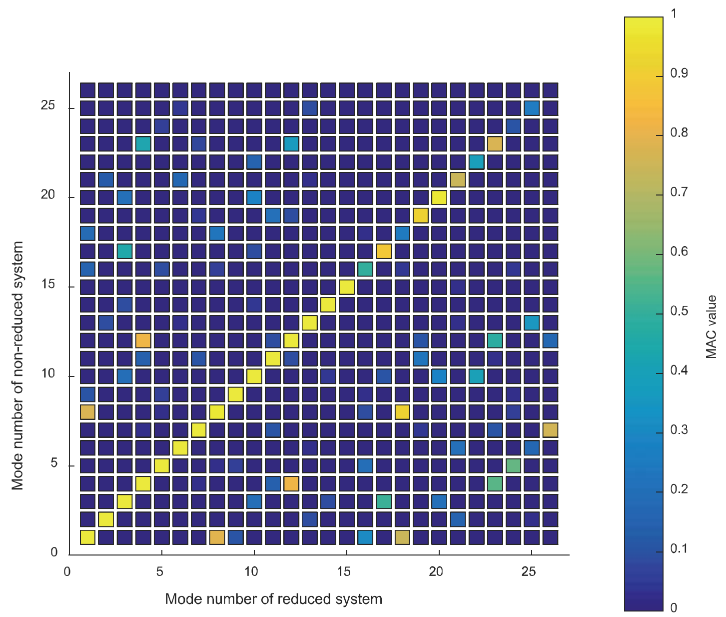

Figure 5.9. MAC for reduced system by the present method in the plate structure with a hole: (a) case 1, (b) case 2.

5.2.3 Hyperboloid shell problem

We here consider a hyperboloid shell structure with free boundary as shown in Fig. 5.9. Height H is 4.0 m and thickness h is 0.05 m. Young's modulus E is 69 GPa, Poisson's ratio ν is 0.35, and density ρ is 2700 $\mathrm{kg/m^3}$. The mid-surface of this shell structure is described by

$$x^2 + y^2 = 2 + z^2; \quad z \in [-2,2]. \tag{5.18}$$

Three substructures ($N_s = 3$) are assembled to construct the original FE model of the shell structures, in which 800 shell elements and 903 nodes are used (4200 DOFs). The selected master DOFs contain all interface DOFs and 2% of interior DOFs for each sub-structure. The master DOFs are selected by using the ratio of the diagonal terms of mass and stiffness matrices [24-25]. The numbers of master DOFs used and the numbers of DOFs in the original and reduced systems are presented in Table 5.3.

Fig. 5.11 presents the relative eigenvalue errors obtained using the present methods. The first 25 eigenvalues calculated by the non-reduced exact FE model and present method are listed in Table 5.4, in which mode numbers are sorted by the magnitude of eigenvalues. The results consistently show the accuracy of the present method.

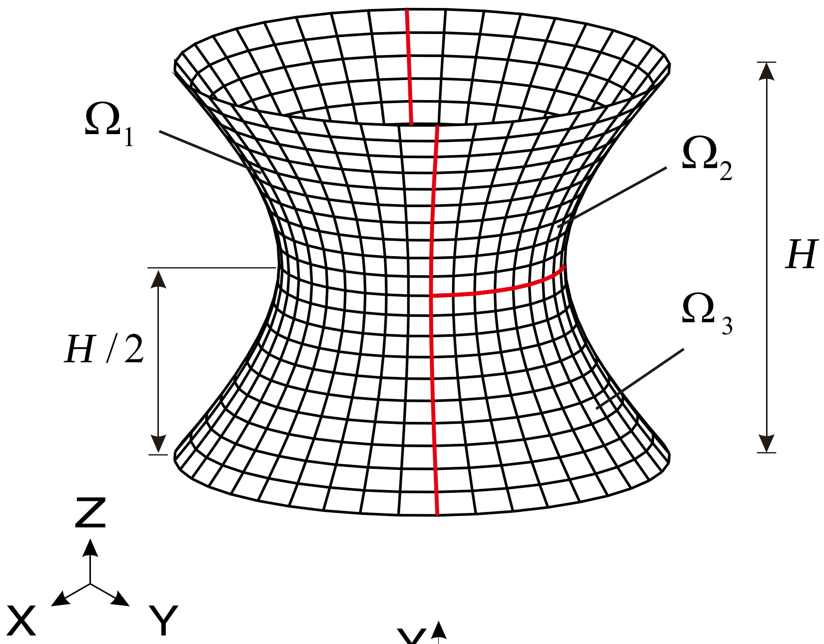

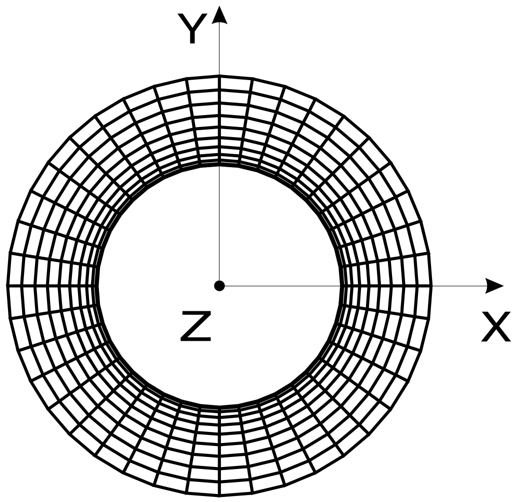

Figure 5.10. Hyperboloid shell problem.

Table 5.3. Number of master DOFs used and number of DOFs in original and reduced systems for the Hyperboloid shell problem.

Methods	$N_m^{(1)}$	$N_m^{(2)}$	$N_m^{(3)}$	N_m	N_b	N_g	N_1
Present	250	225	225	700	315	4830	1015

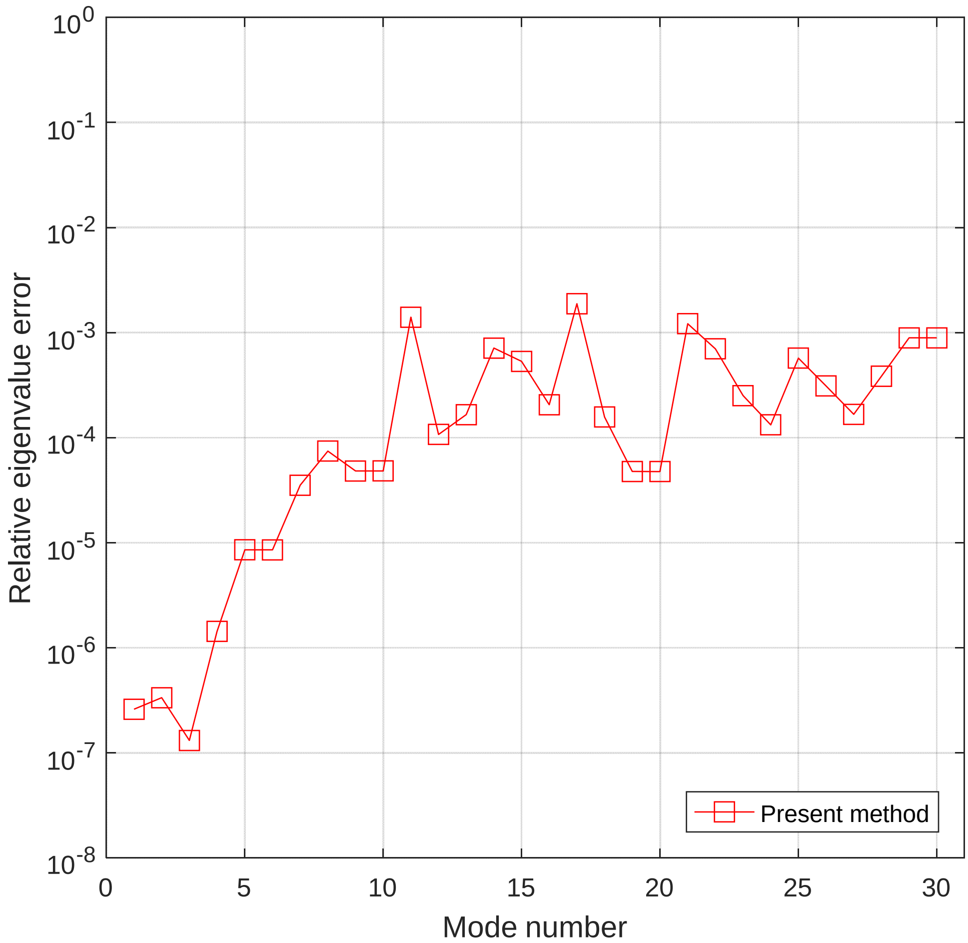

Figure 5.11. Relative eigenvalue errors in the hyperboloid shell problem.

Table 5.4. Eigenvalues calculated for the hyperboloid shell problem.

No.	Exact	Present method
1	5.3715E+03	5.3715E+03
2	5.3715E+03	5.3715E+03
3	1.8569E+04	1.8569E+04
4	1.8569E+04	1.8569E+04
5	4.7642E+04	4.7643E+04
6	4.7642E+04	4.7643E+04
7	7.1066E+04	7.1064E+04
8	7.1066E+04	7.1072E+04
9	1.3395E+05	1.3394E+05
10	1.3395E+05	1.3394E+05
11	2.2742E+05	2.2710E+05
12	2.2742E+05	2.2744E+05
13	2.9949E+05	2.9944E+05
14	2.9949E+05	2.9970E+05
15	3.1100E+05	3.1083E+05
16	3.1100E+05	3.1094E+05
17	4.4692E+05	4.4608E+05
18	4.4692E+05	4.4699E+05
19	4.7120E+05	4.7122E+05
20	4.7120E+05	4.7122E+05
21	4.9582E+05	4.9521E+05
22	4.9582E+05	4.9616E+05
23	5.2752E+05	5.2739E+05
24	5.2752E+05	5.2759E+05
25	5.3151E+05	5.3120E+05

5.2.4 Bended pipe problem

A bended pipe structure with clamped boundary at one end is considered as shown in Fig. 5.12, in which the structural configuration and specification are illustrated. Young's modulus E is 69 GPa, Poisson's ratio ν is 0.35, and density ρ is 2700 $\mathrm{kg/m^3}$. The FE model of the pipe structure is an assemblage of three substructural FE models ($N_s = 3$). We consider the structural FE model with matching and non-matching meshes between neighboring substructures. In the IRS and present method, the master DOFs are selected by using the ratio of the diagonal terms of mass and stiffness matrices [24-25]. The detailed numbers of DOFs in original and reduced are listed in Table 5.5.

For the matching mesh, the whole FE model has 5640 shell elements. To investigate the accuracy and computational efficiency of the present method compared to the original IRS method, the following numerical cases are considered:

- The original Guyan and IRS method are used with the reduced model size of $N_1 = 2340$ ($N_m = 2340$), see Fig. 5.12a.
- The present method is used with the reduced model size of $N_1 = 2340$ ($N_m = 1940$), see Fig. 5.12b.

Fig. 5.13 presents the relative eigenvalue errors obtained by the original Guyan, IRS and present methods. When reduced models of the same size ($N_1 = 2340$) are considered, the present method has similar accuracy to the original IRS method and has significantly improved accuracy compared to the original Guyan method.

Fig. 5.14 presents the MAC for reduced system by the present method. In this case, the approximated eigenvectors have accurate consistency when compared to the eigenvectors of the non-reduced FE model.

Next, the computational costs of the original IRS and present methods are compared. Table 5.6 shows the detailed computational costs. For reduced models of the same size, the computation time required for the present method is only 37.15%, compared to the original IRS method. The computational cost is reduced a lot using the present method. The numerical results demonstrate the solution accuracy and computational efficiency of the present method.

Let us consider the non-matching mesh case, see Fig. 5.12c. The substructural FE models have 1800, 460, 500 shell elements, respectively. Non-matching mesh is located at the interface between neighboring substructures, Ω_1 and Ω_2. The present method is used with the reduced model size of $N_1 = 1215$ ($N_m = 915$).

Fig. 5.15 presents the relative eigenvalue errors obtained by the present methods. The graph in the figure consistently shows the accuracy of the present method for this non-matching mesh case. Fig. 5.16 presents the MAC for reduced system by the present method. In this non-matching mesh case, the approximated eigenvectors also maintain the excellent consistency when compared to the eigenvectors of the non-reduced FE model.

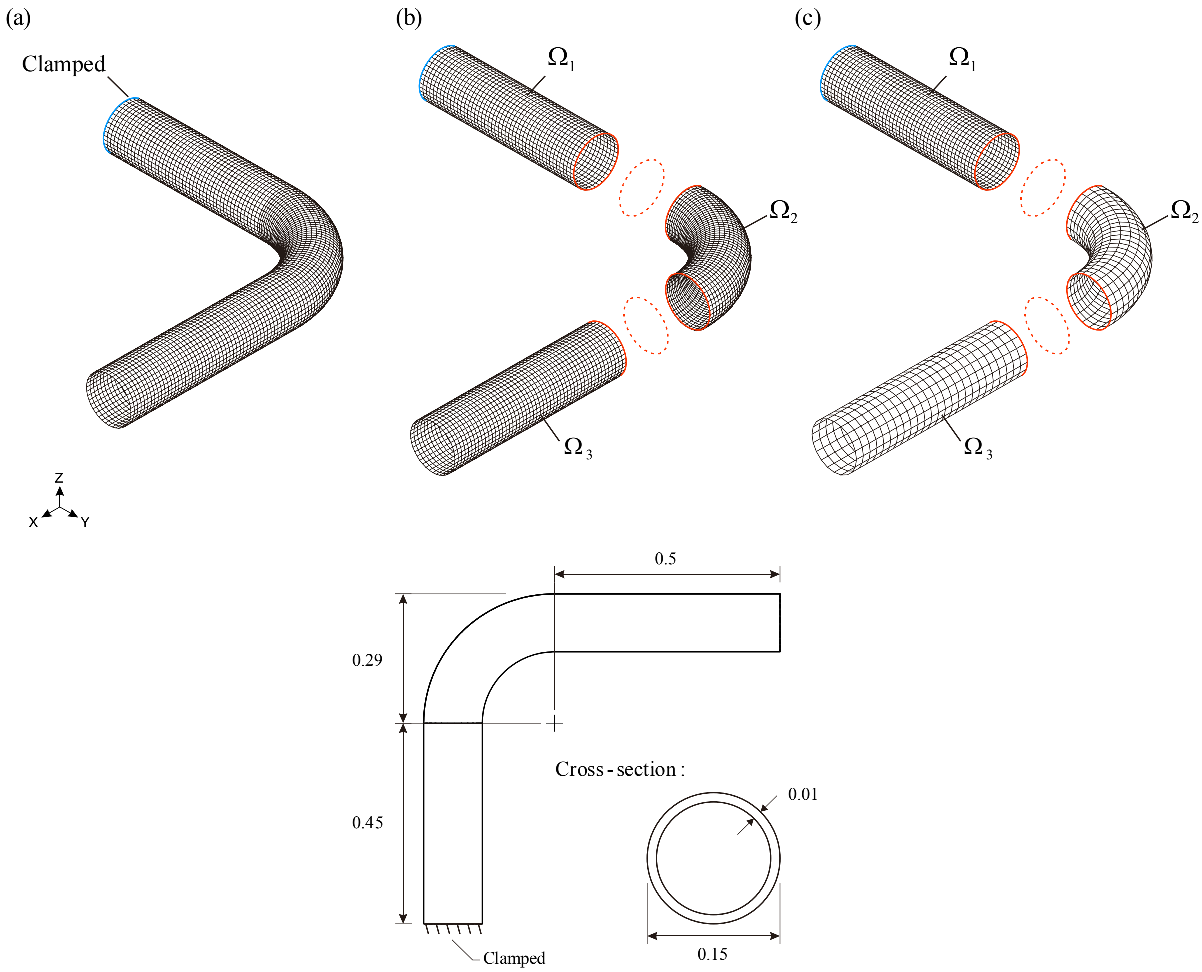

Figure 5.12. Bended pipe problem: (a) Global FE model without substructuring, (b) Matching mesh on the interface, (c) Non-matching mesh between neighboring substructures.

Table 5.5. Number of master DOFs used and number of DOFs in original and reduced systems for the bended pipe problem.

Cases	Methods	$N_m^{(1)}$	$N_m^{(2)}$	$N_m^{(3)}$	N_m	N_b	N_g	N_1
Matching mesh	Guyan	-	-	-	2340	-	28200	2340
	IRS	-	-	-	2340	-	28200	2340
	Present	560	775	605	1940	400	29000	2340
Non-matching mesh	Present	470	270	175	915	300	14300	1215

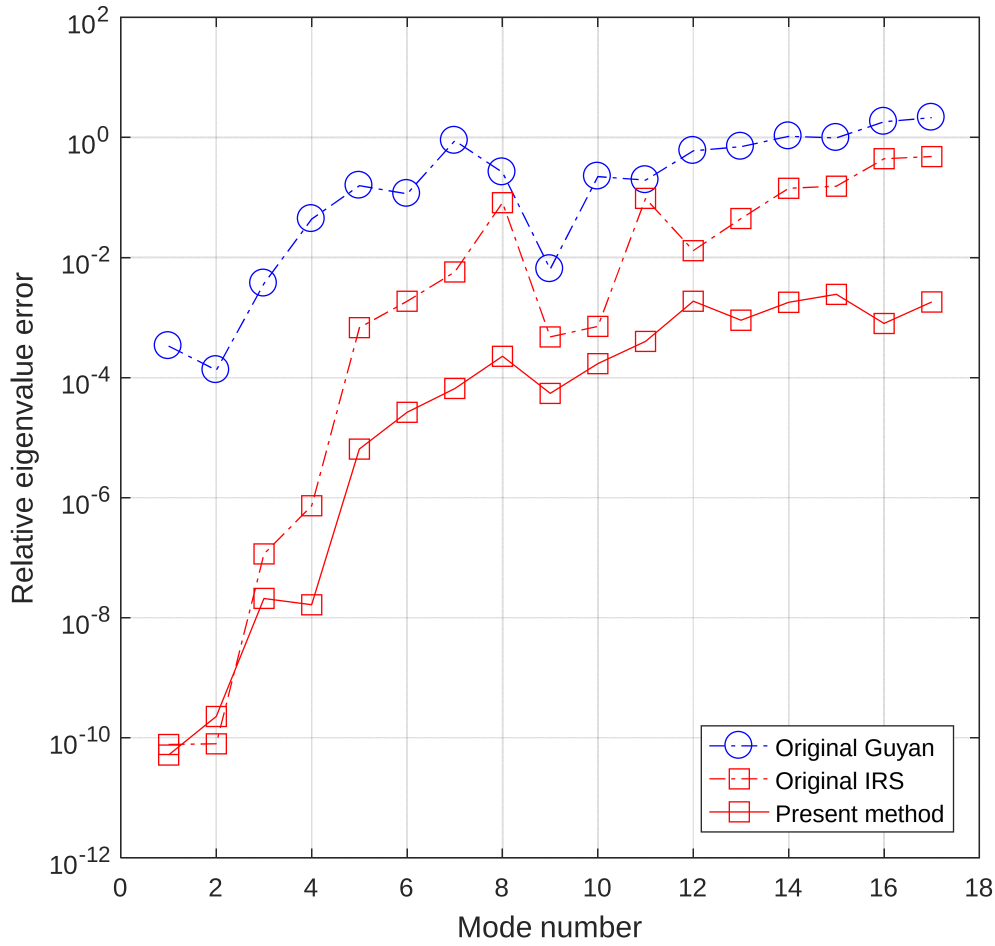

Figure 5.13. Relative eigenvalue errors in the bended pipe problem with matching mesh.

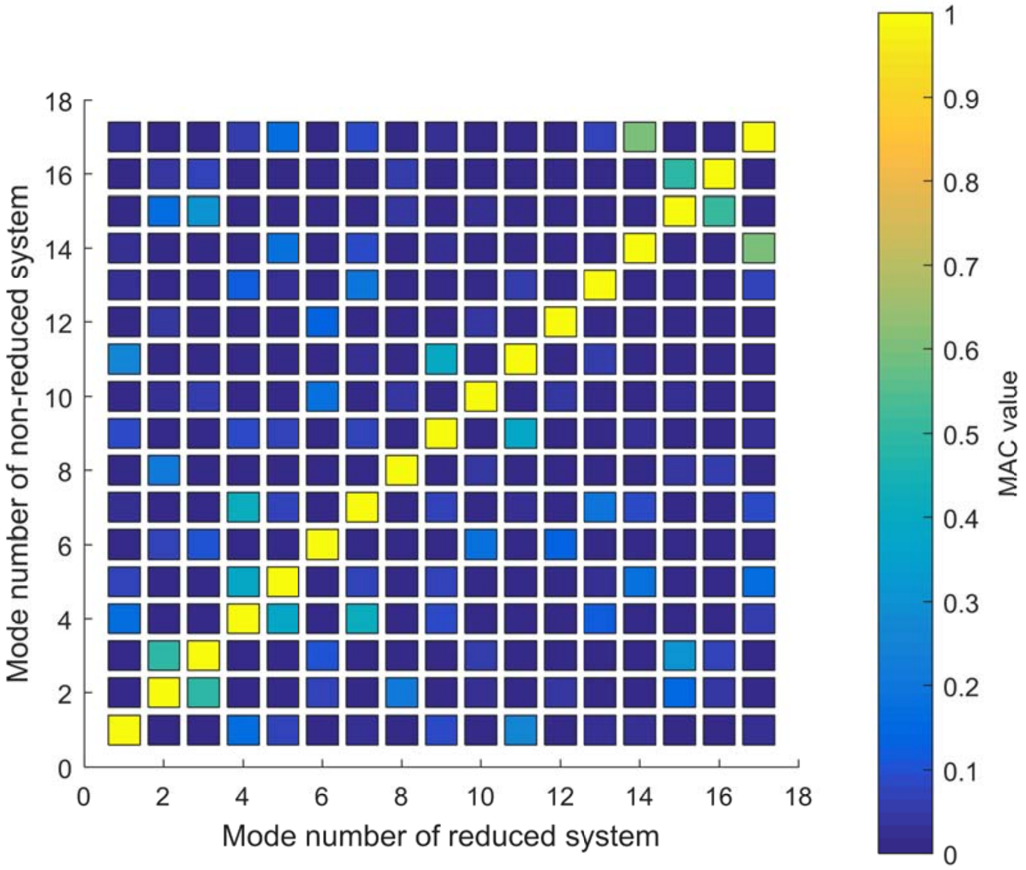

Figure 5.14. MAC for reduced system by the present method in the bended pipe problem with matching mesh.

Table 5.6. Computational costs for the bended pipe problem.

Methods	Items	Computation times [sec]	Ratio [%]
Original IRS ($N_1 = 2340$)	Load system matrices ($\mathbf{M}_g$, $\mathbf{K}_g$)	0.09	0.01
	Matrix permutation (master & slave DOFs)	0.12	0.02
	Guyan reduction ($\mathbf{T}_0$, $\overline{\mathbf{M}}_0$, $\overline{\mathbf{K}}_0$)	576.98	80.69
	IRS reduction ($\mathbf{H}_0$, $\mathbf{T}_1$, $\overline{\mathbf{M}}_1$, $\overline{\mathbf{K}}_1$)	137.90	19.28
	Total	715.09	100.00
Present ($N_1 = 2340$)	Load substructural system matrices ($\mathbf{M}^{(i)}$, $\mathbf{K}^{(i)}$, $\mathbf{B}^{(i)}$)	0.22	0.03
	Substructural Matrix permutation (master & slave DOFs)	0.07	0.01
	Substructural Guyan reduction ($\mathbf{T}_0^{(i)}$, $\overline{\mathbf{M}}_0^{(i)}$, $\overline{\mathbf{K}}_0^{(i)}$)	105.48	14.75
	Substructural IRS reduction ($\mathbf{H}_0^{(i)}$, $\mathbf{T}_1^{(i)}$, $\overline{\mathbf{M}}_1^{(i)}$, $\overline{\mathbf{K}}_1^{(i)}$)	159.76	22.34
	Assemble substructural IRS reduced matrices	0.12	0.02
	Total	265.65	37.15

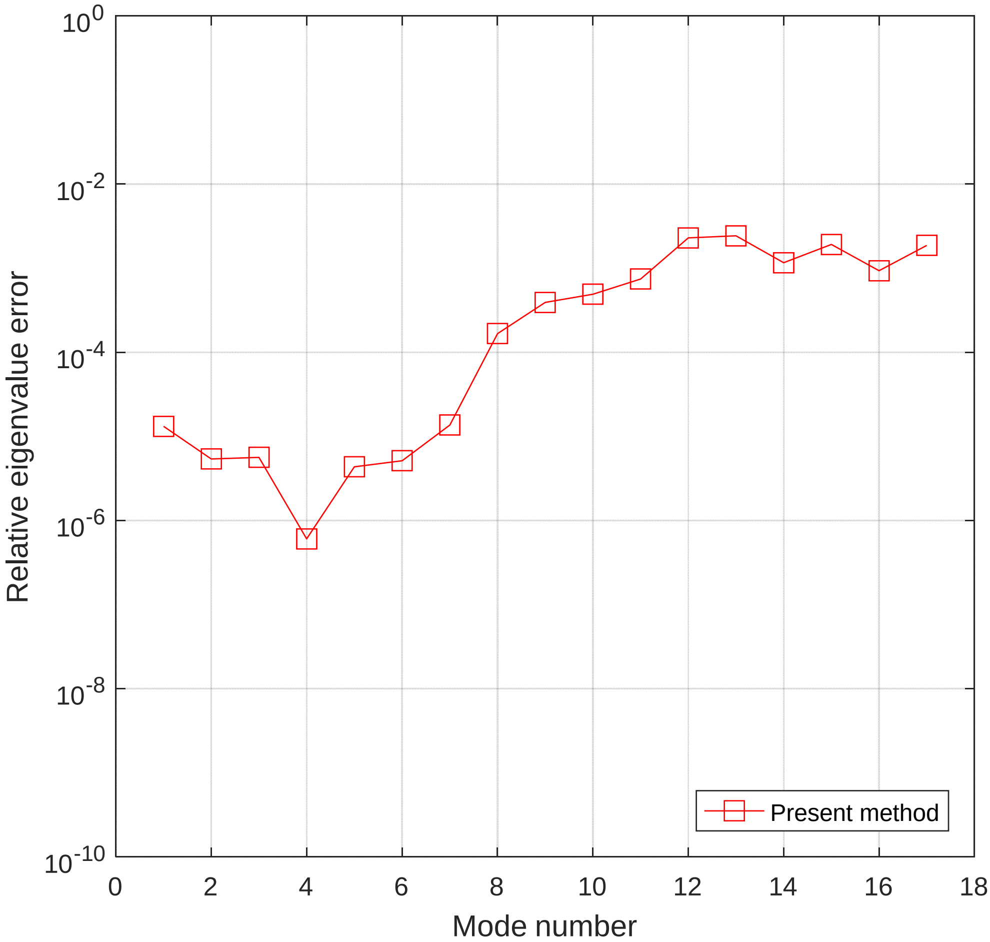

Figure 5.15. Relative eigenvalue errors in the bended pipe problem with non-matching mesh.

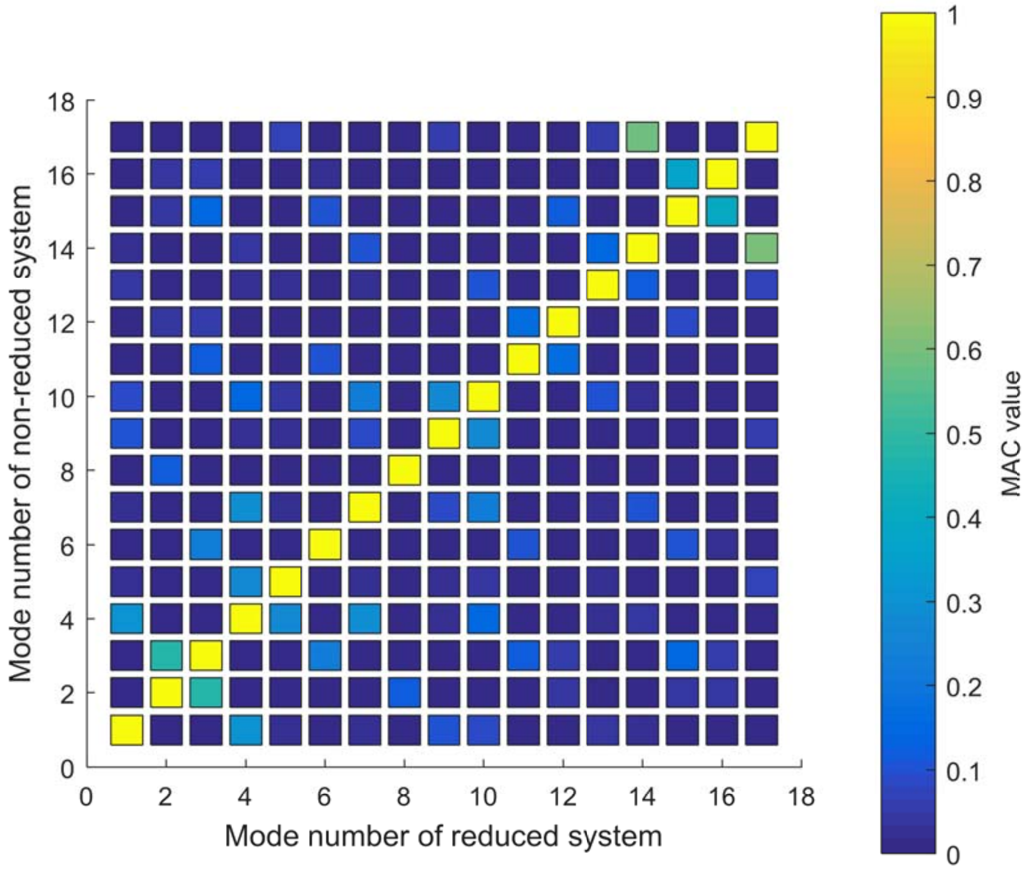

Figure 5.16. MAC for reduced system by the present method in the bended pipe problem with non-matching mesh.

5.2.5 Wind turbine rotor problem

We consider a 600 kW wind turbine rotor structure as shown in Fig. 5.17. The rotor diameter is 39.76m, Young's modulus E is 58 GPa, Poisson's ratio ν is 0.43, and density ρ is 1700 kg/m^3. The all substructures are modeled by the well-known commercial FE analysis software, ADINA [70].

The FE model of the structure is an assemblage of four substructural FE models ($N_s = 4$): three turbine blades and a rotor hub. The turbine blade FE model has 5082 shell elements and 5101 nodes. Due to its shell-shell intersection on the blade edge, all the nodes were modeled by 6 DOFs. The FE model of rotor hub has 508 shell elements and 560 nodes, all the nodes were modeled by 5 DOFs. The master DOFs are selected by using the ratio of the diagonal terms of mass and stiffness matrices [24-25]. Table 5.7 lists the numbers of master DOFs used and the numbers of DOFs in the original and reduced systems. In order to link the finite element model of the rotor hub and turbine blades, the Lagrange multiplier is considered for translational DOFs. For structures with repetitive patterns as in this numerical example, the present method is more efficient because it does not need to build a complete finite element model.

Fig. 5.18 presents the relative eigenvalue errors obtained by the present methods, and Table 5.8 shows the detailed computational costs. Fig. 5.19 presents the MAC for reduced system by the present method. The pairs of eigenvectors from the reduced model and non-reduced model in each mode are showed the acceptable consistency. Because the structure with repetitive patterns by the same turbine blade FE model, it has pair vibration modes with the similar eigenvalue. These results can be investigated by off-diagonal MAC values and the corresponding approximated eigenvalues.

Here, implementing a global FE model with many DOFs to perform the analysis requires immeasurable computational costs and time. The original IRS method is hardly acceptable to reduce this FE model because it needs to construct global transformation matrix and perform computation with fully-populated matrices. As mentioned previously, the present method can reduce the structure of each substructure independently and then obtain a reduced model by simply assembling the substructural matrices.

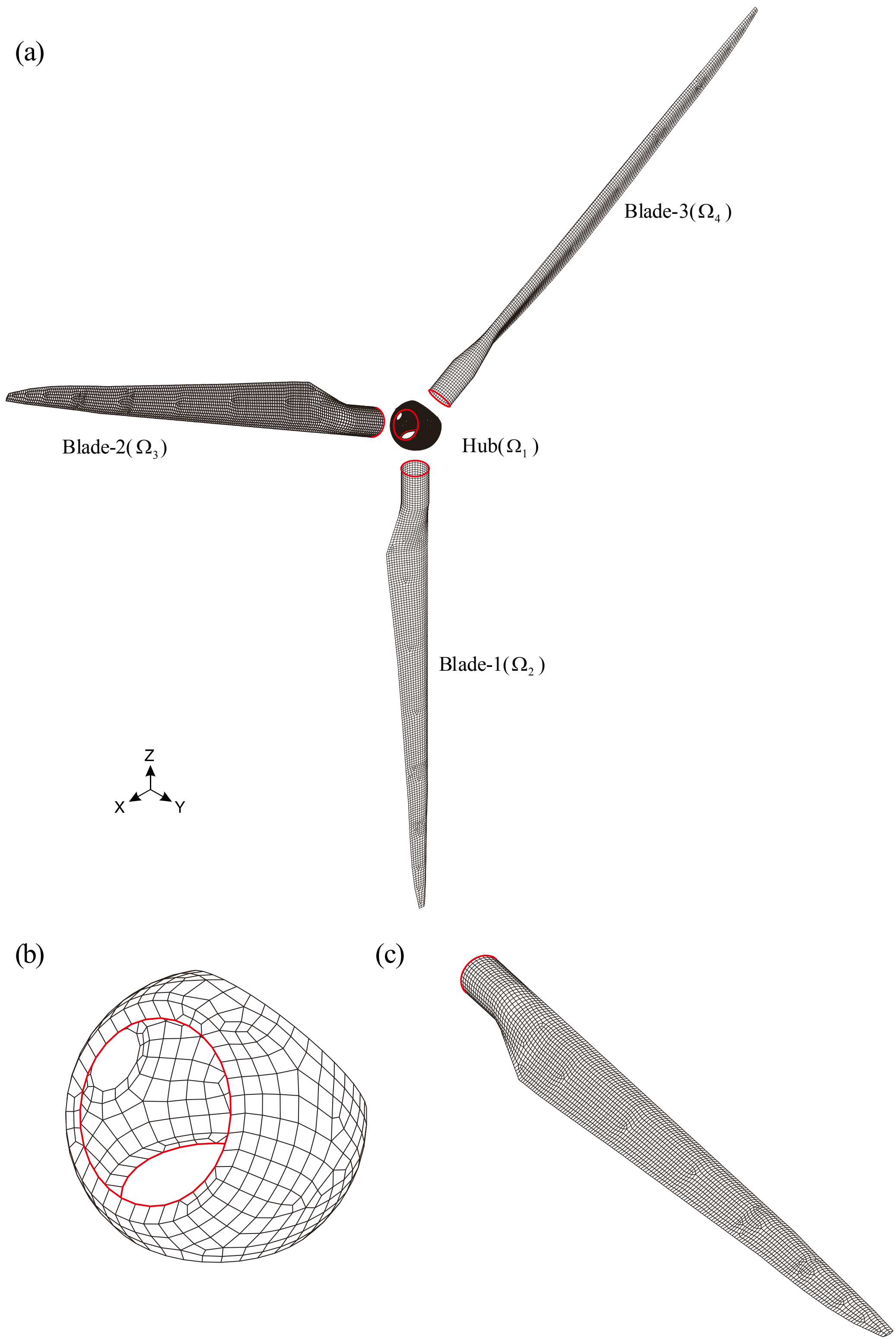

Figure 5.17. Wind turbine rotor problem.

Table 5.7. Number of master DOFs used and number of DOFs in original and reduced systems for the wind turbine rotor problem.

Method	$N_m^{(1)}$	$N_m^{(2)}$	$N_m^{(3)}$	$N_m^{(4)}$	N_m	N_b	N_g	N_1
Present	505	498	498	498	1999	288	94906	2287

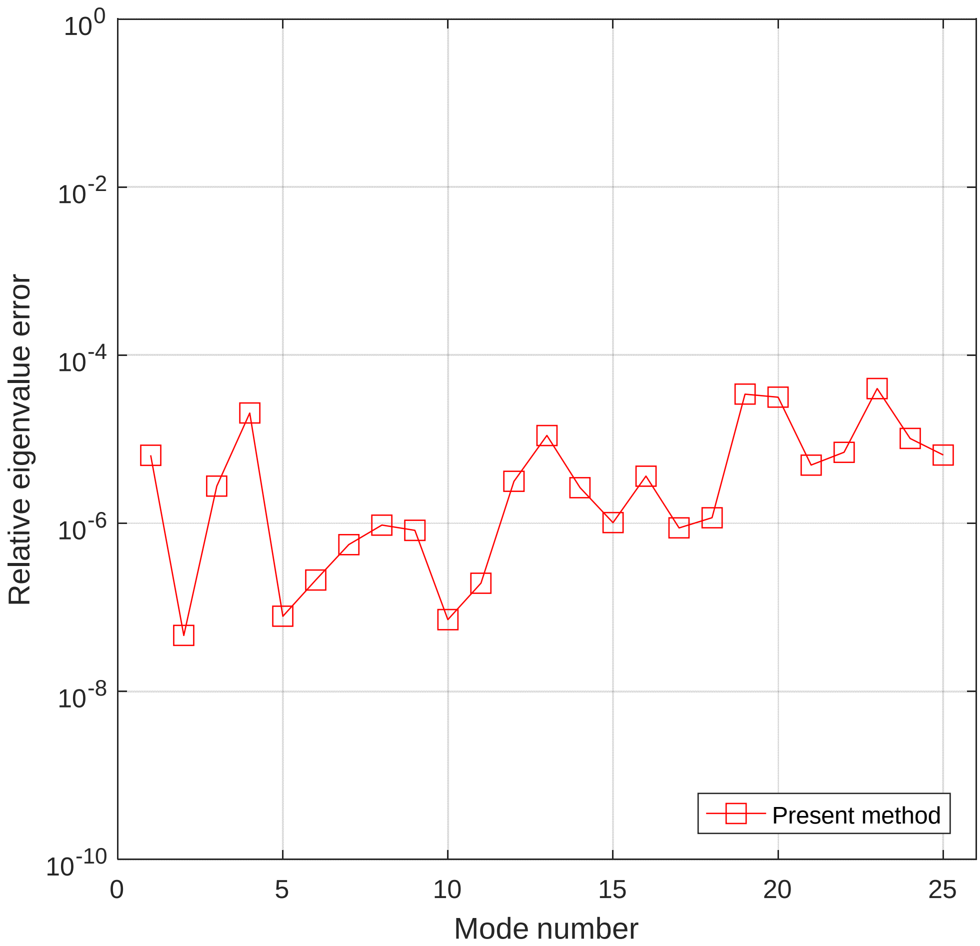

Figure 5.18. Relative eigenvalue errors in the wind turbine rotor problem.

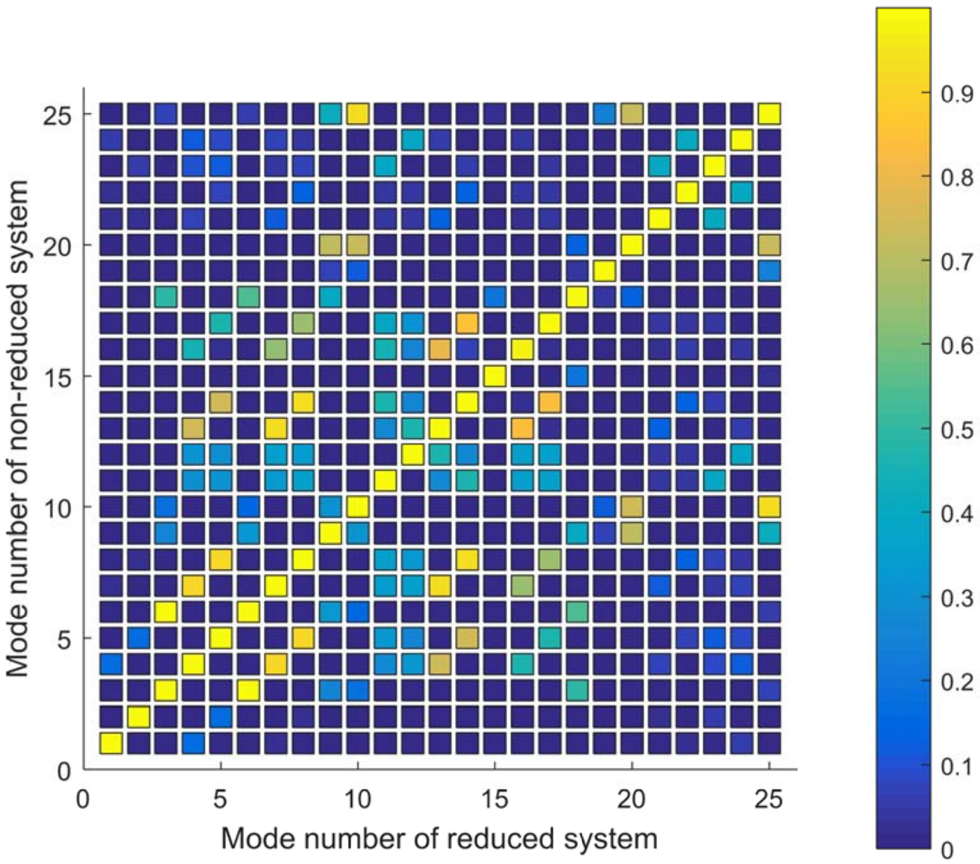

Figure 5.19. MAC for reduced system by the present method in the wind turbine rotor problem.

Table 5.8. Computational costs for the wind turbine rotor problem.

Method	Items	Computation times [sec]	Ratio [%]
Present	Load system matrices ($\mathbf{M}^{(i)}$, $\mathbf{K}^{(i)}$, $\mathbf{B}^{(i)}$)	0.55	0.06
	Matrix permutation (master & slave DOFs)	0.13	0.02
	Substructural Guyan reduction	282.94	33.58
	Substructural IRS reduction	558.85	66.33
	Assemble substructural IRS reduced matrices	0.10	0.01
	Total	842.57	100.00

5.2.6 NACA 2415 wing with ailerons problem

A NACA 2415 wing structure with clamped boundary at one end is considered again for the present method. The structural configuration and specification are illustrated in Fig. 5.20. The two ailerons are connected by a frictionless hinge to the first substructure. Due to the ailerons, the two rigid body modes are calculated in the eigenvalue analysis of both global and reduced eigenvalue problems. The modeling of hinge is simply implemented by the Lagrange multipliers.

The length L is 0.9144 m, width W is 0.2286 m, and thickness H is 0.0345 m. Young's modulus E is 71 GPa, Poisson's ratio ν is 0.33, and density ρ is 3000 $\mathrm{kg/m^3}$. The whole model is an assemblage of four substructural FE models ($N_s = 3$). The each substructure is discretized by 3873, 112 and 144 shell elements, respectively (19250, 725 and 925 DOFs).

Table 5.9 lists the numbers of dominant modes used and the numbers of DOFs in the original and reduced systems. Fig. 5.21 presents the relative eigenvalue errors obtained using the present method. Fig. 5.22 presents the MAC for reduced system by the present method. The results show that the robustness of eigenpairs approximated by the present method.

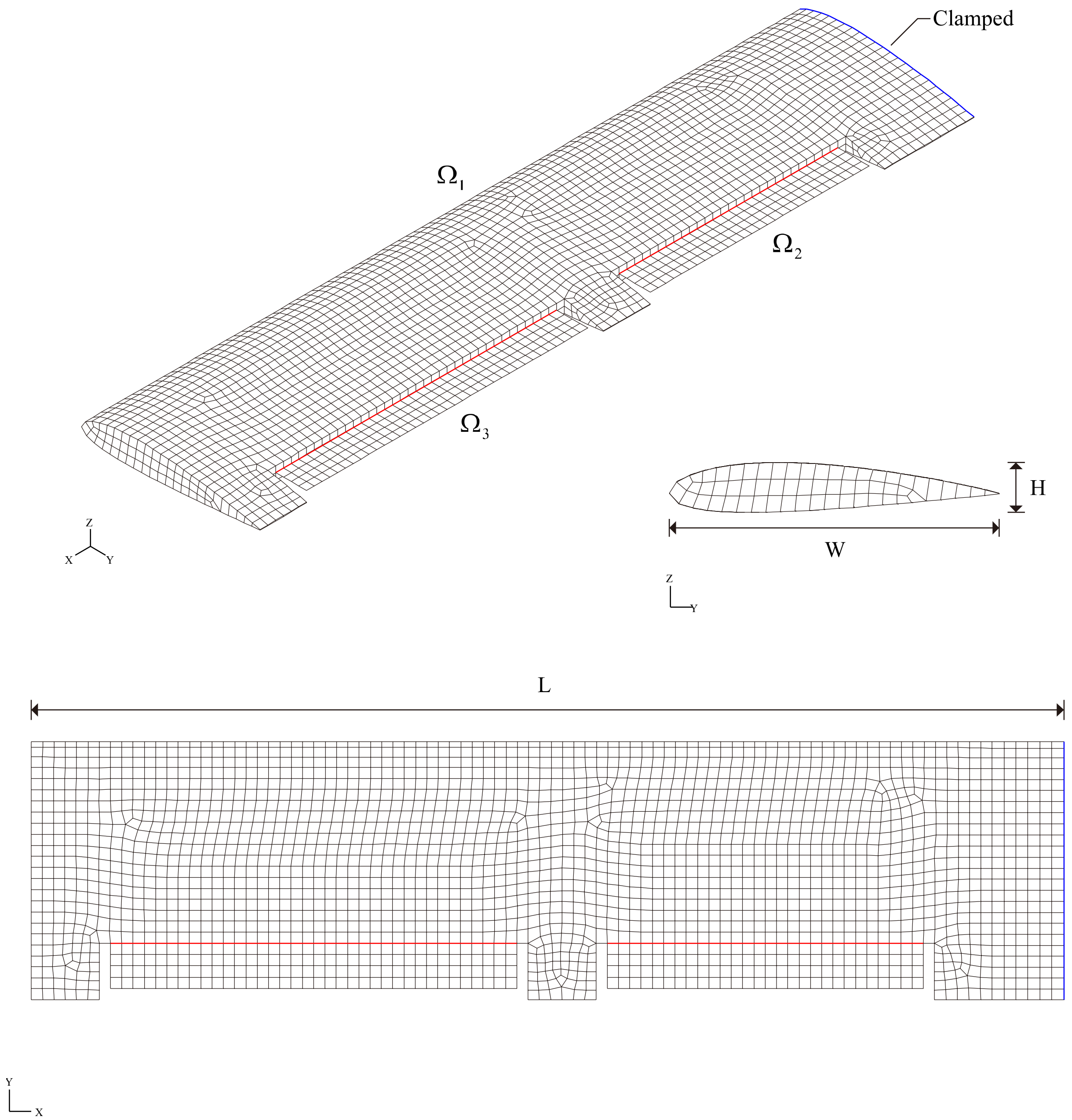

Figure 5.20. NACA 2415 wing with ailerons problem.

Table 5.9. Number of master DOFs used and number of DOFs in original and reduced systems for the NACA 2415 wing with ailerons problem.

Method	$N_m^{(1)}$	$N_m^{(2)}$	$N_m^{(3)}$	N_m	N_b	N_g	N_1
Present	1675	195	245	2115	198	21098	2313

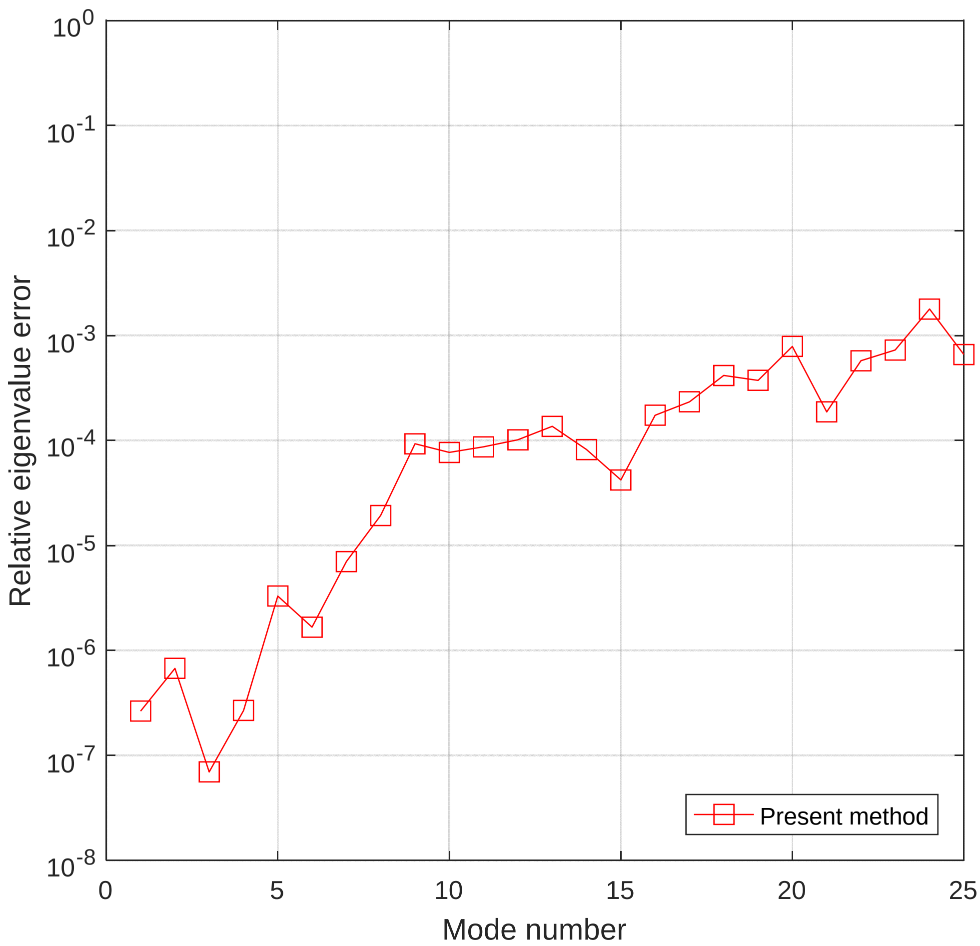

Figure 5.21. Relative eigenvalue errors in the NACA 2415 wing with ailerons problem.

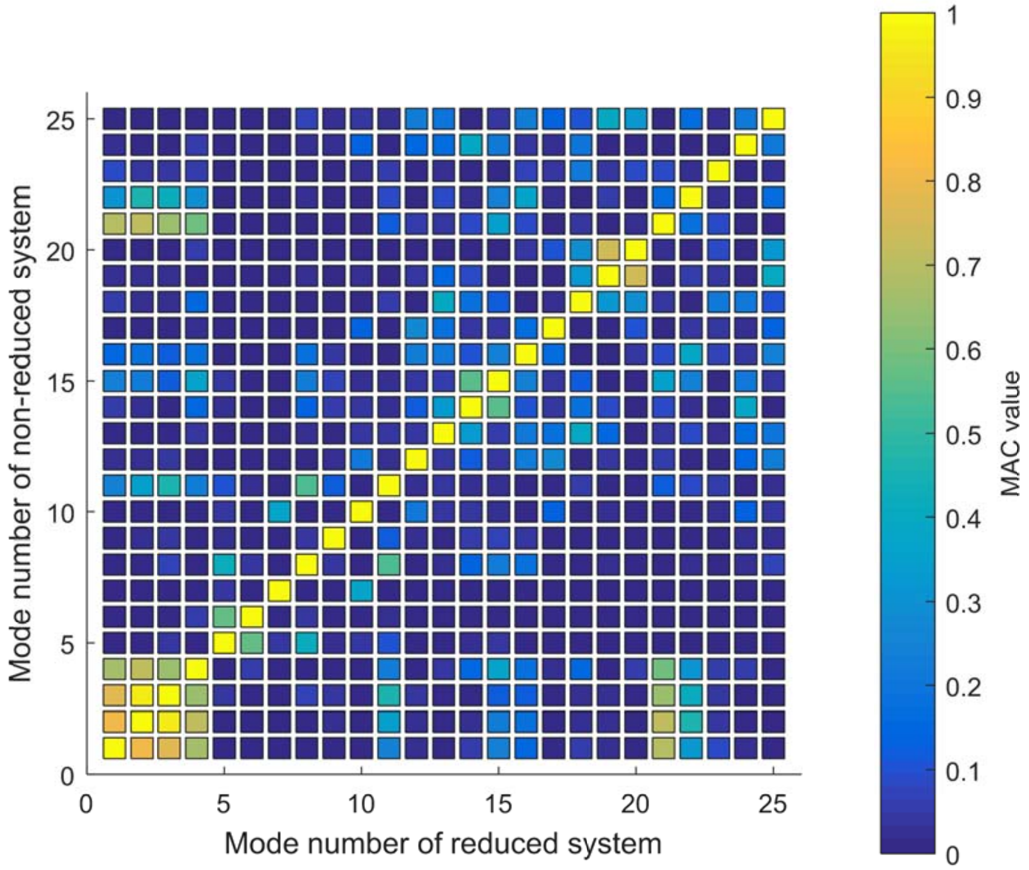

Figure 5.22. MAC for reduced system by the present method in the NACA 2415 wing with ailerons problem.

5.2.7 Cable-stayed bridge problem

We finally consider a cable-stayed bridge problem as shown in Fig. 5.23 and 5.24. The unit of length in this figure is feet (ft). The FE model and its mass and stiffness matrices are obtained by the well-known commercial FE analysis software, ADINA [70]. The structure is modeled using 504 shell elements for the girder, 50 3D solid elements for the tower, and 4 3D truss elements for the cable, respectively. The number of nodes is 1666, and total DOFs is 6878.

Here, we considered the bridge structure in Fig. 5.23 as one sub-structure and connected multiple substructures to make the long-span bridge structure as in Fig. 5.24. In this problem, we assemble the six substructures ($N_s = 6$), and the number of DOFs in the original assembled FE model (N_g) is 42293.

In this problem, we consider the two numerical cases of master DOFs selection:

- The only interface DOFs are selected as the master DOFs ($N_1 = 3075$).
- The selected master DOFs contain all interface DOFs and 1% of interior DOFs for each sub-structure ($N_1 = 3555$). The interior DOFs are selected by using the ratio of the diagonal terms of substructural mass and stiffness matrices [24-25].

Table 5.10 lists the numbers of dominant modes used and the numbers of DOFs in the original and reduced systems. Fig. 5.25 presents the relative eigenvalue errors obtained using the present method. Fig. 5.26 presents the MAC for reduced system compared to the non-reduced global FE model. Through the numerical results, both the eigenvalues and the corresponding eigenvectors are shown to be precisely approximated using the present method.

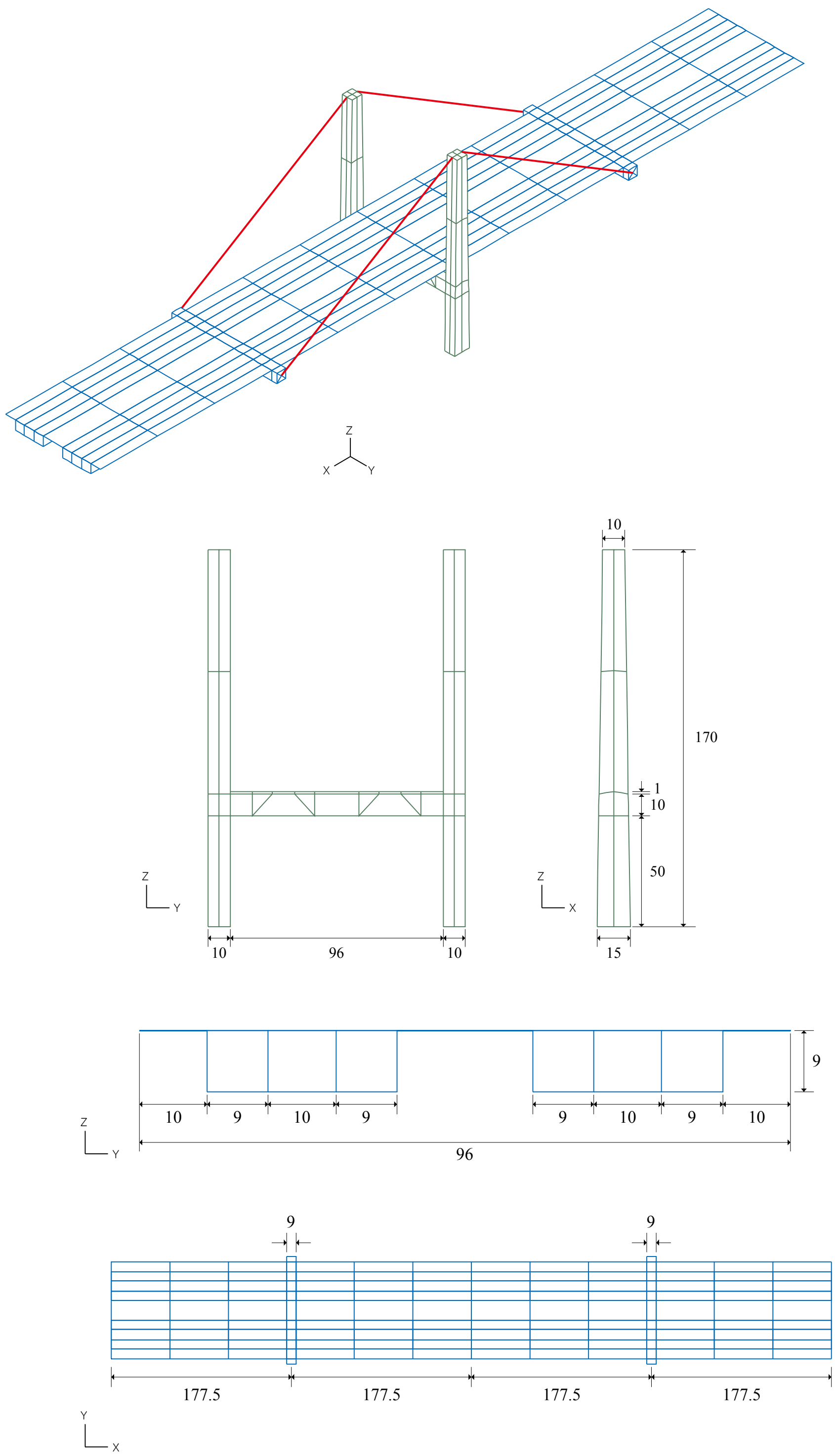

Figure 5.23. Cable-stayed bridge problem (1 substructure).

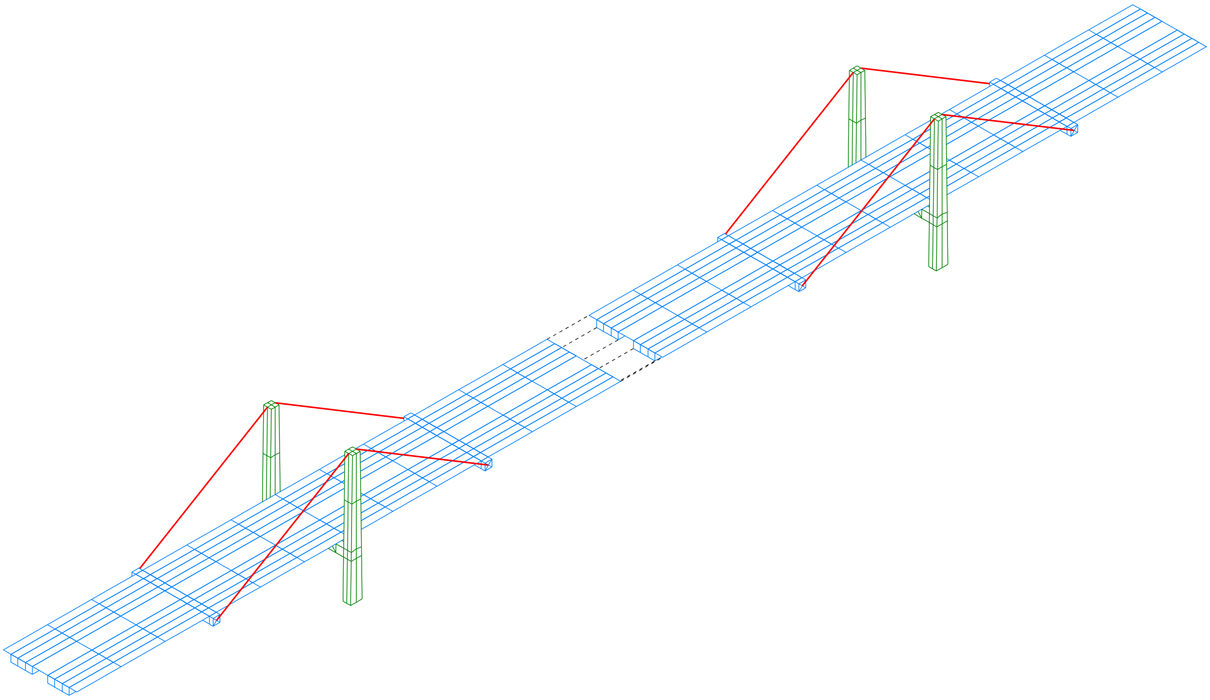

Figure 5.24. Connection of cable-stayed bridge substructures ($N_s = 2$).

Table 5.10. Number of master DOFs used and number of DOFs in original and reduced systems for the cable-stayed bridge problem ($N_s = 6$).

Method	$N_m^{(1)}$	$N_m^{(2)}$	$N_m^{(3)}$	$N_m^{(4)}$	$N_m^{(5)}$	$N_m^{(6)}$	N_m	N_b	N_g	N_1
Present (case 1)	205	410	410	410	410	205	2050	1025	42293	3075
Present (case 2)	285	490	490	490	490	285	2530	1025	42293	3555

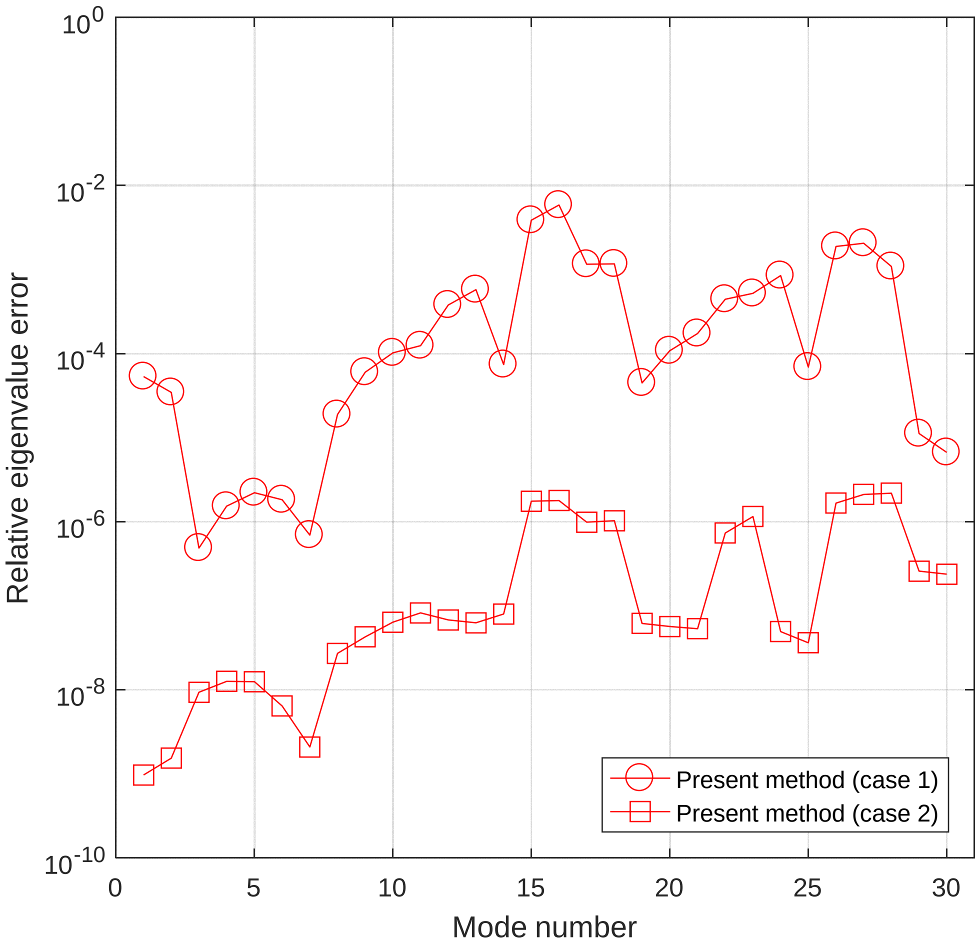

Figure 5.25. Relative eigenvalue errors in the cable-stayed bridge problem ($N_s = 6$).

(a)

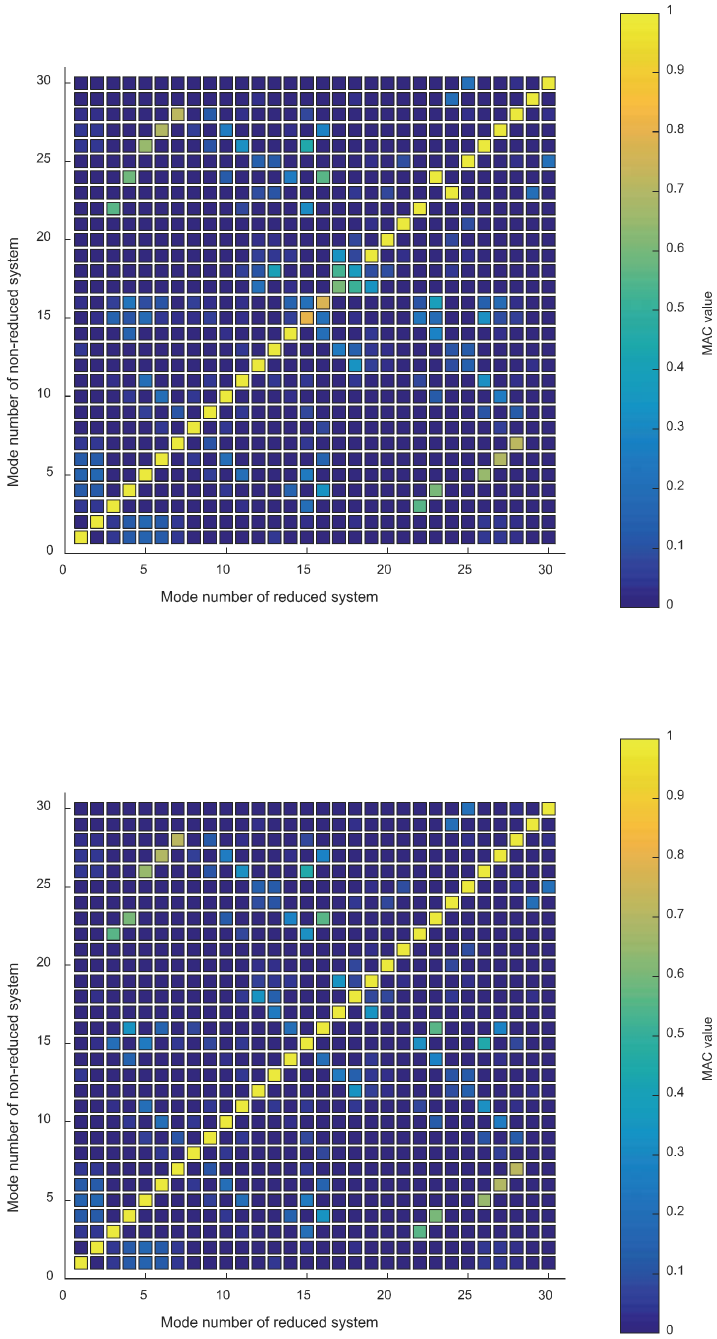

(b)

Figure 5.26. MAC for reduced system by the present method in the cable-stayed bridge problem ($N_s = 6$): (a) case 1, (b) case 2.

Chapter 6. Conclusions

This dissertation focused on developing the new model reduction methods with free-interface substructuring. The developed model reduction methods have the following advantages: (1) Ensure the substructural independence. (2) We do not need to repeat the reduction procedure for each assembly stage. (4) The free-interface condition can easily consider the experimentally measured dynamic behavior of the substructure. (5) It can be easily applied to the non-matching mesh condition or various interface boundary conditions. In this dissertation, the new CMS method by improving the accuracy of dual Craig-Bampton (DCB) method, the error estimation method for the DCB method, and the dynamic condensation method with fully decoupled substructuring were proposed.

First, we proposed a new CMS method by improving the DCB method. The formulation was derived by considering the second order effect of residual substructural modes. The transformation matrix of the original DCB method was enhanced by using the additional dynamic terms, and the resulting additional interface coordinates in the reduced system was eliminated by applying the concept of SEREP. An important feature of the improved DCB method lies in the fact that the accuracy of reduced models is remarkably improved and negative eigenvalues are avoided in lower modes. Through various numerical examples, we demonstrated accuracy and computational efficiency of the improved DCB method compared to the original DCB method.

Second, we proposed an error estimation method to accurately estimate the relative eigenvalue errors of reduced model by the DCB method. To develop the accurate error estimator for the DCB method, the second order effect of residual substructural modes was considered as the second order term of residual flexibility matrix for each substructure. Through various numerical examples, we demonstrated the performance of the proposed error estimation method. By using accurately estimated error, we showed that the approximated eigenvalues by the DCB method could be corrected with lower bound of errors.

Finally, we proposed a dynamic condensation method by using the free-interface substructuring algorithm. We implement the formulation of the IRS method to the FE model of substructure. In the present method, it is possible to independently perform the procedure from construction to reduction of each substructure. Since we considered the substructuring, we could efficiently reduce the large structural FE model that cannot be handled by the original IRS method. An important feature of the present method is that it can construct a reduced model with considerable efficiency with maintaining the similar accuracy of original IRS method, and can be applied to non-matching mesh conditions and complex substructure boundary conditions. Through various numerical examples, we demonstrated accuracy and computational efficiency of the present method compared to the original IRS method.

In future work, for the proposed model reduction methods in Chapter 3 and 5, it would be valuable to develop an optimized parallel computation algorithm using multi-processes for the present method to deal with FE models with a large number of substructures and DOFs. Using the substructural independence, a hybrid model reduction method can be developed that uses both proposed methods (CMS and DOF based reduction) selectively for each substructure, and it is expected that the drawbacks of the two methods can be complemented. We expect that the new method is an attractive solution for constructing accurate reduced models for experimental-FE model correlation, FE model updating, and optimizations. Especially, the Lagrange multiplier based finite element modeling is applied for the analyses of multi-physics and multi-material structures. Therefore, the developed method is expected to be a breakthrough not only for conventional model reduction but also for the efficient analysis of complex physical phenomena.

For the error estimation method in Chapter 4, accurate error estimation is expected to be able to satisfy the solution accuracy effectively in application studies using the reduced model with the DCB method. In future work, it would be also valuable to develop an error estimator for the eigenvectors. If eigenvalues and eigenvectors can be estimated and further corrected, it is expected to be applied to the development of novel mode selection method for various CMS methods.

Bibliography

[1] Hurty WC. Dynamic analysis of structural systems using component modes. AIAA J 1965;3(4):678-685.

[2] Hurty WC. A criterion for selecting realistic natural modes of a structure. Technical Memorandum, Jet Propulsion Laboratory, Pasadena, CA, 1967;33-364

[3] Craig RR, Bampton MCC. Coupling of substructures for dynamic analysis. AIAA J 1968;6(7):1313-1319.

[4] Benfield WA, Hruda RF. Vibration analysis of structures by component mode substitution. AIAA J 1971;9:1255-1261.

[5] MacNeal RH, Hybrid method of component mode synthesis. Comput Struct 1971;1(4):581-601.

[6] Rubin S. Improved component-mode representation for structural dynamic analysis. AIAA J 1975;13(8):995-1006.

[7] Craig RR, Chang CJ. On the use of attachment modes in substructure coupling for dynamic analysis. 18st Structures, Structural Dynamics and Material Conference 1977;89-99.

[8] Qiu JB, Ying ZG, Williams FW. Exact modal synthesis techniques using residual constraint modes. Intl J Numer Methods Eng 1997;40(13):2475-2492.

[9] Rixen DJ. A dual Craig-Bampton method for dynamic substructuring. J Comput Appl Math 2004;168(1-2):383-391.

[10] Park KC, Park YH. Partitioned component mode synthesis via a flexibility approach. AIAA J 2004;42(6):1236-1245.

[11] Bennighof JK, Lehoucq RB. An automated multi-level substructuring method for eigenspace computation in linear elastodynamics, SIAM J Sci Comput 2004;25(6):2084–2106.

[12] Bourquin, F. Analysis and comparison of several component mode synthesis methods on one-dimensional domains. Numerische Mathematik 1990;58(1):11-33.

[13] Yang C, Gao W, Bai Z, Li XS, Lee LQ, Husbands P, Ng E. An algebraic substructuring method for large-scale eigenvalue calculation. SIAM Journal on Scientific Computing 2015;27(3):873-892.

[14] Elssel K, Voss H. An a priori bound for automated multilevel substructuring. SIAM Journal on Matrix Analysis and Applications 2006;28(2):386-397.

[15] Jakobsson H, Larson MG. A posteriori error analysis of component mode synthesis for the elliptic eigenvalue problem. Comput Methods Appl Mech Eng 2011;200(41):2840-2847.

[16] Guyan RJ. Reduction of stiffness and mass matrices. AIAA J 1965;3(2):380.

[17] O'Callahan J. A procedure for an improved reduced system (IRS) model. Proceedings of the 7th International Modal Analysis Conference, Las Vegas, 1989:17-21.

[18] O'Callahan J, Avitabile P, Riemer R. System equivalent reduction expansion process (SEREP). Proceedings of the 7th International Modal Analysis Conference, Las Vegas, 1989:29-37.

[19] Blair MA, Camino TS, Dickens JM. An iterative approach to a reduced mass matrix. In 9th Conference International Modal Analysis Conference (IMAC), 1991;1:621-626.

[20] Friswell MI, Garvey SD, Penny JET. Model reduction using dynamic and iterated IRS techniques. J Sound Vib 1995;186(2):311-323.

[21] Kammer DC, Triller MJ. Selection of Component Modes for Craig–Bampton Substructure Representations. AIAA J 1996;118(2):264-270.

[22] Givoli D, Barbone PE, Patlashenko I. Which Are the Important Modes of a Subsystem? Intl J Numer Methods Eng 2004;59(2):1657-1678.

[23] Liao BS, Bai Z, Gao W. The Important Modes of Subsystems: A Moment-Matching Approach. Intl J Numer Methods Eng 2007;70(13):1581-1597.

[24] Henshell RD, Ong JH. Automatic masters for eigenvalue economization. Earthq Eng Struct D 1974;3(4):375-383.

[25] Ong JH. Improved automatic masters for eigenvalue economization. Finite Elem Anal Des 1987;3(2):149-160.

[26] Rixen DJ. Dual Craig-Bampton with enrichment to avoid spurious modes. Proceedings of the IMAC-XXVII Conference & Exposition on Structural Dynamics, Orlando, USA. 2009.

[27] Markovic D, Ibrahimbegovic A, Park KC. Partitioning based reduced order modelling approach for transient analyses of large structures. Engineering Computations 2009;26(1/2):46-68.

[28] Bathe KJ, Jian Dong. Component mode synthesis with subspace iterations for controlled accuracy of frequency and mode shape solutions. Compt Struct 2014;139:28-32

[29] Perdahcıoğlu, Akçay D, et al. An optimization method for dynamics of structures with repetitive component patterns. Struct Multidisc Optim 2009;39(6):557-567.

[30] Hinke L, Dohnal F, Mace BR, Waters TP, Ferguson NS. Component mode synthesis as a framework for uncertainty analysis. J SOUND VIB 2009;324(1):161-178.

[31] Voormeeren SN, De Klerk D, and Rixen DJ. Uncertainty quantification in experimental frequency based substructuring. Mech Syst Signal PR 2010;24(1):106-118.

[32] Voormeeren SN, C. Van Der Valk PL, Rixen DJ. Generalized methodology for assembly and reduction of component models for dynamic substructuring. AIAA J 2011;49(5):1010-1020.

[33] Kadawathagedara SW, Rixen DJ. Model reduction in co-rotated multi-body dynamics based on the dual Craig-Bampton method. 52nd AIAA/ASME/ASCE/AHS/ASC Structures, Structural Dynamics and Materials Conference, Denver, USA, 4-7 April 2011;2011-2029.

[34] Papadimitriou C, Papadioti DC. Component mode synthesis techniques for finite element model updating. Comput Struct 2013;126:15-28.

[35] Qu, Z. Q. Model order reduction techniques with applications in finite element analysis. Springer Science & Business Media, 2013.

[36] Rixen DJ, Boogaard A, van der Seijs MV, van Schothorst G, van der Poel T. Vibration source description in substructuring: A theoretical depiction. Mech Syst Signal PR 2015;60:498-511.

[37] Géradin M, Rixen DJ. A ‘nodeless’ dual superelement formulation for structural and multibody dynamics application to reduction of contact problems. Intl J Numer Methods Eng 2016;106:773-798.

[38] Brecher C, Fey M, Tenbrock C, Daniels M. Multipoint constraints for modeling of machine tool dynamics. J Manuf Sci E-T ASME 2016;138(5):051006.

[39] Blachowski B, Gutkowski W. Effect of damaged circular flange-bolted connections on behaviour of tall towers, modelled by multilevel substructuring. Eng Struct 2016;111:93-103.

[40] Kim JG, Lee PS. An enhanced Craig-Bampton method. Intl J Numer Methods Eng 2015; 103:79-93.

[41] Kim JG, Boo SH, Lee PS. An enhanced AMLS method and its performance. Comput Methods Appl Mech Eng 2015;287:90-111.

[42] Boo SH, Lee PS. A dynamic condensation method using algebraic substructuring, Intl J Numer Methods Eng 2016;DOI: 10.1002/nme.5349.

[43] Kim JM. Development of a Component Mode Synthesis Method with Higher-order Residual Flexibility [M.S. thesis]. Department of Mechanical Engineering, KAIST, 2016.

[44] Kim JH, Kim J, Lee PS. Improving the accuracy of the dual Craig-Bampton method. Compt Struct 2017;191:22-32.

[45]Kim JG, Lee KH, Lee PS. Estimating relative eigenvalue errors in the Craig-Bampton method, Compt Struct 2014; 139:54-64.

[46] Boo SH, Kim JG, Lee PS. A simplified error estimator for the CB method and its application to error control. Compt Struct 2016;164:53-62.

[47] Boo SH, Kim JG, Lee PS. Error estimation method for automated multi-level substructuring method, Intl J Numer Methods Eng 2015;DOI:10.1002/nme.5161.

[48] Kim JG, Lee PS. A posteriori error estimation method for the flexibility-based component mode synthesis, AIAA J 2015;53:2828-2837.

[49] Bouhaddi N, Fillod R. Substructuring using a linearized dynamic condensation method. Compt Struct 1992;45(4):679-683.

[50] Bouhaddi N, Fillod R. A method for selecting master DOF in dynamic substructuring using the Guyan condensation method. Compt Struct 1992;45(5-6):941-946.

[51] Kim H, Cho MH. Improvement of reduction method combined with sub□domain scheme in large□scale problem. Intl J Numer Methods Eng 2007;70(2):206-251.

[52] Cho M, Baek S, Kim H, Kim KO. Identification of Structural Systems Using an Iterative, Improved Method for System Reduction (TN). AIAA J 2009;47(9):2255.

[53] Kim H, Cho MH. Sub-domain reduction method in non-matched interface problems. J Mech Sci Technol 2008;22(2):203.

[54] Kim H, Cho MH, Kim H, Choi HG. Efficient construction of a reduced system in multi-domain system with free subdomains. Finite Elem Anal Des 2011;47(9):1025-1035.

[55] Park KH, Jun SO, Baek SM, Cho MH, Yee KJ, Lee DH. Reduced-order model with an artificial neural network for aerostructural design optimization. J Aircraft 2013.

[56] Chang S, Baek SM, Kim KO, Cho MH. Structural system identification using degree of freedom-based reduction and hierarchical clustering algorithm. J Sound Vib 2015;346:139-152.

[57] Yin T, Lam HF, Chow HM, Zhu HP. Dynamic reduction-based structural damage detection of transmission tower utilizing ambient vibration data. Eng Struct 2009;31(9).

[58] Kim CW, Kawatani M. Pseudo-static approach for damage identification of bridges based on coupling vibration with a moving vehicle. Struct Infrastruct E 2008;4(5):371-379.

[59] Pastor M, Binda M, Harčarik T. Modal assurance criterion. Procedia Engineer 2012;48:543-548.

[60] Allemang RJ. The modal assurance criterion–twenty years of use and abuse. Sound Vib 2003;37(8):14-23.

[61] Craig RR, Kurdila AJ. Fundamentals of structural dynamics. John Wiley & Sons, 2006.

[62] Géradin M, Rixen DJ. Mechanical vibrations: theory and application to structural dynamics. John Wiley & Sons, 2014.

[63] Golub GH, Van Loan CF. Matrix computations. 4thed. JHU Press; 2012, 304-307

[64] Van der Sluis A. Stability of the solutions of linear least squares problems. Numerische Mathematik J 1974;23(3);241-254.

[65] Bathe KJ, Dvorkin EN. A formulation of general shell elements - the use of mixed interpolation of tensorial components. Intl J Numer Methods Eng 1986;22(3):697-722.

[66] Bathe KJ. Finite element procedure, 2006.

[67] Lee PS, Bathe KJ. The quadratic MITC plate and MITC shell elements in plate bending, ADV ENG SOFTW 2010;41(5):712-728.

[68] Lee YG, Yoon KH, Lee PS. Improving the MITC3 shell finite element by using the Hellinger-Reissner principle, Compt Struct 2012;110-111:93-106.

[69] Jeon HM, Lee PS, Bathe KJ. The MITC3 shell finite element enriched by interpolation covers, Compt Struct 2014;134:128-142.

[70] ADINA system 9.3, ADINA R & D Inc., Watertown, MA; January 2017.